Macromodelling Of Microsystems

Eskild R. Westby

i

Abstract

The aim of this work has been to develop new knowledge about macro-modelling of microsystems. Doing that, we have followed two different approaches for generating macromodels, namely model order reduction and lumped modelling. The latter is a rather mature method which has been widely recognized and used for a relatively long period of time. Model order reduction, on the other hand, is a relatively new area still in rapid development. Due to this, the focus is therefore different for the two approaches. The parts considering reduced order modelling is strongly biased towards methodology and concepts, whereas parts on lumped modelling is biased towards systems and devices.

In the first part of this thesis, we focus on model order reduction. We introduce some approaches for reducing model order for linear systems, and demonstrate how a model of a (linear) squeeze-film damping system can be simplified. The example clearly demonstrates capabilities of model order reduction. It is also shown how the squeeze-film damping can be expressed in terms of an electrical equivalent circuit. We then move on to investigate model order reduction of nonlinear systems, where we present and use the concept of invariant manifolds. The concept can be explained in a simple manner by the following: for a linear system being excited in a single eigenmode, the motion will always stay on the phase-plane of that eigenmode. The surface described by the phase plane is an invariant manifold, since the state of the system never leaves the surface (without external excitation). Parallel to this, nonlinear systems may also contain such surfaces, or invariant manifolds, that the motion always will stay on. For nonlinear systems, however, these surfaces are generally no longer planar, but curved. While the concept of invariant manifolds is general, we utilize it for reducing models. An obvious advantage of using invariant manifold theory is that it offers a conceptually clear understanding of effects and behaviour of nonlinear system.

A major difficulty in using the invariant manifold method is to identify the shape of the manifold. We utilize an asymptotic approach presented by others [1]. We investigate the accuracy of the asymptotic approach. For our examples, we find that the nonlinear behaviour of the slave modes are stronger than the retained mode(s). This implies that the polynomial approximations of the slave modes will diverge earlier from the exact solution, than will the approximation of the retained mode. Thus the reduced model is approximating the retained mode better than the slave modes.

The treatment of external forcing for reduced models created via the invariant manifold approach is discussed. We present a new geometrical interpretation, and show how this leads to a procedure where external forcing can be dealt with in a manner consistent with the invariance property of the man-

ifold. The interpretation also indicates how this can be utilized to minimize errors by creating a manifold of larger dimension.

We have also extended the asymptotic approach in a manner that makes it possible to create design-parameter sensitive models. The asymptotic approach, both with regards to modal amplitude and to design-parameters, limits the range of validity of the design-parameter sensitive model. Nevertheless, it gives the designer the possibility to reason about changes in linear and nonlinear behaviour of the system, and is therefore a valuable tool. We investigate an industrialized dual-axis accelerometer by means of the method and demonstrate some of the capabilities of the method.

In the last chapter dealing with reduced order modelling, we discuss how manifolds for nonlinear dissipative systems can be found. We present a method, which we apply to the industrialized dual-axis accelerometer, now with squeeze-film damping included.

After having focused on model order reduction in the first chapters, we focus on lumped modelling of a microresonator in chapter 6. We also discuss other topics, like electrical equivalents of mechanical systems. Particularly we demonstrate the two analogies between the mechanical and the electrical domain. It is shown how the $f \rightarrow V$ analogy, linking velocity to voltage, is the natural choice. This does, however, have the implication that the electrostatic transducer element, expressed as an electrical equivalent, involves a gyrator. The microresonator is modelled using a lumped modelling technique, disregarding all nonlinear effects except in the electrostatic transducer. We create electrical equivalent circuits of the system by employing the $f \rightarrow V$ analogy. We create 3 lumped models with different number of degrees of freedom.

In chapter 7, we analyse an electromagnetic system, intended for levitating objects. The analysis is done by using a lumped model, where the elements are created on the basis of analytical solutions. By using the compact model, we demonstrate the scaling effects of the system, clearly showing that this system takes advantage of the miniaturization. Furthermore, the analysis shows that the system is intrinsically stable. However, an effect which will cause the stable state of the floating disc to be slightly tilted is also unveiled. This is the first analysis done assessing the stability criterions of such a systems. The knowledge arising from the analysis gives strong indications on how such a system can be utilized and how it can be improved.

Acknowledgements

First, I would like to thank Professer Tor A. Fjeldly for giving me the opportunity to perform research in this new and interesting research field. He has been an excellent supervisor, always available and open for discussions. I would also like to express my gratitude to Professor Alan Sangster and Dr. Marc Desmulliez for allowing me to do parts of the work at the Heriot-Watt University. Professor Alan Sangster also introduced me to the field of electromagnetics.

I am very much indepted to SensoNor (now a subsidiary of Infinion Technologies) for granting me leave of absence to pursue a PhD and for economical support at various stages. I would also like to thank the people at SensoNor.

This thesis has been fulfilled under the *Asic for MEMS* project financed by The Norwegian Research Council.

v

Table of content

Chapter 1
Introduction

1.1   Background and motivation

Microsystems, and more specifically MEMS (MicroElectroMechanical System), is a relatively new area. Many consider an article published in 1982 ("Silicon as a mechanical material", [2]) as the starting point, although MEMS-devices had been around for nearly a decade at the time. A myriad of fabrication techniques enabling microsystems to be realized has been developed and improved considerably in the past two decades or so. Examples are wet and dry anisotropic etching for both bulk and surface micromachining, and double-sided lithography. This has allowed new concepts and devices to be brought forward, motivated by the market forces and the scientists' ingenuity. Examples are ink-jet heads for printers, accelerometers for airbag systems, and micromirror arrays used in projectors.

One of the fundamental characteristics of microsystems is their small size. Although the macroscopic and the microscopic world is governed by the same physical laws, the relative importance of the individual effects changes with size. Therefore, when designing microsystems, merely miniaturizing macroscopic systems is not a clever way to realize such systems. Scaling effects, i.e. of mass versus stiffness, and microscale effects, like surface tension and brownian noise, must be taken into account right on from the outset of the design process.

The close interaction between different 'energy domains' is also of fundamental importance to microsystems. An example is electrostatic forces, acting on the mechanical structure, thus involving both the mechanical domain and the electrical domain. While mechanical and electrical effects often are the keystones of the operational principles of microsystems, many systems involve effects from other domains, like the fluidic, thermal, optical, biological, or others.

From a historical perspective, most domains utilized in microsystems, like mechanics, are already well known and well explored, although miniaturization brings forward new effects, knowledge, and use. However, the close interaction between various domains demands something more than an understanding of each single domain: the understanding of the complex interaction between effects from the different domains acting on the complete microsystem is required. Although the full system can be analysed in detail using one of the many system level simulators available, the designers will always need simpler models, where more explicit relations between macro-

1

scopic parameters and functionality are preserved, for efficient optimization, failure mode prediction and etc. of designs.

Such models may be called macromodels. These are the attributes a macromodel should have, as defined by Senturia [3]:

- Preferably analytical, rather than numerical, permitting the designer to reason about the effects of design changes.
- Correct dependencies on device geometry and constitutive properties.
- Correct explicitly energy conservation and dissipation behaviour (that is, contains no dependent sources with mysterious energy sources).
- Covers both quasi-static and dynamical behaviour.
- Expressible in a simple-to-use form, either as an equation, a network analogy, or a small set of coupled ordinary differential equations.
- Easy to connect to system-level simulators.

In this work dealing with microsystems and macromodels, we are more focused on general aspects regarding macromodels than on specific aspects of microsystems. We are also emphasizing mechanical problems, although the methods we present are general in nature.

1.2   General simulation issues

Microsystems technology offers product developers a number of fascinating possibilities, but also challenges. Fully understanding how a microsystem device works generally requires insight across traditional engineering fields. The same is true for the modelling of microsystems.

Simple problems encountered in engineering can be solved by classical analytical methods. However, most realistic systems encountered are generally too complex to be solved analytically, and we have to use numerical methods instead. Such methods, characterised by partioning the original problem into a number of smaller, interconnected problems, have been known for a long time. However, it was not until major advances in computer-technology took place in the 50's and 60's, that the real development of such methods, like the finite element method and the boundary element method, took place [4], [5]. With the continouos improvements both in computer technology and in simulator code, these methods have become indispensable to modern engineering.

Today, there exist a number of CAD-tools capable of handling more than a single energy 'domain', e.g. which are capable of performing a mixed mechanical and electrical simulation. Some of these are targeted specifically at the Microsystems community (CoventorWare, IntelliSuite, SESES, CFD-ACE+MEMS, MEMS XPLORER) while others are more general (like ANSYS Multiphysics, FEMLAB, CFD-ACE).

An alternative to using mixed simulators is to express the system in terms of a single energy domain. It is, for example, quite possible to express mechanical system in terms of an electrical equivalent circuit [6]. We will discuss this possibility in a later chapter, since it offers the advantage that a designer can work in a single domain.

1.2.1 Earlier work in (macro-) modelling

Since this thesis is biased towards mechanics, it is natural to focus on the developments within the mechanics community. This involves, for example preference for FEM instead of BEM. However, many of the methods for creating macromodels are general in nature, and are not linked to a specific method.

The finite element method (FEM) is, in brief, a method where a system is discretized into a number of smaller subsystems. It is then assumed that the behaviour of each subsystem can be approximated by a simple solution (for example, a linear function). The subsystems are then interconnected in a proper way, effectively creating a set of coupled equations, where the subsystem solutions are parts of the total solution (piecewise linearization).

Present day numerical simulators, based on FEM and BEM are very powerful tools indeed for analyzing mechanical systems. They have been applied to create increasingly complex systems, again leading to increasingly large and complex models. This model complexity is determined by the degrees of freedom used, and the damping and nonlinearities in the system. However, early on it became apparent that the detail and complexity of many models where much greater than needed to reproduce the system behaviour within the range of interest, mostly because of excessive numerical partitioning of the system, which creates a complex topology [7]. In the field of finite element modelling, this was a topic as early as in the 60's, making researchers look for how to reduce the original size of the FE-model without loosing accuracy [8].

In structural mechanics, the discretization of a system can roughly be divided in two different categories, as is shown schematically in fig. 1.1. One alternative is to merely divide the structure into such small pieces that we can use the Cauchy-equations to describe the behaviour of the elements (the Cauchy-equations are the underlying governing differential equations in continuum mechanics). The other alternative is to divide the structure into larger elements, 'lumped' elements, where each element is essentially a well-known structure. Typical are beam elements, springs, dampers, and rigid bodies. Generally, the behaviour of such lumped elements are approximately described by beam theory, plate theory, rigid body theory, or other. However, these theories are all based on the continuum hypothesis (and thereby the Cauchy-equations) in one way or another.

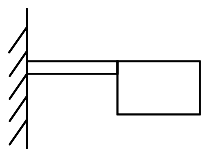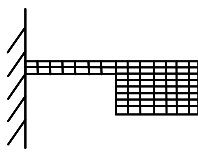We also note that there is a direct analogy with electrical systems, where

	'Lumped'	'Standard'
Elements based on:	Beam theory, rigid body, or other	The Cauchy-equations
# degrees of freedom (dof)	Low	Very high
Choice of dof	Dof's chosen by designer	Highly automatic
Accuracy	Depends on choice of dof's	Very good

Figure 1.1: Two main categories in mechanics for creating finite element models. For electrical systems / electrodynamics, similar categories exists.

the Cauchy-equations are replaced by Maxwells equations. The lumped elements can be resistors, inductors, and capacitances.

1.2.1.1 Lumped modelling

Lumped modelling has been very popular for creating macromodels, and it has been the de facto standard for creating such models also in the MEMS-community [9], [3]. It offers the designer the possibility to create a manageable model, where the elements normally are described in terms of analytical expressions. The latter facilitates reasoning and transparency regarding effects of design-parameter changes since the elements used are well understood and characterized.

The accuracy of lumped models, however, can be questioned in many cases since creating such models is a manual operation, which depends on the experience and insight of the designer. The designer's goal is to partition the system into as few elements as possible, while still capturing the essence of the system behaviour. Non-essential effects, that require large simulator resources can therefore be ignored in a lumped model. We note that nonlinear behaviour may be difficult to capture in lumped elements, requiring extensive physical intuition on part of the designer.

1.2.1.2 Transfer-function approximation

An alternative to formulating the systems as a set of differential equations is to use a transfer-function. A transfer-function is obtained by performing a Laplace-transformation and some matrix-operation on the FE-model of the

system. Hence, the function is expressed in the s-plane.

If the transfer-function is created on basis of a full FE-model, the function becomes large and complex, consisting of a large polynomial in both the numerator and the denominator. Such a function can easily be approximated by a number of methods. Well known are Padé-approximations [10] and Taylor-expansion.

Two major drawbacks are associated with the use of transfer-function (approximations). Firstly, the method is linear in nature, and is not valid for non-linear systems. Secondly, most simulators do not accept transfer-functions, and they must therefore be reformulated to a format that is accepted, typically a set of differential equations. However, this may prove to be difficult due to numerical issues for complex systems. Finally, a transfer-function often appears quite abstract, and is generally not very transparent in the form.

1.2.1.3 Model order reduction

As already mentioned, it was early on recognized that the complexity of (FE-) models where governed by topology, and not complexity of behaviour [7]. The overall goal is therefore to reduce the number of degrees of freedom in the models in such a way that they still represent the behavioural characteristics in a satisfactory manner. In finite-element modelling and mechanical engineering, the first attempts where focused on identifying structural properties by investigating the FE-model. One such method is Guyan reduction (or mass condensation) dating back to the 1960's [8].

A number of other methods have been utilized to automatically reduce the number of degrees of freedom in the systems. However, they all have the same general foundation, which is to project the original high-dimensional space, in which the model is presented in, onto a lower-dimensional space. This is often referred to as the projection framework.

One example of this procedure is to express the system in terms of the eigenvectors, and then disregard all but the eigenvectors corresponding to a small set of the lowest eigenvalues. In other words, the full system is projected onto a lower-dimensional space, whose basis-vectors are the eigenvectors corresponding to the lowest eigenvalues. A number of other methods for choosing basis-vectors in the lower-dimensional space also exists.

The projection framework has lately proved efficient in reducing large models. However, much of the work in this area appears to be focused on creating highly accurate reduced models rather than on creating transparent macromodels. In fig. 1.2, we have compared some properties of lumped modelling and the use of the projection framework.

1.2.1.4 Nonlinear systems

The problem of reducing nonlinear systems is considerably harder than re-
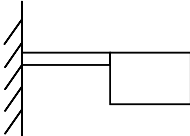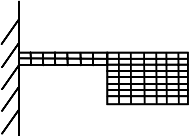
	Lumped modelling	Reduced-order modelling

		Full model	
		Elements	Cauchy
		#dof's	Very high
		Choice of dof's	Automatic
		Accuracy	Very good

	Lumped modelling	Reduced-order modelling	
Elements	Beam theory etc.	Complex / automated	
#dof's	Low	Low to medium	
Choice of dof's	Dof's chosen by designer	Highly automated	
Interpretation of dof's	Clear	Possibly obscure physical interpretation	
Accuracy	Depends on choice of dof's	Depends on reduction factor and reduction method	

Figure 1.2: Two main methods for creating reduced models, examplified by a mechanical system. General properties of the methods are shown.

ducing linear systems, even though the former can be viewed as a natural extension of the latter.

Among the approaches that exist for reducing nonlinear systems are piecewise linearization, Volterra series, and manifold methods. These methods are still in rapid development, and have apparently not yet reached their full potential. This is also true for the methods that are capable of creating macromodel (note that the terms "reduced model" and "macromodel" are not entirely identical).

In this thesis we have chosen to focus on manifold methods for reducing nonlinear systems. A first step towards invariant manifolds, namely the concept of the nonlinear normal mode, was introduced as early as in the 1960's [11]. Explained briefly, the nonlinear normal mode is a nonlinear extension of the linear normal mode (or eigenvector). A good review on nonlinear normal modes, including use and updated knowledge, can be found in [12].

We know that for a linear system excited in a single mode, the state of the system will always stay on the phase-plane of that mode. No other modes will be excited. Hence, the state of the system will always stay on a surface defined by the phase-plane of the excited mode. This surface is in fact an invariant manifold, since the motion of the system will always stay on the manifold (or surface). However, such invariant manifolds also exists for many nonlinear system. These surfaces are generally no longer planar, but curved, for the nonlinear system. The concept of invariant manifolds where apparently introduced as late as in the beginning of the 1990's to the field of mechanical engineering [13]. It is of interest to note that although the use of invariant manifolds was recently introduced to the field of mechanical engineering, these objects have been known in the mathematical community for a long period of time [14].

Manifold methods for reducing nonlinear structural problems have recieved a good deal of attention from researchers. However, much of the work is focused on identification of special effects and behaviour of small discrete or continuous systems (e.g [15], [16], [17], [18]). This is perhaps symptomatic of the relative recent introduction of the methods to mechanics. However, with more attention paid to this method, more of the work will be directed towards larger systems of more practical importance.

1.3   This work

We show in this work how large models, like FE-models with many degrees of freedom, can be reduced to give more compact models (reduced order modelling). To this end, we have studied the use of invariant manifolds for nonlinear conservative systems. Hence, we have investigated the accuracy of an asymptotic approach for finding the invariant manifold, and developed a design-parameter sensitive model. We also discuss how external forcing in

the systems should be treated, taking into account assumptions made in the invariant manifold theory and present an approach to deal with this problem. We have also analysed a nonlinear dissipative systems, using a numerical approach to obtain the manifold.

Most of these analyses are based on the modelling of an industrialized accelerometer and yielded valuable insigth into the behaviour of the microsystem. In addition, we have analysed squeeze-film damping, and shown how to represent simplified models of the squeeze-film damping in terms of electrical equivalents.

The lumped modelling approach has been applied to a resonator with electrostatic excitation and detection, and and investigated how electrical equivalents of the mechanical system can be built. Using electrical equivalents, we have demonstrated how the correct analogy gives a natural relation between the equivalent circuit and the mechanical topology. We also present the electrostatic transducer element in terms of both electrical analogies (the direct analogy and the mobility analogy).

Finally, we have analysed a newly proposed electromagnetic levitation system. This is the first complete analysis of such a system. The system has been analysed based on fundamental solutions of waves in waveguides, combined with a lumped modelling approach. The analysis demonstrates new effects and offers increased understanding of the system.

During the work on this thesis, the following papers have been published:

- Zhang, Z.L., Vitorovich, N., Westby, E., Wang, D.T.: *Notch fracture of MEMS sensors made of single crystal silicon*, 10th International Conference on Fracture (ICF'10), December 2001.
- Zhang, Z.L., Vitorovich, N., Westby, E., Wang, D.T.: *Notch fracture of MEMS sensors made of single crystal silicon,* First national conference on Computational Mechanics, Norway, MekIT'01, pp. 449-455, 2001.
- Westby, E., Fjeldly, T.A.:*Dynamical Equivalent-Circuit Modeling of MEMS with Squeezed Gas Film Damping*. Physica Scripta, Proc. of the 19th Nordic Semiconductor Meeting. Vol.T101, pp. 192-195, 2002.
- Westby, E., Fjeldly, T.A.:*Nonlinear Analytical Reduced-Order Modeling of MEMS*. Proc. of Modeling and Simulations of Microsystems 2002, MSM'02, pp. 150-153, 2002.
- Westby, E., Sangster, A., McErlean, E.:*Stability of a cavity based electromagnetic suspension system for micro-scale actuators*. J. of Electromagnetic waves and applications, Vol. 17, No. 9, pp.1331-1347, 2003.
- Westby, E.:*Nonlinear Reduced Modeling Of a Damped Dual-axis Accelerometer*. EuroSIME'03, pp. 161-164, 2003.

1.4   Outline of thesis

In chapter 2, we presented the subject of model order reduction, starting with reduction methods for linear systems. An example with squeeze-film damping is given. In chapter 3, several methods for reducing nonlinear conservative systems are presented. The concept of invariant manifolds is further elaborated on in chapter 4 and we present a method for treatment of external forcing. We analyse the accuracy of an asymptotic approach for creating the invariant manifold. A reduced model of an undamped dual-axis accelerometer is built. We also develope a method to create design-parameter sensitive models. We finish the topic of model order reduction by looking at nonlinear dissipative systems in chapter 5, where we also build a reduced model of a damped dual-axis accelerometer. The second main topic is lumped modelling. In chapter 6, we present some equations that are fundamental to mechanical and electrical engineering, following an analysis of electrical analogies of mechanical systems, including electrostatic transducer elements. The accuracy of the lumped models of the microresonator is analysed. In chapter 7 we analyse an electromagnetic levitation system. Finally, we discuss the topic of macromodelling and we draw some conclusions in chapter 8.

PART I

Model Order Reduction

Chapter 2
MOR: Linear Systems

The subject of this thesis is macromodelling of microsystem. That implies the creation of macromodels involving various domains. At least two main strategies for constructing compact models can be identified, and are here divided into the two categories:

- Model order reduction
- Lumped modelling

Model order reduction of a compact model typically start with a large, accurate, numerical model describing the system of interest. Based on a highly accurate, but large model, methodologies can be applied to reduce the size of the model. This will obviously also reduce the accuracy of the model, but many reduction methodologies are capable of reducing model size heavily while retaining a high degree of accuracy. These methodologies do generally have a strong mathematical foundation. They tend to be used in such a way that the reduced model contain typically hundreds of d.o.f.. Hence it is often difficult, if not impossible, to gain much physical insight into the physical system from the reduced model. This is not necessarily a limitation of the reduction methods, but may simply be a result of the way the methods are used (i.e. by giving priority to accuracy, and hence retain a relatively large number of d.o.f.)

Lumped modelling is somewhat opposite to the aforementioned. The methodology is based upon the use of analytical models and physical intuition. A number of simple designs invite for using and solving the governing equations directly. However, most systems are too complicated to be solved directly using analytical models. In many of these cases, there is a possibility of dividing the structure into a small number of simple substructures, where each substructures can be modelled by a simple analytical equation. This approach has proven very efficient in many cases. The approach can be examplified showing how it is used in mechanical engineering. An accurate approach would mean solving the Cauchy-equations over the full structure. This is generally solved numerically, using finite elements. Instead of using a large number of elements based on the Cauchy-equations, we identify simple substructures. Each substructure is typically masses, beams etc.. The behaviour of such structures can often be modelled analytically, and then made to form a single finite element. Hence, the structure is modelled by a small number of elements, each describing the behaviour of a substructure.

In electrical engineering, the parallel to this is the use of lumped inductors, resistors, and capacitances, and not the direct use of Maxwells equations.

Both model order reduction and lumped modelling have their advantages and drawbacks, of which a few were shown in fig. 1.2. Model order reduction tend to give models where parameter-dependency and physical intuition are not necessarily easily to deduce. Despite this, it is definitely an important area, due to possible automation in the methodology and ability to model effects that are lost using oversimplified lumped models (or analytical models with coarse approximations). Hence, an overview of some methods used for reducing models are given in the following. Reviewing these methods also gives basic understanding of compact models and their properties.

2.1   Linear systems

Systems can be described in a number of ways. A convinient way to describe linear dynamic systems is state-space description:

$$\dot{\mathbf{x}} = \mathbf{Ax} + \mathbf{Fu}$$
$$\mathbf{y} = \mathbf{Cx}$$

where we denote the state vector $\mathbf{x}$, the observation vector $\mathbf{y}$, system matrix $\mathbf{A}$, load matrix $\mathbf{F}$, and the observability matrix $\mathbf{C}$. The state-space description can of course also be used for nonlinear system, simply by replacing the matrix-operation by some kind of nonlinear function. However, we will at present consentrate on linear systems. A mechanical system, described in terms of finite elements, may be transformed from the usual description to a state-space description:δ

$$\delta \mathbf{F}_m \mathbf{u} = \mathbf{M}\ddot{\mathbf{x}}_m + \mathbf{D}\dot{\mathbf{x}}_m + \mathbf{K}\mathbf{x}_m$$
$$\begin{bmatrix} \dot{\mathbf{x}}_M \\ \ddot{\mathbf{x}}_M \end{bmatrix} = \begin{bmatrix} \mathbf{0} & \mathbf{I} \\ -\mathbf{M}^{-1}\mathbf{K} & -\mathbf{M}^{-1}\mathbf{D} \end{bmatrix} \begin{bmatrix} \mathbf{x}_M \\ \dot{\mathbf{x}}_M \end{bmatrix} + \begin{bmatrix} \mathbf{0} \\ -\mathbf{M}^{-1}\delta\mathbf{F}_m \end{bmatrix} \mathbf{u}$$

where $\mathbf{x}_m$ denotes the amplitude of the mechanical degrees of freedom. $\mathbf{M}$ denotes mass matrix, and $\mathbf{K}$ and $\mathbf{D}$ denotes the stiffness matrix and the damping matrix respectively. $\mathbf{I}$ is the identity matrix. Some distinct disadvantages of this formulation are that the size of the matrices are doubled, and certain properties are lost, like symmetry. These are evident computational and numerical drawbacks. Nevertheless, the formulation has advantages which may outweigh the drawbacks. Hence many of the methods described in the following rely on this formulation. It should also be noted that some systems are naturally of first order and are therefore naturally in this formulation.

2.1.1   S-plane analysis

In vibration analysis, the Laplace-transforms are important. Using the Laplace-transform, the system's response is evaluated as a function of frequency (or

the s-parameter). The most common Laplace-transform is:

$$\dot{x} = sx$$

This can be applied to the state-space description and one obtains (for simplicity we assume a single excitation, $u(s)$):

$$
\begin{aligned}
[s\mathbf{I} - \mathbf{A}]\,\mathbf{x}(s) &= \mathbf{F}u(s) \\
\mathbf{x} &= [s\mathbf{I} - \mathbf{A}]^{-1}\mathbf{F}u(s) \\
\mathbf{y} &= \mathbf{C}\mathbf{x} = \mathbf{C}[s\mathbf{I} - \mathbf{A}]^{-1}\mathbf{F}u(s) \\
\mathbf{H}(s) &= \frac{\mathbf{y}(s)}{u(s)} = \mathbf{C}[s\mathbf{I} - \mathbf{A}]^{-1}\mathbf{F}
\end{aligned}
$$

Since the s-parameter is complex, we note that the transfer-function, $\mathbf{H}(s)$, will also be complex. Hence the transfer-function gives us information about the system response from sinusoidal excitation, in terms of both amplitude and phase.

2.1.2 Eigenvalue analysis

Along with s-plane analysis, eigenvalue analysis is an important basic tool. Assuming we describe the system by the set of equations:

$$\mathbf{B}\dot{\mathbf{x}} = \mathbf{A}\mathbf{x}$$

we substitute:

$$
\begin{aligned}
\mathbf{x} &= \mathbf{v}e^{\lambda t} \\
\dot{\mathbf{x}} &= \lambda\mathbf{v}e^{\lambda t}
\end{aligned}
$$

which yields:

$$\lambda\mathbf{B}\mathbf{v} = \mathbf{A}\mathbf{v}$$

Which is the eigenvalue-problem. The solution of the eigen-problem gives the eigenvalue, λ_i, and the corresponding eigenvector, $\mathbf{v}_i$. Generally, this problem has as many solutions as it has d.o.f.'s. Note also that both eigenvalues and eigenvectors may consist of both real and imaginary components. By placing all the eigenvectors in a matrix, we have obtained the transformation matrix from the eigenroom (d.o.f.'s=q's) to the k-room (d.o.f.'s=x's).

$$
\begin{aligned}
\mathbf{x} &= \begin{bmatrix} \mathbf{v}_1 & \mathbf{v}_2 & ... & \mathbf{v}_N \end{bmatrix}\mathbf{q} \\
\mathbf{x} &= \mathbf{V}\mathbf{q}
\end{aligned}
$$

The system originally posed in the k-room, may likewise be expressed in the eigenroom. With proper normalization of the eigenvectors, the system

13

matrix becomes a diagonal matrix with the eigenvalues in the diagonal:

$$
\begin{aligned}
\dot{\mathbf{x}} &= \mathbf{A}\mathbf{x} + \mathbf{F}\mathbf{u} \\
\mathbf{V}^{-1}\mathbf{V}\dot{\mathbf{q}} &= \mathbf{V}^{-1}\mathbf{A}\mathbf{V}\mathbf{q} + \mathbf{V}^{-1}\mathbf{F}\mathbf{u} \\
\dot{\mathbf{q}} &= \mathbf{A}^q\mathbf{q} + \mathbf{F}^q\mathbf{u} \\
\dot{\mathbf{q}} &= \begin{bmatrix} \lambda_1 & 0 & & 0 \\ 0 & \lambda_2 & & 0 \\ & & \ddots & \\ 0 & 0 & 0 & \lambda_N \end{bmatrix} \mathbf{q} + \mathbf{F}^q\mathbf{u}
\end{aligned}
$$

Returning to the transfer-function, we note that this is an extremely handy form, since:

$$
\begin{aligned}
\mathbf{H}\left(s\right) &= \mathbf{C}^q \left[s\mathbf{I} - \mathbf{A}^q\right]^{-1} \mathbf{F}^q \\
\mathbf{H}\left(s\right) &= \begin{bmatrix} \sum_j C_{1,j}^q \frac{1}{s-\lambda_j} F_j^q \\ \sum_j C_{2,j}^q \frac{1}{s-\lambda_j} F_j^q \\ \vdots \\ \sum_j C_{K,j}^q \frac{1}{s-\lambda_j} F_j^q \end{bmatrix}
\end{aligned}
$$

From this equation the importance of the eigenvalues becomes apparent.

2.2 Transfer-function approximation

The transfer-function may also be formulated as a rationale (for simplicity we assume a single output):

$$
\begin{aligned}
\mathbf{H}\left(s\right) &= \sum_j C_j^q \frac{1}{s - \lambda_j} F_j^q \\
\mathbf{H}\left(s\right) &= \frac{a_1 + a_2 s + \ldots + a_N s^{N-1}}{b_1 + b_2 s + \ldots + b_N s^{N-1} + s^N}
\end{aligned}
$$

We note that the goal of model order reduction is to construct a simpler transfer-function approximating the exact transfer-function as accurately as required.

2.2.1 Reduction through choice of eigenvalues

With the transfer-function in the form of eigenvalues, we see that one method of reducing the transfer-function is to make a selection of eigenvalues to re-

tain. Hence the transfer-function becomes:

$$\mathbf{H}_{red}(s) = \sum_k C_k^q \frac{1}{s - \lambda_k} F_k^q \qquad k \in \text{retained modes}$$

We note that for systems with purely imaginary eigenvalues (i.e. undamped mechanical systems), the reduced transfer-function is exact at the retained resonance frequencies (eigenvalues). At the same time we see that there is no assurance of accuracy at frequencies different from the chosen eigenvalues. This method has been well-known and commonly used in the MEMS-community [19], [20], [9].

One drawback of the method is that the accuracy is only guaranteed at the resonance-frequencies chosen. This implies that the simplified transfer-function is inaccurate at static behaviour. Obviously, the accuracy also depends on the number of chosen modes. It is common practice to include typically the 6 lowest modes [21].

2.2.2 Reduction through moment-matching

Another, more predictive method, is to analyse the transfer-function rationale. By performing a Taylor-expansion of the full rationale, an approximate function may be constructed:

$$\mathbf{H}(s) = \frac{a_1 + a_2 s + \ldots + a_N s^{N-1}}{b_1 + b_2 s + \ldots + b_N s^{N-1} + s^N}$$

$$\mathbf{H}_{red}(s) = \mathbf{H}(0) + \frac{d\mathbf{H}(s)}{ds} s + \frac{1}{2} \frac{d^2 \mathbf{H}(s)}{ds^2} s^2 + \cdots$$

A major drawback of this method is that most simulators do not accept the transfer-function directly, so it must be rewritten. When writing the transfer-function as a sum of simple first-order systems, it is quite simple to construct, for example an electrical circuit with the same behaviour. Hence it is correspondingly easy to create a state-space model of the system. However, when expreessing the transfer-function in terms of a rationale, it becomes increasingly difficult to find the roots of the numerator and the denominator with increasing order. Constructing a state-space model from a rationale therefore soon becomes a numerically extremely difficult task.

2.2.3 Matching at frequencies

Another method of constructing a simple transfer-function is by establishing a simplest possible function that matches the full transfer-function at given set of frequencies. The disadvantages of this method is much like those encountered in 2.2.1, using the method of choosing a set of eigenvalues. However, also this method suffers from the difficulty of constructing a first-order system from the reduced transfer-function.

2.3   Projection framework, reducing space

2.3.1   Using eigenvectors

Above we presented methods that may be used for simplifying the full transfer-function. It is of interest to note that these methods may be expressed differently by focusing on a coordinate system representation instead of the transfer-function.

This is achieved by projecting the original high-dimensional system onto a lower-dimensional space. This lower-dimensional space may, for example, be spanned by a subset of the eigenvectors. The resulting transfer-function then becomes equivalent to what is obtained by attacking the transfer-function directly and selecting a set of eigenvalue, like presented in 2.2.1. Mathematically, this is done by constructing a matrix, mapping the reduced state-space vector, $\mathbf{q}_{red}$, onto the full-size state-space vector:

$$\mathbf{x} = \mathbf{V}_{red}\mathbf{q}_{red} = \begin{bmatrix} (v_1)_1 & (v_2)_1 & \cdots & (v_n)_1 \\ (v_1)_2 & (v_2)_2 & & (v_n)_2 \\ \vdots & & \ddots & \\ (v_1)_N & (v_2)_N & & (v_n)_N \end{bmatrix} \mathbf{q}_{red}$$

Here we note that the transfer matrix is of size $N \times n$, where N is the number of d.o.f. in the full system and n is the number of d.o.f. in the reduced system. In the case of using a set of eigenvectors as reduced basis, it is apparent that the columns in $\mathbf{V}_{red}$-matrix consists of the chosen eigenvectors. We also note the mapping from the full space onto the reduced space:

$$\mathbf{q}_{red} = \mathbf{U}_{red}\mathbf{x} = \begin{bmatrix} (u_1)_1 & (u_2)_1 & \cdots & (u_N)_1 \\ (u_1)_2 & (u_2)_2 & & (u_N)_2 \\ \vdots & & \ddots & \\ (u_1)_n & (u_2)_n & & (u_N)_n \end{bmatrix} \mathbf{x}$$

The construction of the reduced model then proceeds by replacing the original full state-space vector with the mapping functions:

Full model   Reduced model
$\dot{\mathbf{x}} = \mathbf{A}\mathbf{x} + \mathbf{F}\mathbf{u}$ $\Rightarrow$ $\mathbf{U}_{red}\mathbf{V}_{red}\dot{\mathbf{q}} = \mathbf{U}_{red}\mathbf{A}\mathbf{V}_{red}\mathbf{q} + \mathbf{U}_{red}\mathbf{F}\mathbf{u}$
$\mathbf{y} = \mathbf{C}\mathbf{x}$ $\Rightarrow$ $\mathbf{y} = \mathbf{C}_{red}\mathbf{V}\mathbf{q}$

When a set of eigenvectors are used as the reduced basis, calculations show that this is equivalent to the transfer-function approximation in 2.2.1. Although it was assumed that the basis vectors of the reduced space was defined by eigenvectors, this is no requirement, since the formalism is quite general.

2.3.2   Krylov-subspace

In the above, the projection framework was examplified by using eigenvectors

for defining the basis vectors of the reduced space. However, other suitable ways of defining the reduced space exists. A method that has shown good results is the use of Krylov subspace [20], [22], [23]. This method is parallel to the moment-matching of the transfer-function. The difference is that instead of finding the moments of the transfer-function, the corresponding generalized vector is found. This means that a k'th order Krylov subspace matches the k first moments of the transfer-function. The resemblance between the Krylov subspace (found via the Lanczos method) and Padé-approximations of the transfer-function is shown clearly in [24]. Several papers have investigated the use of Krylov subspace methods, using Lanzcos or Arnoldi-methods, e.g. [25], [22].

2.3.3 Proper orthogonal modes

Proper orthogonal decomposition, or Karhunen-Loève decomposition, is primarily a statistical formulation, finding an optimal distribution of energy from a set of measurement histories. A historical review and a physical interpretation of proper orthogonal modes can be found in [26]. It is a common tool in turbulence studies [27], and it has recently also received attention from other communities, e.g. the MEMS-community [28], [21]. The method is presented for systems with a finite number of degrees of freedom, see [29] for more details. The set of measurement histories can be obtained either via simulation or via experimental observation. The set of measurement histories are placed in an $M \times N$ ensemble matrix ($\mathbf{X}$), where N is the number of degrees of freedom, while M is the number of timesteps the system has been observed. From the ensemble matrix one can thus obtain the $N \times N$ correlation matrix ($\mathbf{R}$):

$$
\begin{aligned}
\mathbf{x}\left(t\right) &= \begin{bmatrix} x_1\left(t\right) & x_2\left(t\right) & \ldots & x_N\left(t\right) \end{bmatrix} \\
\mathbf{X} &= \begin{bmatrix} \mathbf{x}\left(t_1\right) & \mathbf{x}\left(t_2\right) & \ldots & \mathbf{x}\left(t_M\right) \end{bmatrix}^T \\
\mathbf{R} &= \mathbf{X}^T \mathbf{X}
\end{aligned}
$$

(The means are sometimes subtracted from the time history data). The eigenvalues and eigenvectors of the correlation matrix corresponds to the proper orthogonal values and proper orthogonal modes of the system. A selection of the proper orthogonal modes (POM) may now serve as the basis for the reduced model. One common criterion for choosing POMs is to select those POMs with corresponding proper orthogonal values that sums up to at least 99% of the sum of all the proper orthogonal values ([30], [27]).

It is worth mentioning that using the singular value decomposition (SVD) gives the same results as using the Karhunen-Loève approach for finding the POMs [29].

A drawback of using POMs is, however, that it relies on measurement histories. One problem is obviously that these measurement histories must be

created somehow, either by simulation of the full system or by experimental observation, with the latter possibly being difficult or impossible in the context of MEMS. Secondly, the measurement histories should represent results obtained under all different external influences.

2.4   Guyan reduction

In mechanics, Guyan reduction is a well-known method for reducing models, dating back to the 60's [8]. It is implemented in the commercial finite element program ANSYS. The method is based on dividing the degrees of freedom into masters and slaves. The principal idea is that for low-frequency modes, the inertia forces on slave d.o.f.'s are much less important than the elastic forces transmitted by the master d.o.f.'s [4]. In other words, this means that the slave d.o.f. move in a quasi-static manner. This methodology is, despite being fully automatic, rather coarse, meaning that reduction by a factor of only 5-10 can be expected with good accuracy compared to e.g. a factor in the hundreds for Krylov methods, [31], [32], and [4].

2.5   Example: squeeze-film damping

2.5.1   Introduction

Modelling of MEMS structures often involves multi-domain simulations. One of the domains encountered is the fluidic domain, where gas film damping is of importance for a wide range of systems. This is often, if not always, encountered along with the mechanical domain. There are obvious advantages to having simplified models of systems or subsystems available. Also the advantages of describing the various domains in a consistent manner have been mentioned. In [33] we have shown how squeeze-film damping can be described in a compact fashion using electrical equivalents. This part of the thesis is largely based on [33].

A popular solver for the electronic domain is the circuit simulator SPICE. This simulator is capable of dealing with analog and highly nonlinear elements. In the present work, we have chosen to use SPICE, which means that the mechanical problem must be reformulated in terms of an electrical equivalent circuit. When transforming a mechanical system into an electrical equivalent, we have two choices of mapping, either the flow-voltage analogy ($f \rightarrow V$), or the effort–voltage ($e \rightarrow V$) analogy. Here, the $f \rightarrow V$ mapping is preferred (a more thorough discussion regarding mechanical systems and their electrical equivalents is found in chapter 6). Considering, for example, a simple mass-spring-damper element, the mapping should be quite straight forward, see fig. 2.1.

One main characteristic of many silicon microstructures is that the moving surfaces are often very close to other surfaces. This means that if one surface
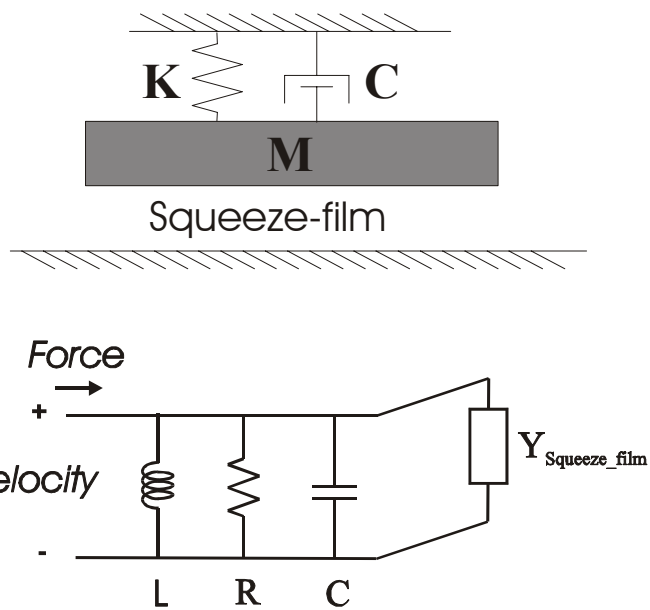
Figure 2.1: Shown is a simple mechanical system with squeeze-film damping. Below is the electrical equivalent circut (in the $f \rightarrow V$ mapping). $L = \frac{1}{K}$, $R = \frac{1}{C}$, and $C = M$.

moves against another, and the gap is small relative to the surface dimensions, the gas in between behaves as a squeezed gas film. Analytical solutions of the governing equations show that the fluid adds an effective spring and a viscous damper to the mechanical system. The effective spring and viscous damper are frequency-dependent. Describing the system in an electrical equivalent in the $f \rightarrow V$ analogy, the squeeze-film effect may be represented represented by an infinite ladder-like circuit with elements described analytically [34]. We have developed an approximate representation of the ladder which only requires a small number of elements. This is done through a careful selection of elements including suitable weighting factors. Finally, we classify some mass/spring systems and discuss what consequences the different systems will have upon the modelling.

2.6   Squeeze-film damping

Before demonstrating the capabilities of the reduced model, squeeze-film damping is more thoroughly presented. Starting from the Navier-Stokes equation for fluids, the continuity equation, the ideal gas law, and some simplifying assumptions, the Reynolds equation valid for squeezed films can be derived. The assumptions are as follows [35],[36]:

- The gap is always small relative to the lateral extent of the moving plate.
- The motion of the plate is sufficiently slow, so that we can treat the gas as moving under Stokes flow.
- The gas film has no pressure gradient in the direction perpendicular to the plate.
- The lateral flow has a Poiseuille-like velocity profile (parabolic profile with zero transverse velocity at the plates).
- The gas obeys the ideal gas law.
- The system is isothermal, i.e., any temperature rise due to gas compression or to viscous dissipation, or any temperature drop due to gas dilation is quickly compensated by heat flow to or from the walls.

To simplify further, it is assumed that the amplitude of the plate displacement δh is small relative to the mean distance h between the plates, which means that the pressure variation δp in the film is small compared to the ambient pressure P_a (small-signal approximation). With these assumptions, the Reynolds equation for the gas in the squeezed film becomes

$$\nabla^2 \psi - \sigma_{static} \frac{\partial}{\partial t} \psi = \sigma_{static} \frac{\partial}{\partial t} \varphi \tag{2.1}$$

For a rectangular plate, $\sigma_{static} = \frac{12\mu \cdot L_W^2}{h^2 P_a}$ is the so-called static squeeze number, L_W is the shortest of the rectangular plate dimensions, μ is the gas viscosity, and $\psi = \frac{\delta p}{P_a}$ and $\varphi = \frac{\delta h}{h}$ are the relative (dimension-less) pressure and

gap perturbations, respectively.

The temporal behaviour of the film response can easily be found from eq. 2.1 for the case of a simple harmonic motion excitation. The corresponding in-phase and out-of-phase force components, F_1 and F_0, respectively, become (integrating the pressure over the plate area A):

$$F_1 = P_a \int \psi_1 \cos \tau dA \tag{2.2}$$

$$F_0 = P_a \int \psi_0 \sin \tau dA \tag{2.3}$$

Here F_0 acts as a damper, while F_1 acts as a spring.

For a rectangular plate of length L_L and width L_W, the spring and damping coefficients can be expressed as follows [37]:

$$K_{fluid} = \frac{64\sigma^2 P_a A}{\pi^8 h} \sum_{m,\ odd} \sum_{n,\ odd} \frac{m^2 + \frac{n^2}{\beta^2}}{(mn)^2 \left(\left(m^2 + \frac{n^2}{\beta^2} \right)^2 + \frac{\sigma^2}{\pi^4} \right)} \tag{2.4}$$

$$C_{fluid} = \frac{64\sigma P_a A}{\pi^6 h \omega} \sum_{m,\ odd} \sum_{n,\ odd} \frac{m^2 + \frac{n^2}{\beta^2}}{(mn)^2 \left(\left(m^2 + \frac{n^2}{\beta^2} \right)^2 + \frac{\sigma^2}{\pi^4} \right)} \tag{2.5}$$

Here $\beta = \frac{L_L}{L_W}$ ($L_L \geq L_W$) is the plate aspect ratio, which should always be unity or larger. We also note that the frequency-dependant squeeze number is one of the coefficients that govern the behaviour of the spring constant and the viscous constant. Plots of the spring constant and the viscous damping constant for some common parameters are shown in fig. 2.2.

Note that the spring-effect shown here is the result of the viscous forces opposing the motion of the fluid, and is not caused by inertial forces, which we neglected earlier.

Plots of the forces associated with the spring and the damping are shown in fig. 2.3. We define the cutoff frequency, as the frequency where the damping and spring forces become equal. It can be estimated to first order as $\omega_{cutoff} = \frac{(1+(\frac{1}{\beta})^2)\cdot\pi^2}{\sigma_{static}}$.

2.7 Electrical equivalent circuit

The two analogies that can be used for deriving an electrical equivalent circuit for a mechanical system are shown in table 1. For a general one-dimensional mass-spring system modelled in the $f \rightarrow V$ analogy, the electrical equivalent circuit is shown in fig. 2.4.

The fluidic forces are represented here as $R\_f(s)$ and $L\_f(s)$, where the s indicates that there is a frequency-dependence (in the notation of Laplace transforms). The resistance R represents damping by other causes, e.g. in-
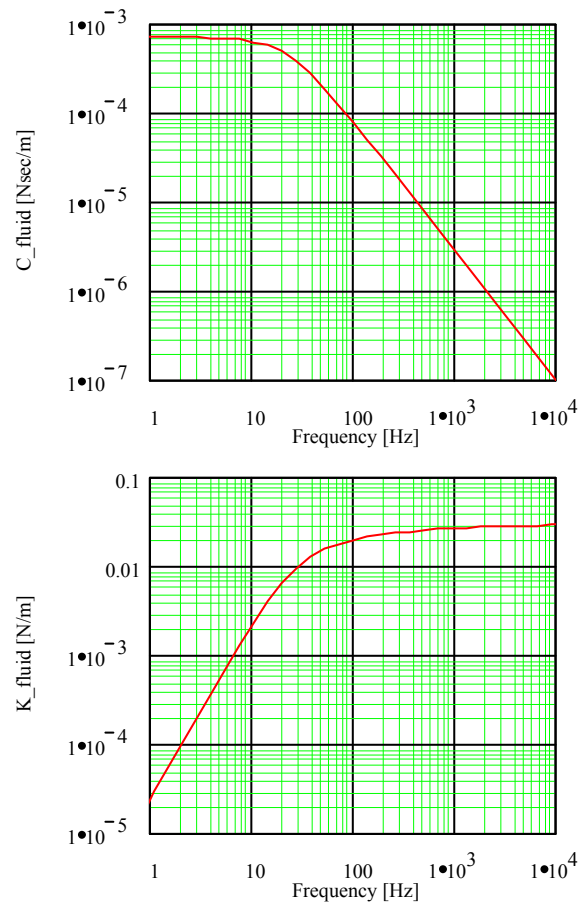
21

Figure 2.2: Above: Damping coefficient plotted against frequency. Below: Spring coefficient plotted against frequency.

Mech. quan	Electrical equivalent	
	f→V analogy	e→ V analogy
F, Force	i, Current	V, Voltage
v, Velocity	V, Voltage	i, Current
M, Mass	C, Cap.	L, Ind.
C, Damping	R^{-1}, Cond.	R^{-1}, Cond
K, Stiffness	L^{-1}, Inv. ind.	C^{-1}, Inv. cap.

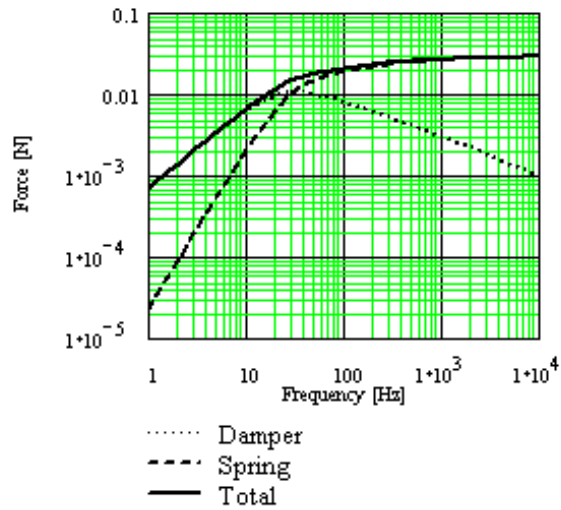Table 1.: Electrical - Mechanical analogies.

Figure 2.3: Force arrising from the fluidic damper plotted against frequency. The same is done for the spring and the total force from the fluid.
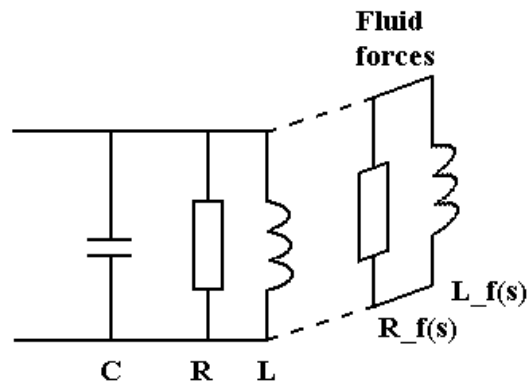

Figure 2.4: Electrical equivalent of mass-damper-spring system, with fluidic forces.
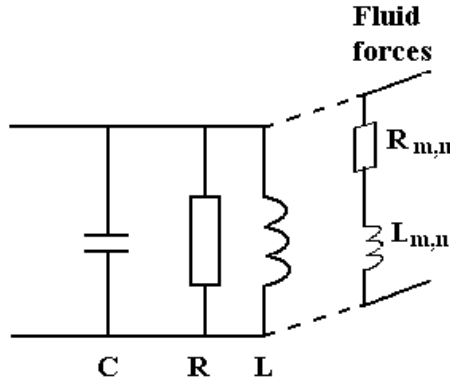
Figure 2.5: Ladder-like equivalent circuit of fluidic forces.

ternal damping in the spring. Since frequency-dependent parameters, such as those associated with the fluid, are not readily acceptable in many solvers, e.g. SPICE, a motivation exists for reformulating the problem in terms of suitable electrical equivalents.

2.7.1 Electrical equivalent of fluid forces

Veijola et al. [34] reformulated the expressions for the fluidic forces to circumvent the use of frequency-dependent parameters. This was done, however, at the cost of introducing an infinite array of circuit-elements. Hence, the rewritten form will have a ladder-like representation of a resistor and an inductor at each step, as shown in fig. 2.5. The circuit elements of the ladder can be expressed as:

$$L_{m,n} = (mn)^2 \frac{\pi^4 h}{64 A P_a}$$

$$R_{m,n} = (mn)^2 (m^2 + \frac{n^2}{\beta^2}) \frac{\pi^6 h^3}{768 A L_W^2 \eta}$$

$$(m, n = \text{odd})$$

$$(\sigma = \frac{12 \eta L_W^2}{P_a h^2} \omega)$$

2.7.2 Reduced series and approximation

In practice, we are interested in finding approximate representations for the infinite ladder of the exact solution. Analysing the equivalent in fig. 2.5, we find that at low frequencies (below cutoff), the forces can be represented quite well by retaining only a few low-order steps (elements) of the ladder. As we add elements, the accuracy gradually improves also at higher frequencies. A

(m,n)	$(1,1)$	$(1,3)$ $(3,1)$	$(1,6)$ $(6,1)$	$(1,17)$ $(17,1)$
$B_{m,n}$	1	1	3.4	11.5
(m,n)	$(1,53)$ $(53,1)$	$(1,167)$ $(167,1)$	$(1,265)$ $(265,1)$	$(1,800)$ $(800,1)$
$B_{m,n}$	37	128	380	1200

Table 2.

complicating factor is that the number of elements needed to obtain a given accuracy will depend on the geometry of the plate, as represented by the plate aspect ratio β. Figure 2.6 shows the number of elements needed to obtain an accuracy of 5% versus frequency for $\beta = 1$ (square plate). We see that above the cutoff frequency, the complexity of the equivalent soon makes this model impracticably complicated.

On the other hand, we find that a comparable accuracy can be obtained by selecting a subset of elements, letting each represent an average of all the elements in its vicinity. To sum up the total effect, each element of the subset is given a suitable weighting factor to account for all the elements omitted in the subset. Using this technique, the number of elements needed to obtain the desired accuracy is drastically reduced as seen in fig. 2.6. In this case, the following sequence of elements was chosen:

$$\sum_{m,n} e_{m,n} \cong \sum_{m}^{selected} e_{m,1} \cdot B_{m,1} + \sum_{n}^{selected} e_{1,n} \cdot B_{1,n} \qquad (2.6)$$

where $B_{m,n}$ are the weighting factors and the elements are defined as

$$e_{m,n} = (R_{m,n} + L_{m,n} \cdot s) \qquad (2.7)$$

The selected values of m and n, together with the weighting factors are shown in table 2 for a selection that will guarantee an accuracy of 5% for the entire frequency range from dc to $10^4 \cdot f_{cutoff}$ for all plate aspect ratios. We note that the highest accuracy is found for small values of β (≤ 1.5) or for large values ($\beta \geq 25$), in which case the number of elements in the selection can be reduced further. In the above discussion, we have not included boundary effects that may affect the properties of the squeezed gas. However, it has been shown that such effects can be incorporated by approximate techniques [38].

2.8   Design and simulation issues

Using the above model for fluidic damping, we can classify different mass/spring
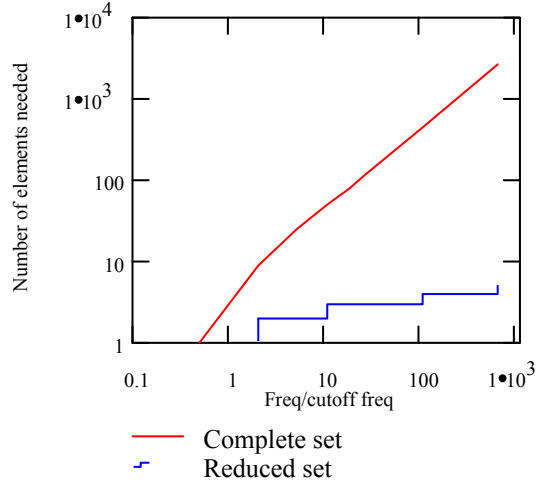
Figure 2.6: Number of elements needed for a 5% accuracy, plotted against normalized frequency. Starting with the complete ladder-like solution, we include all elements up to $e_{MN\max,MN\max}$ which satisfies the 5% accuracy requirement. The same is done for the reduced ladder subset when the element selection is optimized for a minimum number of elements.

systems according to their resonance frequency $f_{MS} = \frac{1}{2\pi}\sqrt{\frac{K}{M}}$ relative to the squeeze film cutoff frequency f_{cutoff}:

1) Highly damped $f_{MS} << f_{cutoff}$
2) Lightly damped $f_{MS} >> f_{cutoff}$
3) Medium damped $f_{MS} \tilde{=} f_{cutoff}$

2.8.1 Highly damped

Systems that have their main response below the cutoff frequency, can be modelled quite precisely using a small number of elements in the approximate ladder discussed above. In fact, even with one element a good representation is obtained. However, it should be noted that with only one element, the description close to and above the cutoff will degrade significantly. For such accelerometers, this may give significant errors in the simulated behaviour, since an additional resonance top for the system above cutoff will be missed. However, this can be rectified by adding a few more elements.

If the fluidic spring effect is insignificant or the frequency is sufficiently low, the squeeze-film ladder can be replaced by a simple resistor.

2.8.2 Lightly damped

Above the cutoff frequency, the damping decreases with increasing frequency (see fig. 2.2). Hence, for $f_{MS} >> f_{cutoff}$ the transfer-function of the system will not be flat at frequencies below f_{MS} (assuming that fluidic dissipation

is dominant). We assume that the system's Q-factor is large, and that the operating frequency will be close to the mechanical resonance. Then, for a model covering the frequency range from DC up to and above the mechanical resonance, an approximation should be used, for example the type shown in 2.7.2.

If only the response close to resonance is needed, it may be sufficient to use 2 elements in the representation.

If the fluidic damping is much smaller than the damping in the intrinsic mass/spring system, it is sufficient to model the fluid as a constant spring.

2.8.3   Medium damped

For a system operating at frequencies close to the cutoff frequency, the model must describe fully the behaviour of the fluid. This means that the fluid must be represented by several elements. However, two elements may be sufficient providing that the frequency-range is sufficiently small. Basically this constitutes the same problem as in the modelling of a resonator, except that the approximation of disregarding the fluidic damping cannot be made.

2.9   Discussion and conclusion

In the first part of the chapter, we presented methodologies for model order reduction. Some of the methods are based on the approximation of the transfer-function, while others have their basis in the projection framework. The principles behind the reduction methods are dissimilar and the reduced model's properties may therefore vary distinctly with reduction method. Hence a knowledge of various methods are of importance.

We have analysed the fluidic forces that act on a mass/spring system working against a nearby surface, with a thin gas-filled gap separating them. We have shown how the frequency dependent fluidic forces can be approximately represented by a ladder type equivalent circuit with a finite number of steps (elements), rendering systems with fluidic damping suitable for analysis by means of circuit simulators such as SPICE. We have classified mass/spring systems with fluidic damping into three categories, depending on the relative magnitude of the mass/spring resonant frequency and the fluidic cutoff frequency, and determined which additional simplifications (if any) can be made in each case. The present model is a small-signal one, but it is still applicable for realistic microdevices. It is also pointed out that the model is based on the exact solution of the Reynold's equation for squeeze-film, which is only valid for a harmonic motion.

In this example, the reduction has not been strictly based on a mathematical blackbox-style methodology, but rather on an analysis of the fluidic system. It has also become apparent through the analysis, that the reduction of the fluidic system is strongly linked with the properties and the behaviour

of the interacting domain, i.e. the mechanical system. Thus we obtain an increased knowledge of the full system, leading to an increased understanding of properties required from the reduced model. This knowledge may in turn be applied to create an optimally reduced model. Combining this with the analytical expressions of the series elements, which were the basis of the reduced model, the model also becomes transparent in the sense that parameter-dependency of the reduced elements can be deduced.

Chapter 3
MOR: Nonlinear Systems

The importance of normal modes in linear dynamical systems is indisputable. They are used to decouple the governing equations of motions, and to evaluate the system response. Furthermore, linear superpositioning can be used in cases where nonlinearities are insignificant. In the example related to modelling squeeze-film damping, a reduction scheme was applied to make the model more compact. One of the more important approximations that was made, was regarding linearities. In fact, it was assumed that the squeeze-film damping model was linear. Looking at the theory, it is clear that nonlinearities do exists and are potentially of great importance [35], [39]. We shall in the following look more at weakly nonlinear systems and how such systems can be reduced. This shall be done without a focus on the squeeze-film damping, but rather on general systems.

In many cases, neglecting nonlinearities in a model is a decent approximation. This is e.g. very often done analysing mechanical systems. Cases may arrise, however, where nonlinearities cannot be neglected. This is especially true in microsystems, where there exists designs that rely on nonlinear effects (see e.g. [40] and [41]).

The problem of generating compact models for nonlinear systems is much harder than for linear problems. One of the main reasons for that can be seen by looking at a nonlinear system:

$$\begin{aligned}
\dot{\mathbf{x}} &= \mathbf{A}(\mathbf{x})\,\mathbf{x} + \mathbf{F}\,\mathbf{u} \\
\mathbf{y} &= \mathbf{C}\,\mathbf{x}
\end{aligned}$$

From the equation it is clear that linear eiqenvectors do not exist, since the eigenvectors will be state-dependent. Likewise will moment-matching methods fail, since the moments depend upon the state of the system, also this due to the state-dependency of the system matrix $\mathbf{A}(\mathbf{x})$. The concepts, howevever, are still of importance, either used directly or as the basis of slightly more advanced concepts. In the following, some methods used for reducing weakly nonlinear systems are presented.

3.1 Piecewise linear models

In the previous chapter, the projection framework was presented, where the reduced basis vectors are found by considering the linear system. We are here, however, dealing with a nonlinear system, meaning that the reduced basis vectors will be functions of the state. These functions can be represented by piecewise constant functions. Using piecewise constant basis vectors, the
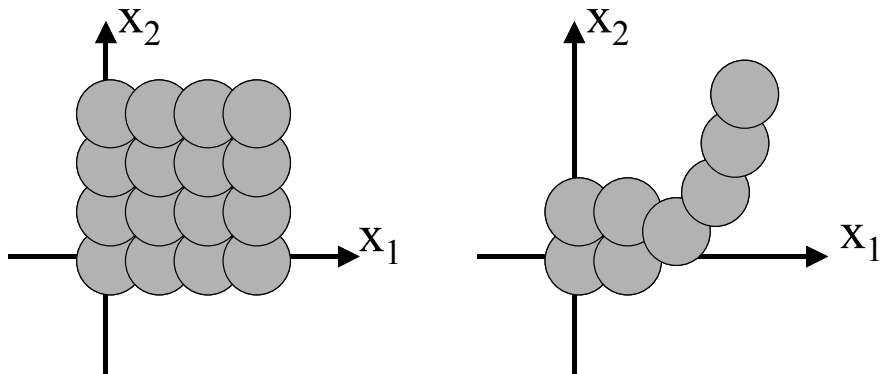
Figure 3.1: Left side shows how a number of discrete system matrices can reflect the nonlinear system. Right side demonstrates how the efficiency can be improved by only mapping the discrete system matrices that are "needed".

reduced system matrix becomes a piecewise constant function. Thus, the state-space model has become a piecewise linear model. Such a methodology has been presented in [22] and [42], where moment-matching via the Krylov subspace was applied to find the reduced basis vectors. Left side in fig. 3.1 shows how a number of discrete system matrices can describe the reduced nonlinear system. It is apparent, however, that the number of discrete system matrices may be unnecessarily large. Therefore, instead of calculating all possible discrete system matrices, a training input can be applied, and whereby only the "necessary" space is mapped by discrete system matrices [22], see right side of fig. 3.1. The methodology appears to be promising, and quite accurate results have been demonstrated [22].

3.2   Truncation

A method that in the past has been presented in the MEMS-community is simple truncation ([43], [44]). The methodology can in certain ways be compared to a projection framework method. Often, the first few eigenvectors (or linear normal modes) are used as the reduced basis vectors, equivalent to what would have been done for a linear system. The eigenvectors are found by disregarding nonlinear effects. The truncation then proceeds by simply disregarding everything but the reduced basis. An example of this is shown below, where the system is presented in the eigenspace. For simplicity, we consider a model with only 2 degrees of freedom. The full system is nonlinear

in displacement and is:

$$\begin{bmatrix} \ddot{q}_1 \\ \ddot{q}_2 \end{bmatrix} = \begin{bmatrix} -\omega_1^2 & 0 \\ 0 & -\omega_2^2 \end{bmatrix} \begin{bmatrix} q_1 \\ q_2 \end{bmatrix} + \begin{bmatrix} -a & -b & -c \\ -d & -e & -f \end{bmatrix} \begin{bmatrix} q_1^2 \\ q_1 q_2 \\ q_2^2 \end{bmatrix} \quad (3.1)$$

By keeping mode 1, and disregarding mode 2, we get the reduced model:

$$\begin{bmatrix} \ddot{q}_1 \\ 0 \end{bmatrix} = \begin{bmatrix} -\omega_1^2 & 0 \\ 0 & 0 \end{bmatrix} \begin{bmatrix} q_1 \\ 0 \end{bmatrix} + \begin{bmatrix} -a & 0 & 0 \\ 0 & 0 & 0 \end{bmatrix} \begin{bmatrix} q_1^2 \\ 0 \\ 0 \end{bmatrix}$$

$$\ddot{q}_1 = -\omega_1^2 q_1 - a q_1^2$$

However, by simple comparison of the full and the reduced model, it is clear that the reduction method does not handle nonlinearities in a proper way. Say, for instance, that mode 1 is initially excited. That would, according to the reduced model, mean that mode 2 would have no amplitude, regardless of how large the amplitude of mode 1 is. Looking at the full model, however, it is clear that there will be energy-transfer between (the linear) mode 1 and 2. This is neglected in such a simple truncation scheme. It can therefore be concluded that the truncation methodology cannot handle general nonlinearities in a proper way.

The technique can be enhanced by performing additional simulations of the complete system, where unmodelled nonlinear effects in the truncated mode set can be obtained [45]. Normally, this may lead to a large number of simulations.

3.3   Proper orthogonal modes

Proper orthogonal modes (POMs) have been presented in 2.3.3. The method for identifying the POMs are the same whether the system is linear or nonlinear. However, utilizing the method on nonlinear systems have certain implications.

Having selected a set of POMs, they now act as the reduced basis. In this manner, the reduction is linear and related to the truncation scheme presented above in 3.2. In fact, the only difference is how the reduced basis vectors are chosen. In the section presenting the truncation scheme (3.2), we used linear eigenvectors, whereas here we use the POMs. Since the choice of POMs are made using an energy criterion based on test-results, it appears that a truncation based on POMs are more sophisticated and "smarter" than simply using a selection of eigenvectors.

As mentioned in 2.3.3, a problem related to using POMs is that it relies on measurement histories. This problem becomes much more accentuated for nonlinear system, since the measurement histories now must reflect results
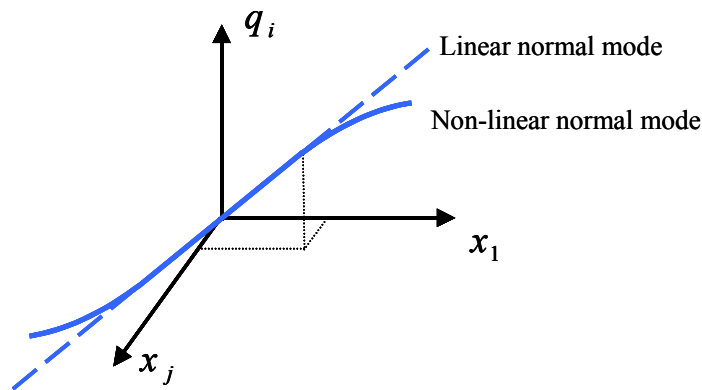
Figure 3.2: The figure shows the linear deflection path of a linear normal mode (broken line) and the nonlinear deflection path of a nonlinear normal mode [12].

from a much wider space of external influences.

3.4 Manifolds

As an alternative to using the linear normal modes as the reduced basis, we may use a procedure where both nonlinearities and, indirectly, a wider modal space are included from the outset, resulting in the creation of nonlinear, reduced-order models [1]. This is done by focusing on the inherent nonlinear behaviour from the outset of the analysis, using nonlinear normal mode (NNM) theory [12]. In the following, a theoretical background is presented.

3.4.1 Normal modes

Vakakis extended the definition of normal modes of classical vibration theory to the nonlinear case [46]. He defined a nonlinear normal mode (NNM) in an undamped, discrete or continuous system as a synchronous, periodic oscillation where all material points of the system simultaneously reach their extreme values or pass through zero. Clearly, when a discrete system vibrates in an NNM, the corresponding oscillation can be represented in the configuration space as a modal line (deflection path), as indicated in fig. 3.2. As can be seen from the same figure, linear systems possess linear modal lines, while nonlinear systems generally have nonlinear modal lines. Comments on differences between nonlinear normal modes and POMs can be found in [26].

3.4.2 Invariant manifolds

In linear dynamical systems, there is a clear relation between the linear normal modes and the dynamic behaviour. If a single linear normal mode is excited, all other modes will always be zero. The motion is therefore always on the phase plane of the single linear mode, where the phase plane is defined by
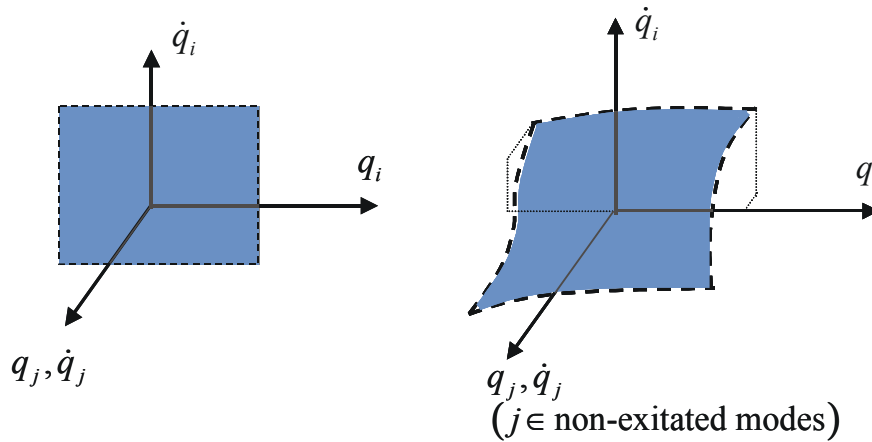
32

Figure 3.3: Left side depicts a manifold of linear dynamical system, while right side shows how a manifold of a nonlinear dynamical system may appear.

the eigenvector corresponding to the single linear normal mode and the time-derivative of the same mode. This is examplified on the left side of fig. 3.3, where the surface of the phase-plane is shown. Such a surface can generally be called an invariant manifold, since a motion initially on that surface is confined to the same surface.

For nonlinear dynamical systems the concept of linear normal modes was extended to nonlinear normal modes. A parallel extension can be done regarding the invariant manifold (or surface) in which the motion takes place. The invariant manifold will for nonlinear dynamical systems no longer be generally planar, but curved, see fig. 3.3. Hence any motion initially lying on the curved manifold will always stay on the manifold.

Provided that there exists an invariant manifold, this manifold can be used to create the reduced nonlinear model. In principle, this is done in the same manner as selecting an eigenvector as basis vector for reducing the linear model. A main difference to point out is that, due to the inherent nonlinearities, the NNMs and the manifolds do not obey the superpositioning principle. Hence two different manifolds based on two different NNMs cannot be added to construct a multi-mode manifold. A multi-mode manifold must be generated directly from the full nonlinear model.

3.5   Conclusion

In this and the previous chapter, some methodologies for constructing reduced-order models of linear and nonlinear systems were presented. In the following chapters, we shall only pursue one of the methods, namely the use of manifolds. It is, however, important for the design engineer to have a knowledge about a variety of reduction methodologies. This is because different method-

ologies result in reduced models with different properties, and because the knowledge of how reduction takes place enhances the understanding of the system under investigation.

Chapter 4
MOR: Manifolds For Conservative Systems

In section 3.4, we presented the idea of invariant manifolds. In the following we will look more carefully at methods based on invariant manifold-theory for reduction of nonlinear systems. First, however, we briefly discuss the reasons for choosing manifold-methods and not any of the other methods.

Much of what has been seen in the literature in the field of model order reduction has been concerned with the objective of creating small systems that are rapid and accurate to simulate. This is, especially in the area of MEMS, a very important task. However, our task is not only to obtain fast and accurate models. Just as important is the transparency of the model, and to give the engineer increased insight into the behaviour of the system.

To obtain transparency, knowledge, and increased understanding of a system, it is fundamental that the system description is very compact. Systems with, say a 100 d.o.f.'s, can be rapidly simulated. However, the number of d.o.f.'s is still far too large to allow for analytical inspection. A macromodel containing very few d.o.f., perhaps in the range 1-10, is more likely to provide analytical inspection. Nonlinearities in the system complicate matters, and thus a reduced nonlinear system will probably need fewer retained d.o.f. than a linear system to allow for more or less the same level of understanding and transparency.

In the previous chapters, a few methods for creating reduced-order models for both linear and nonlinear systems have been outlined. Especially for nonlinear systems, many reduction methods appear to be related to the projection framework (see section 2.3), where a main task is to choose a reduction basis. The reduction basis may then typically be based on the Krylov subspace or linear eigenvectors. We have earlier described how the nonlinearities can e.g. be included either via piecewise linearization or via manifold-methods.

It appears that it is rather difficult to gain a physical understanding of the system from basis vectors found via the Krylov subspace. A main exception is the first basis vector in the Krylov subspace, which basically is the state of the system under static load. Another drawback is that for lightly damped systems, a large Krylov subspace (many retained d.o.f.) must be used. The reason is that a close-to conservative linear system has large changes in the transfer-functions (e.g. the peaks), requiring a large number of moments to obtain a decent approximation of the transfer-function. While e.g. frequency-shift methods can be applied to alleviate the problems, the Krylov-method is inherently a moment-matching method and will remain with these drawbacks

[47].

Piecewise linearization appears to obscure the model from analytical investigation. Therefore it is a goal to use smooth functions instead of piecewise linearization in the reduced model.

For linear systems, eigenvectors can be used as the reduced basis, instead of using Krylov subspace. Using eigenvectors will give a transfer-function that is correct at the respective eigenvalues, but inaccurate elsewhere. However, eigenvectors and eigenvalues not only contain much information, but this information is also very easily accessible and provides a reasonable physical understanding of the system.

For nonlinear systems, the use of nonlinear normal modes and manifolds can be viewed as an extension of the use of eigenvectors for linear systems. The same information is, more or less, also available for this case. The nonlinearities obviously complicate the physical understanding of the system, but this can hardly be changed, since nonlinearities are the nature of the system under investigation. Thus we choose to use invariant manifolds as the basis for reduction, since this method appears to be rather transparent and intuitive.

4.1 Methodologies

In the previous chapter we presented the concept of invariant manifold theory. However, we have so far omitted discussing how invariant manifolds can be found. Three methods will be presented in the following.

4.1.1 Taylor-expansion (Asymptotic approach)

Shaw and Pierre [13] first applied center manifold theory (CMT) to nonlinear modal analysis. A number of details and examples can be found in [48]. Later, Pesheck and Pierre [1] developed a rigorous methodology for reducing a large, nonlinear system of equations to a more manageable subset, where the subset is an invariant manifold. This method is strictly valid only for conservative systems. For weakly damped systems, it has been suggested that this may be added afterwards, although this violates the invariance principle [1]. Here follows a brief outline of the formulation.

Consider a dynamical system of N degrees of freedom, expressed in the following form:

$$[M][\ddot{x}] + [K][x] + f_{nl}([x]) = 0 \qquad (4.1)$$

where $[M]$ is a mass matrix, $[K]$ is the linear stiffness matrix, and f_{nl} represents the nonlinearities of the stiffness. We assume that the nonlinearities can be expressed by means of quadratic and cubic terms. Using linear modal coordinates $[q]$, we may rewrite eq. 4.1 as

$$[I][\ddot{q}] + [\kappa][q] + [\alpha][q^{2*}] + [\beta][q^{3*}] = 0 \qquad (4.2)$$

where $[I]$ is the identity matrix, $[\kappa]$ is the new stiffness matrix, and $[\alpha]$ and $[\beta]$ are the second- and third-order stiffness matrices, respectively, and $[q^{2*}]$ and $[q^{3*}]$ contain all second and third order combinations of the modal coordinates, respectively. Eq. 4.2 may be recast into the following general form:

$$\begin{cases} \dot{q} = p \\ \dot{p} = f(p, q) \end{cases} \tag{4.3}$$

where $q = \begin{bmatrix} q_1 & q_2 & \dots & q_N \end{bmatrix}^T$ and $p = \begin{bmatrix} p_1 & p_2 & \dots & p_N \end{bmatrix}^T$ represent the generalized positions and velocities, while $f = \begin{bmatrix} f_1 & f_2 & \dots & f_N \end{bmatrix}^T$ represents the position and velocity dependent forces. Since we are searching for a multi-mode manifold corresponding to a subset S_M of modes, we may express the coordinates as:

$$\begin{cases} q_k = u_k \\ p_k = v_k \end{cases} \quad \text{for } k \in S_M \tag{4.4a}$$

$$\begin{cases} q_j = X_j(u, v) \\ p_j = Y_j(u, v) \end{cases} \quad \text{for } j \notin S_M \tag{4.4b}$$

The work of finding the functions X_j and Y_j has been the subject of several papers [49], [13], but we follow the line of [1]. Substituting this into the governing equations (eq. 4.3), we obtain a set of equations with no readily available solutions:

$$\begin{cases} \sum_{k \in S_M} \left(\frac{dX_j}{du_k} v_k + \frac{dX_j}{dv_k} f_k \right) = Y_j \\ \sum_{k \in S_M} \left(\frac{dY_j}{du_k} v_k + \frac{dY_j}{dv_k} f_k \right) = f_j \end{cases} \quad \text{for } j \notin S_M \tag{4.5}$$

However, we write an approximate solution for the coordinates X_j and Y_j ($j \notin S_M$) in the form of a polynomial expansion in the coordinates u_k and v_k ($k \in S_M$) as follows:

$$X_j = \begin{bmatrix} \sum_{k \in S_M} a_{1,j}^k u_k + a_{2,j}^k v_k \\ + \sum_{k \in S_M} \sum_{l \in S_M} a_{3,j}^{k,l} u_k u_l + a_{4,j}^{k,l} u_k v_l + a_{5,j}^{k,l} v_k v_l \\ + \sum_{k \in S_M} \sum_{l \in S_M} \sum_{q \in S_M} \begin{pmatrix} a_{6,j}^{k,l,q} u_k u_l u_q + a_{7,j}^{k,l,q} u_k u_l v_q \\ + a_{8,j}^{k,l,q} u_k v_l v_q + a_{9,j}^{k,l,q} v_k v_l v_q \end{pmatrix} \end{bmatrix} \tag{4.6a}$$

$$Y_j = \begin{bmatrix} \sum_{k \in S_M} b_{1,j}^k u_k + b_{2,j}^k v_k \\ + \sum_{k \in S_M} \sum_{l \in S_M} b_{3,j}^{k,l} u_k u_l + b_{4,j}^{k,l} u_k v_l + b_{5,j}^{k,l} v_k v_l \\ + \sum_{k \in S_M} \sum_{l \in S_M} \sum_{q \in S_M} \begin{pmatrix} b_{6,j}^{k,l,q} u_k u_l u_q + b_{7,j}^{k,l,q} u_k u_l v_q \\ + b_{8,j}^{k,l,q} u_k v_l v_q + b_{9,j}^{k,l,q} v_k v_l v_q \end{pmatrix} \end{bmatrix} \tag{4.6b}$$

Inserting this into eq. 4.5, we obtain the coefficients (a's and b's) in 4.6.

37

Although not explicitly stated here, the solution may be given in an analytical form [1]. Generally, these coefficients can be expressed through the following coupled equations:

$$D(\omega)a^{xx} = h_1(\alpha) \tag{4.7a}$$
$$E(\omega)a^{xxx} = h_2(\alpha, \beta, a^{xx}) \tag{4.7b}$$

where the matrices D and E are known functions of the linear eigenfrequencies, the vectors a^{xx} and a^{xxx} represent the coefficients in 4.6. a^{xx} is obtained from the first of these equations where h_1 is a known function of the second order stiffness matrix. Using this result, a^{xxx} is obtained from the second equation where h_2 is a function of a^{xx} and the second and third order stiffness matrices. ω are the linear eigenfrequencies of the retained modes.

Using the solution for the dependent coordinates X_j and Y_j ($j \notin S_M$) in the nonlinear terms of 4.2, we obtain a manageable formulation of the reduced-order, nonlinear problem expressed in terms of the coordinates for the modes belonging to S_M.

4.1.2 Galerkin-based method

An alternative to using asymptotic methods is to use Galerkin-methods. One example of this can be found in [50]. The same procedure is used to establish the fundamental equations describing the manifolds. However, these equations are not solved by asymptotical methods, but by means of a nonlinear Galerkin method. In brief, Galerkin-methods give an approximate solution that is valid over a pre-defined range. This is done numerically. Compared to the asymptotic approach, the Galerkin-methods have the obvious advantage of having a predefined range in which the solution is valid. This also means that the Galerkin-methods allow for a larger range of validity, and a better control of accuracy. These obvious advantages have been demonstrated in the context of invariant manifolds in [50]. We will not present any details regarding nonlinear Galerkin-methods here, but rather refer to texts like [50] and [51].

In the paper [50], they also utilizes a different coordinate system than what we have used earlier. Instead of using displacement and velocity to describe the system, the state is described by amplitude, a, and phase, ϕ:

$$u_k = a \cos \phi$$
$$v_k = \dot{u}_k = -a\omega_k \sin \phi$$

This makes it simpler to describe the range covered by the reduced model. Instead of dealing with $v_{\max}$, $v_{\min}$, $u_{\max}$, and $u_{\min}$, only the maximum amplitude is needed to limit the range of validity.

4.1.3 Methods using periodic constraint

The majority of the approaches today uses various asymptotic methods or nonlinear Galerkin methods. Some work has, however, also been focused on using periodicity constraints, [52]. There, a purely numerical method is developed, of which the principle can be briefly explained: Given that one (nonlinear) mode is excited, a simulation in time shall return to the same point after one period. The same simulation performed backwards in time, starting at the initial state, shall trace the exact same trajectory (but clearly in opposite direction). Now, assuming that the initial excitation is only approximately on the manifold, the two simulations will not trace the same trajectory. Thus the initial conditions are changed iteratively until the two trajectories are the same. At that stage the nonlinear normal mode is found for that amplitude. Further simulations can then be done at various amplitudes.

4.2 External forcing

External forcing, which clearly is of importance, has not been included in the discussion so far. A few papers have investigated systems with periodic forcing, where the forcing-effect has been included in the determination of the manifolds. In [1], using the automated method based on the asymptotic approach, external forcing was included in the model by adding it as an extra degree of freedom. A limitiation of this method is that the forcing must be described by a second order differential equation. Another possibility is to simply add the forcing to the reduced model after the reduction of the (unforced) model has taken place.

The latter method is very simple, but a main drawback is that it violates the invariance property of the manifold [1]. Here, we will demonstrate this by a very simple geometric analysis. The geometric analysis provides an increased understanding of the manifold. This in turn opens up for new methods for handling forcing.

The geometric analysis is as follows: for simplicity, assume that the forcing is constant in direction and only has a component in one of the eigenvectors. This eigenvector happens to be the vector the reduced model is based on. In other words, for small amplitudes, we can regard the system as linear, and the motion of the system should stay on the phase-plane of that mode. Furthermore, we note that the forcing vector is parallel to the linear eigenvector, and hence also parallel to the phase-plane of the chosen mode. Hence no other modes are exitated. For large amplitudes, however, the manifold deviates from the phase-plane of the linear eigenmode. The forcing (F), on the other hand, continues to be parallel to the phase plane of the linear eigenmode, see fig. 4.1 (For simplicity, we have plotted the manifold as a line, without dependence on velocity). From this we see that there is a component of the forcing that can be projected onto the manifold, and one part that is normal to
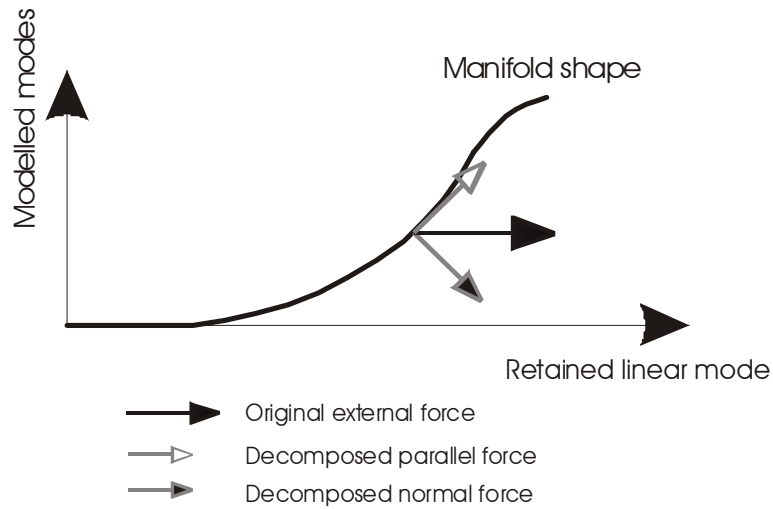
Figure 4.1: The external forcing is defined in the full space. The reduced model is, however, only capable of interacting with the parallel component of the force (F). Thus the normal component must be disregarded. (For simplicity, velocities have been assumed constant in the figure)

the manifold. The interpretation of these two components is of importance. Firstly, we assume that the system is fully modelled, but the motion happens to be on the reduced manifold (and should therefore always stay on it as long as the system is not under external influence, e.g. forcing). Now, we look at the force component parallel to the manifold. Since the forcing is parallel to the manifold, the state will change, but in a manner that still keeps the state on the manifold. This can be seen by comparing with the linear case, where a force parallel to the phase-plane of a mode, influences only that mode and no other mode.

Next step, still looking at the full system, is to analyze the force component normal to the manifold. The motion still lies on the manifold, but is now under influence of this force component. Now, since the force component is normal to the manifold, the energy (from the forcing) cannot be absorbed by the manifold. However, since the motion is not confined to the manifold (in the full system), other degrees of freedom can be excited to absorb the energy. Thus it is clear that this force-component excitates some degrees of freedom in a manner that is incompatible with the invariance property of the manifold.

So far, we have disregarded the dynamics of the system. This can be done in a simple manner, following the same general idea. For the simplified quasi-static example in fig. 4.1 we decomposed the force to one parallel and one normal component along the line. For the dynamic case, however, we must decompose the force to one component normal to, and one parallel to the invariant manifold.

If we now revisit the reduced model and we apply the forcing directly, it is clear that we actually enforce the reduced model to accept all energy-transfer resulting from the external forcing. From the arguments given above, this must be wrong, since only parts of this energy should be transfered to the manifold.

4.2.0.1   Error in external forcing and damping

The line of arguments presented above, naturally leads us to propose a better method of approximating external forcing for the reduced model. Instead of using the forcing directly, it is conceptually much more correct to project the forcing onto the manifold. A further advantage of the concept, related to error-estimates, will be explained below.

The force component normal to the manifold violates the invariance property. Hence this component can actually be used as a measure of the error in the reduced model. The larger the normal component is, the more effort is put into driving the system away from the manifold. We also note that small deviations in the state away from the manifold will influence little the behaviour. It may be quite useful not only to find the size of the normal component of the force, but also to do a coarse approximation of the displacement that this force causes. This can be done in a rather straightforward way, where the starting point is the normal component of the force. Secondly, it is assumed the system is only weakly nonlinear, in which case the linear eigenmodes can be viewed as a very rough estimate of the nonlinear normal modes in the nonlinear system. In a rather crude approximation, we therefore decompose the normal component of the force onto the linear eigenmodes and ignore the amplitude for the retained modes (of the reduced system). Following this approximation, the effect the normal component of the force has on the full linearized system is analyzed. It is important to note that this analysis only gives an indication of the size of the amplitude deviation from the manifold. However, knowing the magnitude of this amplitude, it is possible to judge whether it is acceptable to ignore it or not.

In the case where the amplitude-deviation due to forcing is too large to be acceptable, we have in fact obtained information about which modes are most important and which should be included when rebuilding a reduced model. This is clearly very useful.

So far, only external forcing has been investigated. We recall that the asymptotic approach presented earlier was not capable of dealing with damped systems. In this context it is quite possible to treat the damping forces and the external forcing in the same way. Hence it is actually possible to start with the undamped system, build a reduced model based on the asymptotic approach, investigate the effect of the damping, and then include more modes in the reduced model. This approach can clearly be used iteratively, until

satisfactory behaviour is established. In this case, with a damped, unforced system, the exact manifold is not found, but the reduced model will contain the manifold. Hence it appears that the reduced model is not reduced fully in accordance with the invariant manifold theory, but will be slightly larger than the invariant manifold.

4.3 Further considerations on invariant manifolds

Above, we have presented conciderations and concepts concerning invariant manifolds. However, a number of details regarding manifold theory and methods have been ignored. We will briefly present some of them here.

4.3.1 The asymptotic approach

The asymptotic approach method presented above assumes that the description is in the polynomial form of eq. 4.2. These coefficients must, for most systems, be obtained numerically. This can be done in a systematic manner, see [53]. Due to the high number of coefficients, this is also very time-consuming for large systems.

The asymptotic method relies upon an asymptotic approach, and will therefore have a limited range of validity. This range is not known a priori, as opposed to what is true for the nonlinear Galerkin approach. However, the range of validity is not only limited by the asymptotic approach. The full model is adapted to a polynomial form, and hence will also be valid only up to a given amplitude. Consequently, the range of validity of the reduced model relies upon the accuracy of the asymptotic approach and the accuracy of the full model. Clearly, the polynomial form also limits the form of the nonlinearities in the full system.

Another strong limitation is that the method is only strictly valid for conservative systems. However, in practice, it can be used for weakly damped systems as well [1]. Further improvements can be made by using the method presented here for determining errors due to external forcing/damping forces.

4.3.2 Internal resonance

The nonlinear normal mode is in general amplitude dependent. This implies that the resonance frequencies are state-dependent. If certain conditions are met, commensurable modes may interact strongly, resulting in interchange of energy between those modes. Hence the response becomes multi-modal [54]. This phenomenon is known as internal resonance ([55],[56]).

The interchange of energy between the (nonlinear) modes consequently requires that two modes being in internal resonance must either both be modelled or both remain unmodelled. If one mode is modelled and the other is unmodelled, the energy interchange between the (nonlinear) modes will be missing and hence the reduced model will be erronous.

For the asymptotic approach, internal resonances appears as singularities in the matrices used to find the coefficients in the polynomial expansions [1].

4.4 Accuracy of the asymptotic approach

In 4.1, methods for generating invariant manifolds were presented. Here, we will proceed by investigating the convergence properties of the asymptotic approach, as it was presented above (4.1.1) and in [1]. To investigate the properties of the method, an example system with 6 d.o.f.'s is considered. The example system is conservative.

Based on the nonlinear system, a reduced model is created, using the asymptotic approach presented earlier (4.1.1). The reduced model is simulated, and the results are compared with simulation results from the full system. Also simulation results from the linear model is included for comparison.

4.4.1 The nonlinear system

Care has to be taken to ensure that the system is conservative. This is done by choosing the nonlinear terms in a consistent manner. Here, we have chosen to implement the nonlinearities as a special case of a nonlinear coupling, where the energy has the form:

$$E = \frac{1}{2}k\left(x_1 - x_2\right)^2 + \frac{1}{3}\alpha\left(x_1 - x_2\right)^3 + \frac{1}{4}\beta\left(x_1 - x_2\right)^4$$

The force from the nonlinear coupling can easily be derived from the energy:

$$\begin{bmatrix} F_1 \\ F_2 \end{bmatrix} = \begin{bmatrix} \frac{d}{dx_1}E \\ \frac{d}{dx_2}E \end{bmatrix}$$
$$= \begin{bmatrix} k\left(x_1 - x_2\right) + \alpha\left(x_1 - x_2\right)^2 + \beta\left(x_1 - x_2\right)^3 \\ -k\left(x_1 - x_2\right) - \alpha\left(x_1 - x_2\right)^2 - \beta\left(x_1 - x_2\right)^3 \end{bmatrix}$$

Using this nonlinear relation, it is a simple task to add a number of these nonlinear elements to the linear system, and hence obtain a nonlinear system.

The nonlinear elements of the system used, are shown as a table in fig. 4.2. As can be seen, the coupling elements have been included to ensure sufficient coupling between the various degrees of freedom. The linear elements are:

$$[K]\,[q] = \begin{bmatrix} 1{\cdot}10^5 & 0 & 0 & 0 & 0 & 0 \\ 0 & 2.5{\cdot}10^6 & 0 & 0 & 0 & 0 \\ 0 & 0 & 1.5{\cdot}10^5 & 0 & 0 & 0 \\ 0 & 0 & 0 & 1.2{\cdot}10^5 & 0 & 0 \\ 0 & 0 & 0 & 0 & 4.1{\cdot}10^6 & 0 \\ 0 & 0 & 0 & 0 & 0 & 2.7{\cdot}10^6 \end{bmatrix} \begin{bmatrix} q_1 \\ q_2 \\ q_3 \\ q_4 \\ q_5 \\ q_6 \end{bmatrix}$$

In the following, the accuracy of the reduction scheme is tested and discussed. This is done by varying the number of retained modes (that is, the degree

Figure 4.2: The nonlinear stiffness of the system.

of freedom in the reduced model) and the amplitude at which the system oscillates.

4.4.2 One-mode selection

In the first test case, we generate the manifold with a single mode retained. We choose mode 1 as the retained mode, and it is thus the mode of origin of the manifold. It is the mode with lowest eigenfrequency, and this makes it a sensible choice in terms of trying to model as much as possible of the energy in the system. This of course depend on the form of the system-excitation, but generally, it is a sensible choice.

As already mentioned, three types of simulations are done, namely of the full system (FNI), the linear system (FL), and the reduced manifold system (TNI).

The initial conditions of the system are obviously important. To make sure that the starting points are equivalent in all the simulations, they are calculated from the invariant manifold. This means that we first set mode 1 (the retained mode) to the assigned amplitude. Next, we calculate the amplitude and velocity of the slave modes, as given from the equations describing the manifold (eq. 4.6). Thus we have the initial values for the full system simulations.

In figs. 4.3 and 4.4, the shape of the approximate manifold is presented, demonstrating the geometric nature of the manifold methodology. The initial values for the full system simulations can also be interpreted geometrically. Looking at the figs. 4.3 and 4.4, the amplitude of mode 2 and mode 3 can be found as function of amplitude and velocity of mode 1 (the retained mode). Similar figures can also be made relating velocities and amplitudes of the other modes to the retained mode.

In the same figures (figs. 4.3 and 4.4), simulation results are also included, the green line are results of the full simulations, while the red line stems from the simulations of the reduced model. Clearly, the red lines are bound to follow the shape of the manifold. The green lines, however, may be said to represents the exact solution, since they are based on the full system simulations.

The deviations between the simulation results are likely to be due to errors in the manifold resulting from the approximative nature of the asymptotic approach. Two main types of errors are present, and will be explained in the below.

First comes the error related to the initial conditions of the full system (or shape of the manifold). According to the geometrical interpretation of the manifold, we note that the amplitudes and velocities of the slave modes are functions of the retained mode (see figs. 4.3 and 4.4). Hence, once the amplitude of the retained mode is chosen, we can calculate the amplitude of the slave modes from the invariant manifold. We may now perform simulations

on the full system, and we note that the result should be equivalent to that of the reduced model. However, if the invariant manifold is inaccurate, then also the initial amplitudes of the slave modes will be inaccurately calculated. Now, performing a simulation on the reduced system, the motion is bound to follow the (inaccurate) manifold. Using the same initial conditions to perform simulations on the full system, the result will show that the motion is different from the inaccurate manifold.

A comparison with a linear system can be given. Looking at the linear system, we remember that a motion existing on the phase-plane of one mode only will always stay on that phase-plane (3.4). Now we assume that we have calculated the eigenvector inaccurately (which for a linear system means the same as identifying the phase-plane, or manifold, inaccurately). Secondly, we say that the initial conditions should be so that only a single mode is exitated. This means that the initial conditions are proportional to an eigenvector. However, since the eigenvector is inaccurate, we are actually exitating other modes as well, and the motion will clearly not stay on the calculated phase-plane of the intially chosen mode.

The second type of error relates to the energy of the system when being on the manifold, but not to the geometric shape of the manifold. This can be examplified by looking at the system:

$$\begin{bmatrix} \ddot{q}_1 \\ \ddot{q}_2 \end{bmatrix} = \begin{bmatrix} -\omega_1^2 & 0 \\ 0 & -\omega_1^2 \end{bmatrix} \begin{bmatrix} q_1 \\ q_2 \end{bmatrix} + \begin{bmatrix} -a \cdot q_1^2 \\ 0 \end{bmatrix}$$

Whilst the system is clearly nonlinear, it is evident that nonlinear normal modes at all time are parallel to respectively q_1 and q_2. Also, it can be seen that the mode 1 manifold is planar (Mode 1 is the retained mode. The motion will always stay on the phase-plane of mode 1. The amplitude of mode 2 is always zero). This means that the reduced model based on the manifold is:

$$\begin{align} \ddot{q}_1 &= -\omega_1^2 \cdot q_1 - a \cdot q_1^2 & \text{(4.8a)} \\ q_2 &= f(q_1) = 0 & \text{(4.8b)} \end{align}$$

At the same time, we see that the equation:

$$\begin{align} \ddot{q}_1 &= -\omega_1^2 \cdot q_1 & \text{(4.9a)} \\ q_2 &= f(q_1) = 0 & \text{(4.9b)} \end{align}$$

exhibits the same motion with respect to the slave mode (mode 2). Hence, the geometric shape of the manifold is described correctly in both equations (eq. 4.8b, 4.9b), although the latter system describes the dynamics of the motion on the manifold erronously (eq. 4.9a). In other words, the energy of the system being on the manifold is described incorrectly.

In principal, these two types of errors can be seen by investigating plots of the results. The first type of error, regarding the geometric shape of the

manifold, can potentially be seen in plots like those in figs. 4.3, 4.4, and 4.8. In fig. 4.4, we see that there is a distinct difference between the full system results and the manifold shape regarding mode 3, a slave mode for the largest initial amplitude. Thus it may be concluded that the initial values for the full system simulations where not on the exact manifold, or, in other words, the calculated manifold shape does not match the exact manifold shape accurately.

Assuming that the calculated manifold shape matches the exact manifold shape nicely, one may identify the second type of error (regarding the dynamics on the manifold) by investigating plots. This may most easily be done by looking at phase-plots of the retained mode, like fig. 4.5, where the error appears as a difference between simulation results of the full system and those of the reduced system. However, it is important to note that an error in the phase-plot of the retained mode is not necessarily an error of the second type. Both types of errors give phase-plots where the full system and reduced system results differ, and this is true for phase-plots for both the retained mode(s) and the slave modes.

For the one-mode selection considered in this section, one may draw some conclusions. By looking at the phase-plot in fig. 4.5, we note that the reduced system gives quite accurate results for mode 1 (the retained mode). Hence, we may compare results of the slave modes by investigating phase-plots. In figs. 4.6, 4.7, and 4.8, we note that the results starts to differ at the higher level of initial amplitude. At the same time, the retained mode is approximated quite well. The conclusion must therefore be that for the slave modes 2 and 3 (ref. figs. 4.6, 4.7, and 4.8), the manifold shape starts to diverge, but that the modes are relatively insignificant for the dynamics of the reduced model. Two other slave modes, modes 5 and 6, though, appears to give quite accurate results when looking at the phase-plots (figs. 4.9, 4.10). Because the dynamics of the retained mode is modelled quite accurately, we therefore conclude that modes 5 and 6 are of higher importance to the nonlinear behaviour of the reduced system, than are modes 2 and 3.

4.4.3 Two-mode selection

In this section, a reduced model is created based on two retained modes, namely mode 1 and mode 4. These are selected since they have the lowest resonance frequencies. Using more than one mode as basis for the manifold means that a geometric visualization of the manifold shapes (like in fig. 4.3) becomes impossible. The phase-plots, however, can still be used to investigate errors.

4.4.3.1 Comparison with one-mode selection

In the above simulations, it was noted that the response of the reduced system was not completely in accordance with that of the full system for larger initial
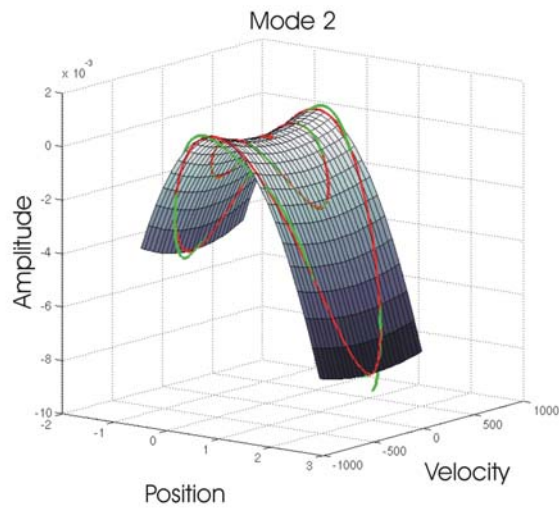
Figure 4.3: The single-mode manifold is shown, where mode 2 is shown as a function of retained mode 1 (the surface). Simulations of the full system are shown (green lines). Simulations using the manifold are also shown (red lines). Simulations are done at different initial amplitudes.
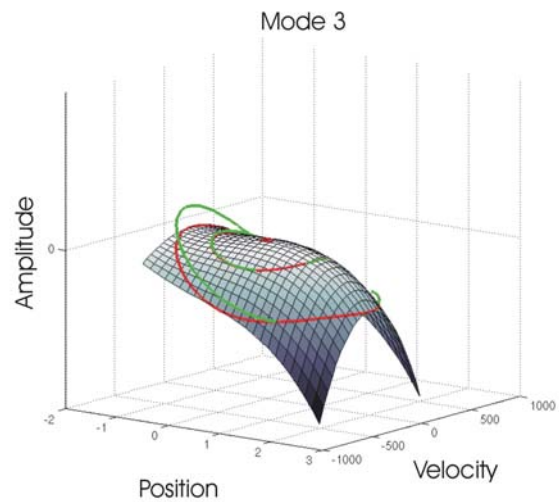

Figure 4.4: The single-mode manifold is shown, where mode 3 is shown as a function of retained mode 1 (the surface). Simulations of the full system are shown (green lines). Simulations using the manifold are also shown (red lines). Simulations are done at different initial amplitudes.
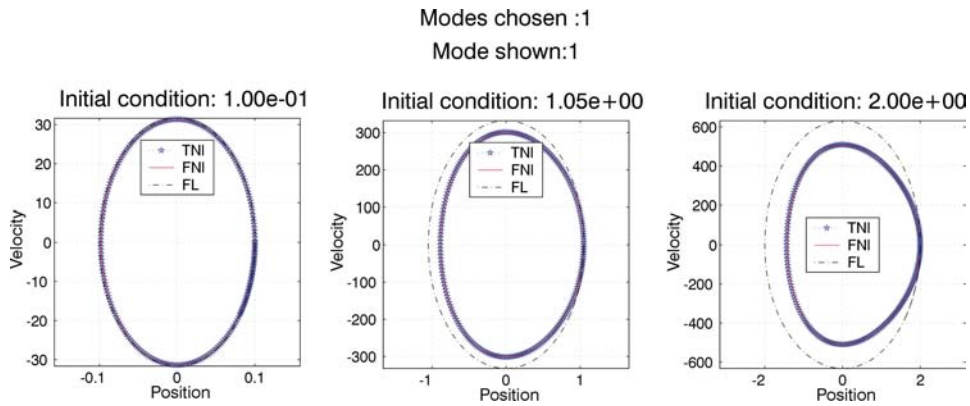
Figure 4.5: The trajectory of mode 1 is shown for simulations using the full system (FNI), the reduced model (TNI) and the full linear model (FL). The reduced model is created using a single-mode manifold, based on mode 1. Each plot in the figure refers to a different level of inital values.
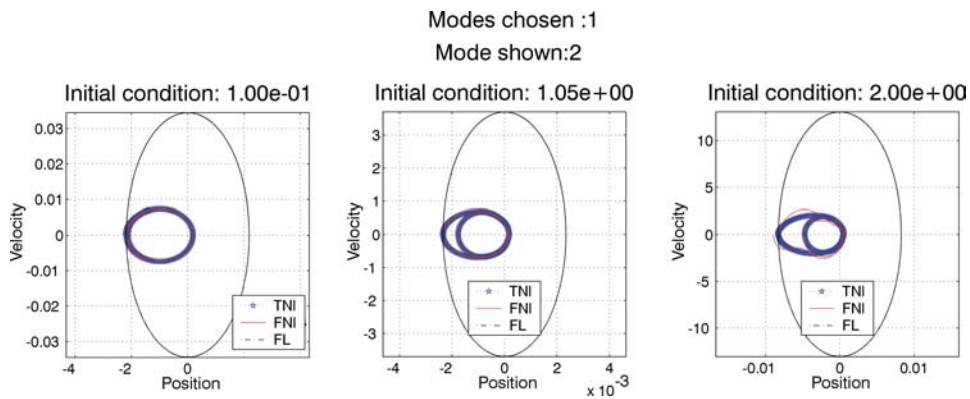

Figure 4.6: The trajectory of mode 2 is shown for simulations using the full system (FNI), the reduced model (TNI) and the full linear model (FL). The reduced model is created using a single-mode manifold, based on mode 1. Each plot in the figure refers to a different level of inital values.
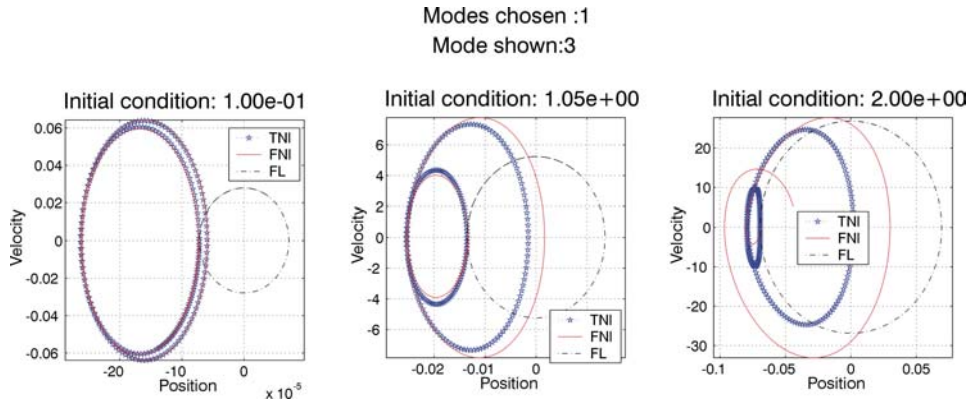
49

Figure 4.7: The trajectory of mode 3 is shown for simulations using the full system (FNI), the reduced model (TNI) and the full linear model (FL). The reduced model is created using a single-mode manifold, based on mode 1. Each plot in the figure refers to a different level of inital values.
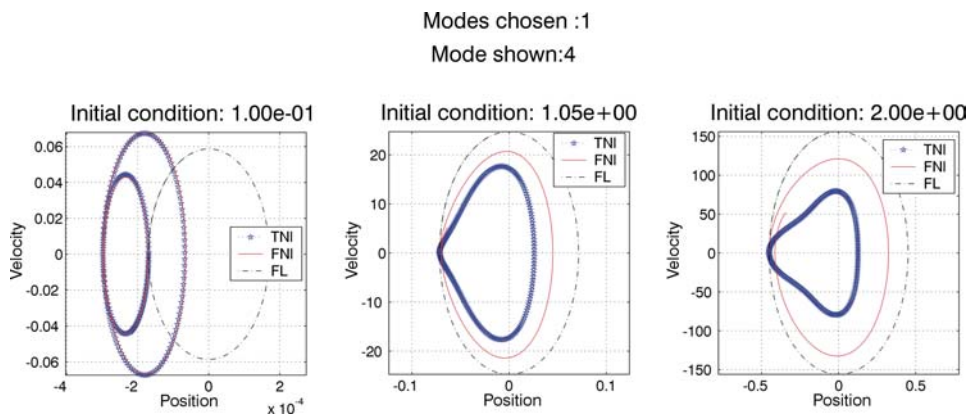

Figure 4.8: The trajectory of mode 4 is shown for simulations using the full system (FNI), the reduced model (TNI) and the full linear model (FL). The reduced model is created using a single-mode manifold, based on mode 1. Each plot in the figure refers to a different level of inital values.
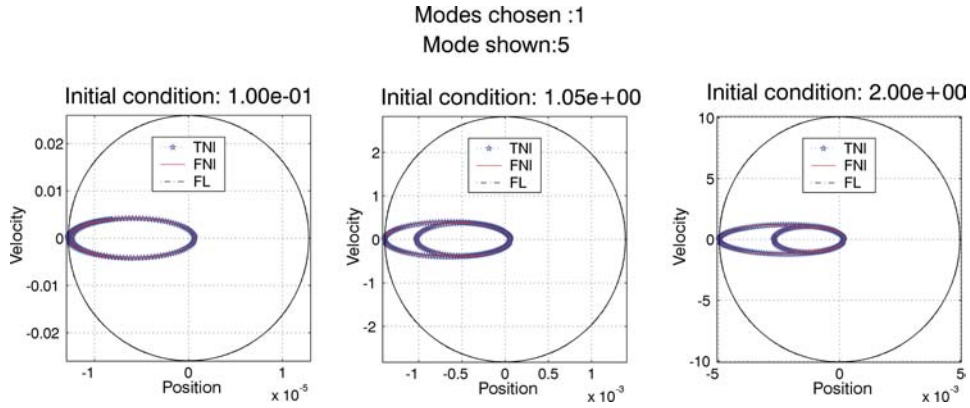
Figure 4.9: The trajectory of mode 5 is shown for simulations using the full system (FNI), the reduced model (TNI) and the full linear model (FL). The reduced model is created using a single-mode manifold, based on mode 1. Each plot in the figure refers to a different level of inital values.

Figure 4.10: The trajectory of mode 6 is shown for simulations using the full system (FNI), the reduced model (TNI) and the full linear model (FL). The reduced model is created using a single-mode manifold, based on mode 1. Each plot in the figure refers to a different level of inital values.
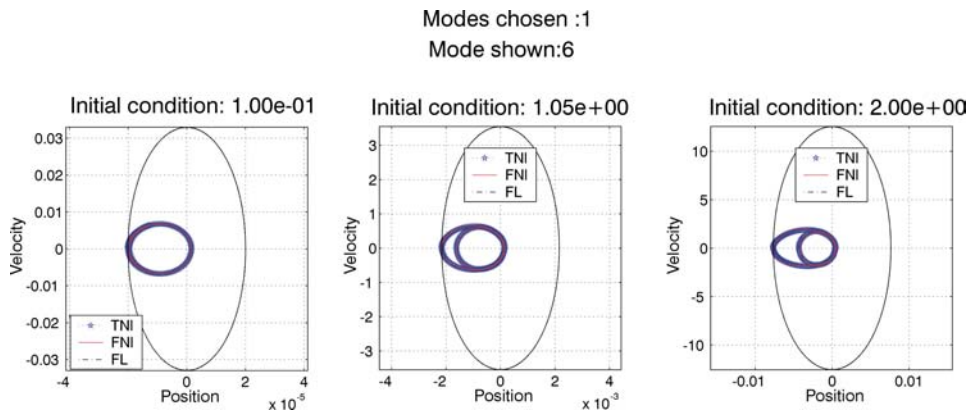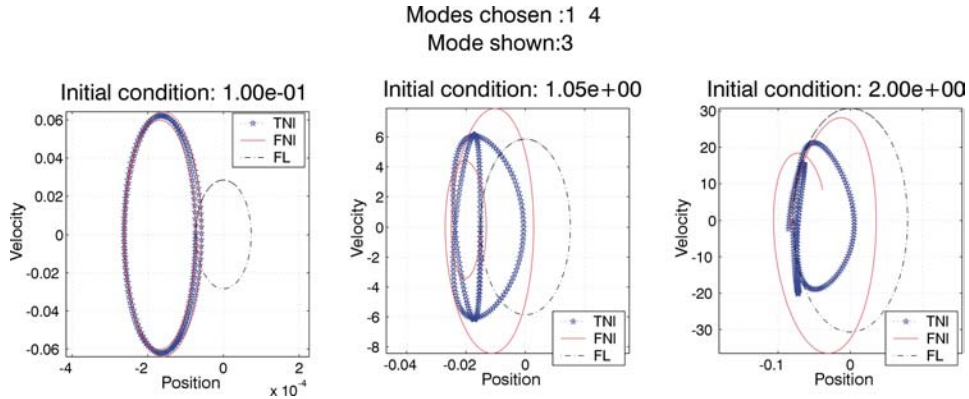
51

Figure 4.11: The trajectory of mode 3 is shown for simulations using the full system (FNI), the reduced model (TNI) and the full linear model (FL). The reduced model is created using a two-mode manifold, based on modes 1 and 4. The simulations are performed at different initial values, which are calculated based on the one-mode manifold. Simulations are based on the two-mode manifold.

values of the amplitude of the retained mode. Here, we create a manifold based on the two modes 1 and 4, to investigate what happens to the accuracy when the dimensions of the manifold increase. For the simulations, the initial values used, are the same as those for the one mode manifold. More precisely, for the manifold simulations the initial amplitudes of mode 1 and 4 are taken from the one-mode manifold approximation presented in 4.4.2. For the full simulations, these values are used in the two-mode manifold approximation to find the initial values of the slave modes. The results for mode 3 and 4 are presented in figs. 4.11 and 4.12.

From figs.4.8 and 4.12, we see that the behaviour of mode 4 is much better approximated using the two-mode manifold, compared to using only the one-mode manifold. This should be no big surprise since the two-mode manifold uses mode 4 as one of the retained modes.

The approximation of mode 3 was seen to be poor for the largest initial values for the one-mode manifold, see fig. 4.7. This approximation appears not be improved when the manifold is expanded to a two-mode manifold, see fig. 4.11. This may indicate that the inaccuracy is due to insufficient approximation of a coupling directly between mode 1 and mode 3, or at least that the coupling is not strongly dependent upon mode 4.

4.4.3.2 General initial condition

For the simulation-results presented here, the initial conditions have been such that both retained modes have the same initial value. The slave modes are calculated on basis of two retained modes in the manifold.
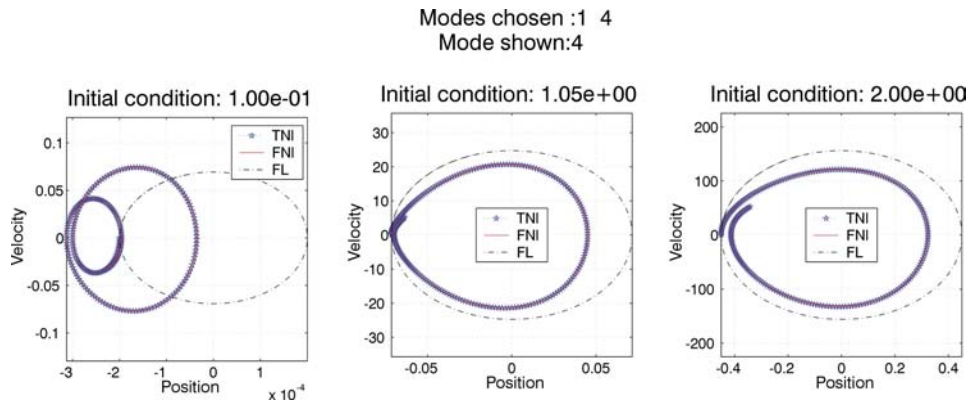
52

Figure 4.12: The trajectory of mode 4 is shown for simulations using the full system (FNI), the reduced model (TNI) and the full linear model (FL). The reduced model is created using a two-mode manifold, based on modes 1 and 4. The simulations are performed at different initial values, which are calculated based on the one-mode manifold. Simulations are based on the two-mode manifold.

Figure 4.13: The trajectory of mode 1 is shown for simulations using the full system (FNI), the reduced model (TNI) and the full linear model (FL). The reduced model is created using a two-mode manifold, based on modes 1 and 4. The simulations are performed at different initial values. Both the retained modes have the same initial value.

53
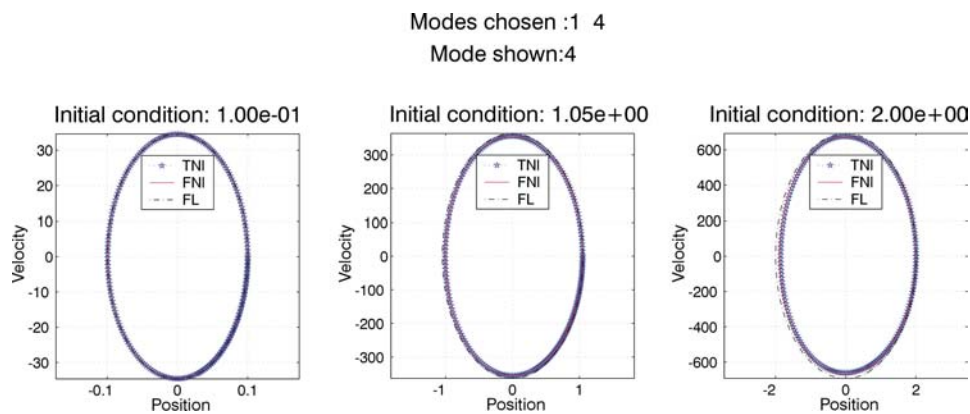
Figure 4.14: The trajectory of mode 4 is shown for simulations using the full system (FNI), the reduced model (TNI) and the full linear model (FL). The reduced model is created using a two-mode manifold, based on modes 1 and 4. The simulations are performed at different initial values. Both the retained modes have the same initial value.
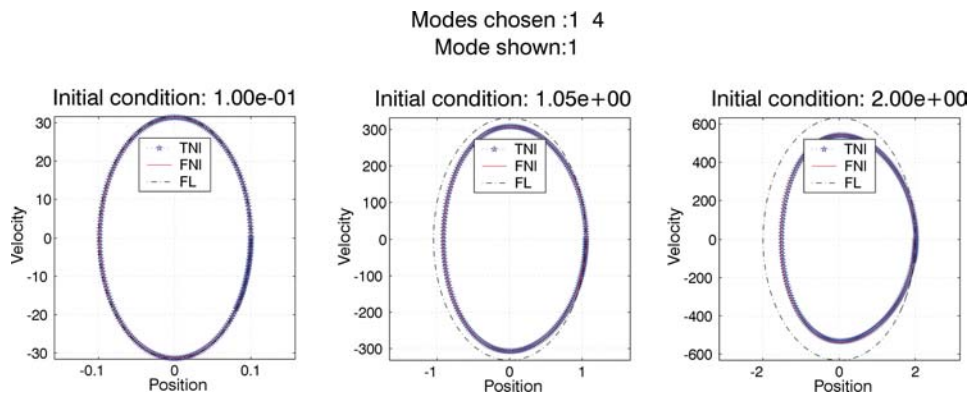

Figure 4.15: The trajectory of mode 3 is shown for simulations using the full system (FNI), the reduced model (TNI) and the full linear model (FL). The reduced model is created using a two-mode manifold, based on modes 1 and 4. The simulations are performed at different initial values. Both the retained modes have the same initial value.
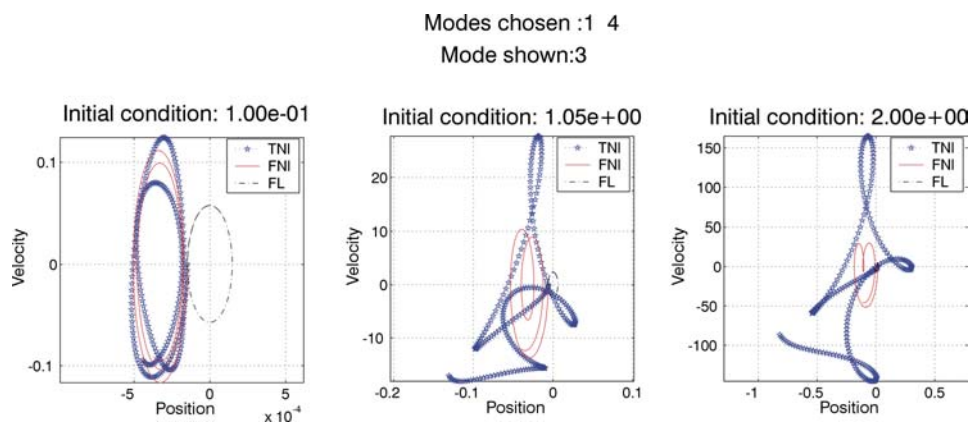
In fig. 4.13, we note the nonlinear behaviour of the retained mode 1. For the retained mode 4, we see the behaviour in fig. 4.14, which appears to be less nonlinear than mode 1. However, the reduced model simulation fits the full system simulations well for both retained modes.

In fig. 4.15, the response of mode 3, a slave mode, is shown. From the plot with lowest initial conditions, it can be seen that the mode 3 approximation is acceptable to a certain degree. However, at the larger initial conditions, the calculated manifold for mode 3 strongly diverges from the exact manifold, which can be seen by the total mismatch between the manifold-based and the full system simulations in fig. 4.15. It is interesting to note that although mode 4 appears to behave quite linearly in fig. 4.14, it has significant influence on the nonlinear behaviour of slave mode 3. This can be seen by comparing the simulation results based on the two-mode manifold, with different initial conditions, see fig. 4.15 and 4.11.

From the simulation results of the two-mode manifold, it can be seen that the approximation of mode 3 is worse when both mode 1 and mode 4 have large initial values. It can be argued that having large initial values of both mode 1 and 4 mean that one is effectively further away from the starting-point of the Taylor-expansion. This, in turn, means that the Taylor-expansion becomes less accurate when both modes are excited. At the same time, we clearly see that the manifold converges for smaller initial values, but at levels where nonlinearities still are significant.

4.4.4 Three-mode selection

This model is the largest of the reduced models presented. Here, 3 modes are retained. This implies that there are only 3 modes left to be modelled (being slaves), and which are removed from the dynamics of the reduced model. With a reduced dynamic model containing as many as 3 d.o.f.'s out of an initially 6 d.o.f.-system, one would expect a quite accurate reduced model.

For the retained modes 1, 3, and 4, it can be seen that mode 3 and 4 appears to behave much more linear than mode 1, see fig. 4.16, 4.17, and 4.18. However, for all the retained modes, the reduced model simulations compare quite nicely with the full system simulations.

In fig. 4.19, it can be seen that the response from the reduced system gives a well-defined and periodic response for mode 5 (which is a slave mode). At lower levels of initial conditions, it can be seen that the manifold matches quite nicely, but at higher levels a clear mismatch can be seen.

4.4.5 Summary and discussion of results

In the above, a 6-d.o.f. system has been simulated using a full nonlinear model and a linear model. Furthermore, reduced models based on an asymptotic approach of the invariant manifold have been constructed and simulated. These reduced models have been constructed with different number of re-

Modes chosen :1 3 4
Mode shown:1

Figure 4.16: The trajectory of mode 1 is shown for simulations using the full system (FNI), the reduced model (TNI) and the full linear model (FL). The reduced model is created using a three-mode manifold, based on modes 1, 4, and 3. The simulations are performed at different initial values. All the retained modes have the same initial value.

Modes chosen :1 3 4
Mode shown:3
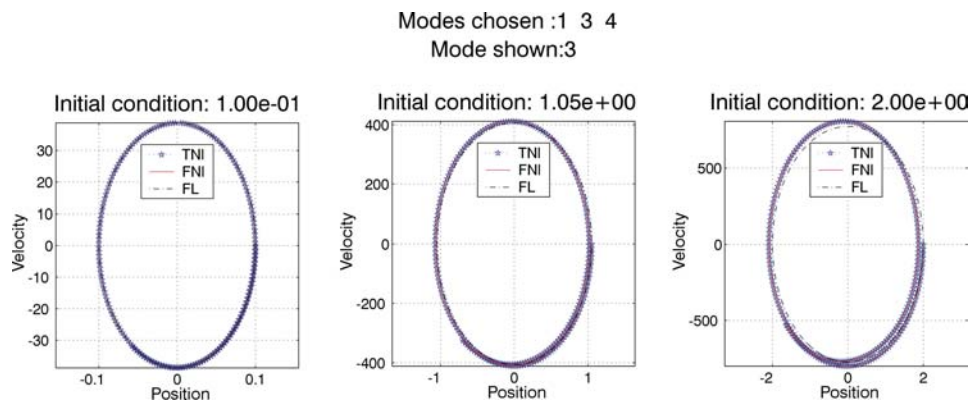
Figure 4.17: The trajectory of mode 3 is shown for simulations using the full system (FNI), the reduced model (TNI) and the full linear model (FL). The reduced model is created using a three-mode manifold, based on modes 1, 4, and 3. The simulations are performed at different initial values. All the retained modes have the same initial value.
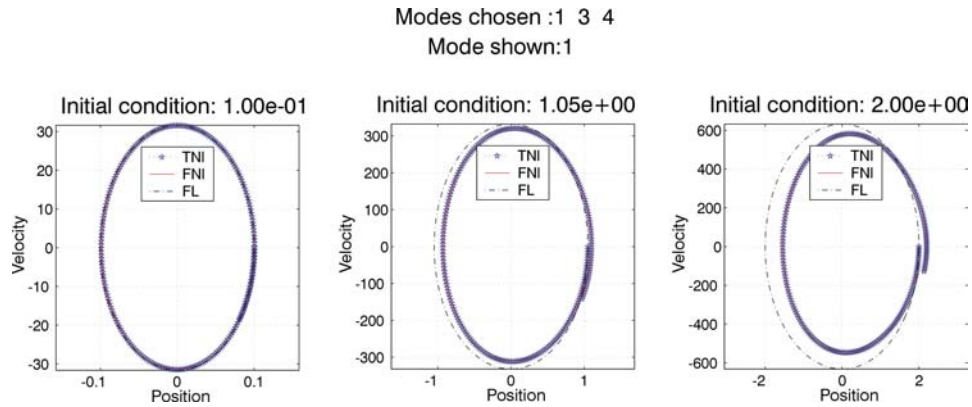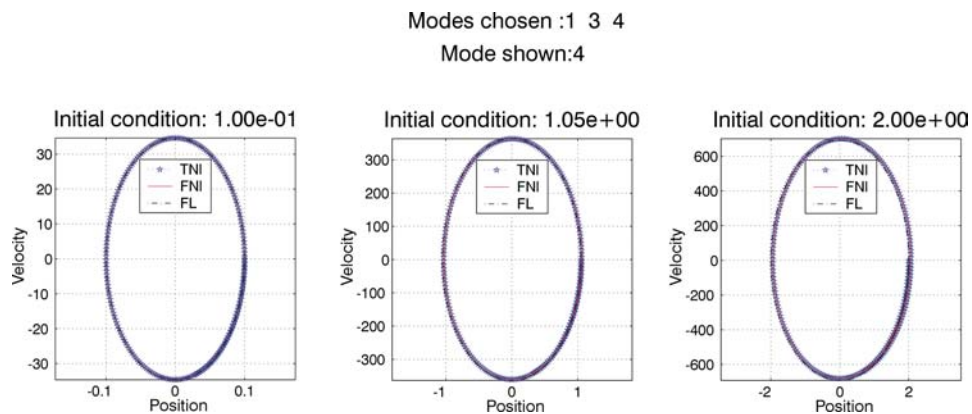
Figure 4.18: The trajectory of mode 4 is shown for simulations using the full system (FNI), the reduced model (TNI) and the full linear model (FL). The reduced model is created using a three-mode manifold, based on modes 1, 4, and 3. The simulations are performed at different initial values. All the retained modes have the same initial value.

Figure 4.19: The trajectory of mode 5 is shown for simulations using the full system (FNI), the reduced model (TNI) and the full linear model (FL). The reduced model is created using a three-mode manifold, based on modes 1, 4, and 3. The simulations are performed at different initial values. All the retained modes have the same initial value.
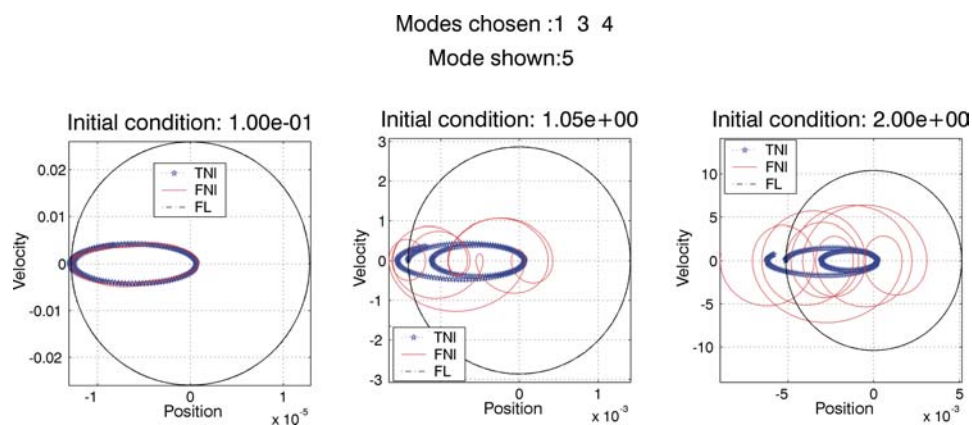
tained modes.

The accuracy of the asymptotic approach has been demonstrated, and it has been clearly shown that for large amplitudes the polynomial approximation of the manifold deviates from the true manifold. This is due to the asymptotic approach used for finding the manifold shape. It is also noted that due to the same asymptotic approach, the inaccuracy of a manifold (with several retained modes) increases when more and more of the retained modes are given large initial values. Hence the most accurate reduced model is a manifold with many retained modes, whose initial condition lie on a single-mode manifold.

The reduced model's accuracy can be defined in terms of accuracy in the dynamics of the retained mode in the reduced model, or in terms of the manifold's ability to approximate the slave modes. From the limited set of simulation presented here, the accuracy of the slave modes varies significantly from mode to mode. It appears that the slave modes being most important with respect to the nonlinear behaviour of the retained mode, are those slave modes that are best approximated. This might be a specific property of the system we have chosen. In other words, the limited set of simulations and the single system we tested prohibit us from drawing conclusion on which slave modes are best approximated in general systems.

For a physical system, the nonlinearities must be expressed in terms of poynomials. Generally, the polynomials are only approximations of the exact physics. Hence, both the accuracy of the asymptotic approach for finding the manifold and the accuracy of the polynomials in the full system present restrictions on the valid range of the manifold.

The simulations have shown that the manifold methodology based on the asymptotic approach is capable of capturing the true nonlinear behaviour of a system. Due to its geometric foundation, the method also invites for increased understanding of the nonlinear behaviour of the nonlinear system.

4.5 Example: Analytical reduced-order modelling of a dual-axis accelerometer

This section is largely based on [57], where we developed a method for generating a design-parameter sensitive invariant manifold.

4.5.1 Design-parameter sensitivity

In section 4.4, we demonstrated the use of invariant manifolds generated via the asymptotic approach. This technique has the proven ability to generate reduced models, which not only leads to faster simulations, but even more importantly, increases understanding of the nonlinear system. However, the methodology gives no information about how changes in design-parameters influence the system behaviour. Clearly, there is a great advantage in having a

model that is parameter dependent. This has lead us to develop a method that is based on the asymptotic approach for generating the manifold, which also includes design-parameter sensitivities [57].

From the general formalism of generating the invariant manifold via the asymptotic approach, as presented in 4.1.1, we now proceed to develop a parameterized model formalism suitable for predictive design. One possibility is to sample the design space of interest to obtain a suitable parameter set. However, this may require extensive simulations. Instead, we adopt a strategy based on Taylor-series expansions of the formalism presented in section 4.1.1, with respect to the design parameters.

First, our problem is normally stated in terms of the physical coordinates such as in eq. 4.1, instead of the modal coordinates as in eq. 4.2. We therefore generate an approximate formulation in the form of eq. 4.2 by a linear expansion of the eigenvectors of the original system in terms of the design parameters. Various methods exist for finding these derivatives, such as Nelson's method [58], finite-difference methods, modal methods, and modified modal methods. Computational cost and accuracy may vary between these methods [59]. For problems with repeated (degenerate) eigenvalues and their associated eigenvectors, special methods must be applied [60],[61].

Having calculated the derivatives by means of one of the above-mentioned methods, we may write:

$$\tilde{Q} = Q_0 + \left(\frac{d}{dg} Q_0 \right) \Delta g \qquad (4.10)$$

where $Q_0 = \begin{bmatrix} q_1 & q_2 & \dots & q_N \end{bmatrix}$ is the initial eigenvector matrix, $\tilde{Q}$ is the perturbed eigenvector matrix, and g is a design-parameter (typically length, width, etc). Assuming that the dependence of the stiffness matrices on the design parameters are known, we may proceed to rewrite eq. 4.2 in the following form:

$$[I] \left[\frac{d}{dt^2} \tilde{q} \right] + [\tilde{\kappa}(g)] [\tilde{q}] + [\tilde{\alpha}(g)] [\tilde{q}^{2*}] + \left[\tilde{\beta}(g) \right] [\tilde{q}^{3*}] = 0 \qquad (4.11)$$

However, we also need an approximate solution of eq. 4.7, that involves the following derivatives (see 4.1.1):

$$\frac{d}{dg} a^{xx} = D^{-1} \left(\frac{d}{dg} h_1 - \left(\frac{d}{dg} D \right) a^{xx} \right)$$

and the corresponding ones for a^{xxx}.

Hence we have constructed approximate solutions both for the stiffness matrices and for the coefficients in the polynomial expansion. Inserting the approximate solutions of the modes into eq. 4.11, we obtained a reduced, parametrized, nonlinear model of the system.
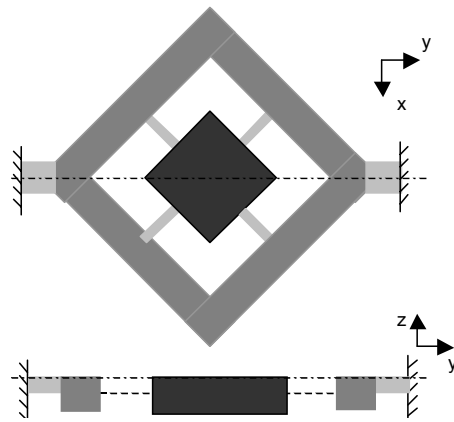
Figure 4.20: Schematic view of the dual-axis accelerometer investigated. Detection is done for x- and z-axis acceleration (Courtesy of SensoNor ASA. Patent pending EP00305807.0).

4.5.2 Simulation results

The above method was implemented in the commercial mathematical program Mathcad and tested on an industrialized dual-axis accelerometer as shown in fig. 4.20.

The accelerometer was realized in single-crystalline silicon by a bulk micromachining process. The z-axis acceleration is measured by piezoresistors implanted in the inner (light gray) beams, while the x-axis acceleration is detected by piezoresistors implanted in one of the outer (light gray) beams (torsional deformation).

A preliminary analysis indicates that there are two dominant modes in the system, the z-axis deflection of the central mass (mode 2) and the torsion of the assembly about the y-axis (mode 1). Hence, these modes are chosen as our subset S_M (i.e the retained modes). In general, the modes to be included in the subset should be selected with care.

Here we primarily investigate the validity of the design-parameter sensitive solution presented above by comparison with the "exact" reduced model, obtained using the asymptotic approach for generating the manifold. In other words, the design-parameter sensitive reduced model is compared to reduced models obtained by using the asymptotic approach for a number of different geometries. In the design-parameter sensitive reduced model, approximate results are obtained by linear expansion in terms of a given design parameter from a known starting point, while the reduced model made for comparison, the results were always calculated using the complete reduced model. The design parameter considered is the length L of the left-side outer beam.
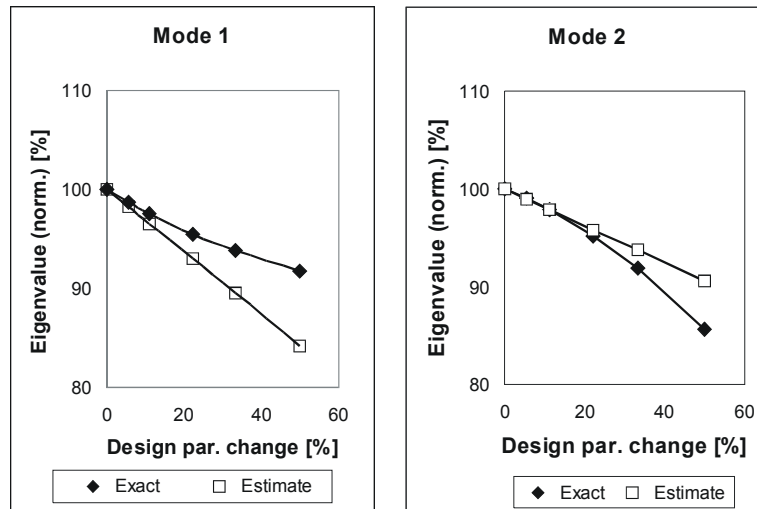
Figure 4.21: Eigenvalues of the two dominant modes versus the relative increase in the design parameter L.

In fig. 4.21 we show the change in the small-signal eigenvalues of the two dominant modes with increasing L. Although this result does not depend on the nonlinearities in the stiffness matrix, it illustrates the overall sensitivity of the system to the parameter chosen, and how well this is reproduced using the linear expansion in eq. 4.10. We notice that the linear expansion provides a good indication of the sensitivity of the eigenfunctions to the design parameter L. It reproduces the results from the complete reduced-order model quite well for up to 10–20 percent increase in L, which is well in the range of process-variations of the geometry and also quite acceptable for optimization of the geometry.

To illustrate the effects of the stiffness nonlinearties, we show in fig. 4.22 a similar comparison of the sensitivity of a dominant second order term in the stiffness matrix. We again observe, just as for the eigenvalues, that the series expansion reproduces the results from the complete reduced-order model quite well for up to 10–20 percent increase in L.

As a further illustration of the nonlinear effects, we have considered the coupling of modes 1 and 2. In fig. 4.23, we have plotted the temporal variation in the excitation of mode 1 resulting from an initial displacement of the system in mode 2. The figure shows the excitation in mode 1 calculated from the complete reduced-order model for a nominal value of the design parameter L and for an 11 percent increase in L. In addition, the latter was calculated using the parameter sensitivity procedure. Again, we observe that the sensitivity procedure provides a good representation of the excitation predicted by the complete model.

61
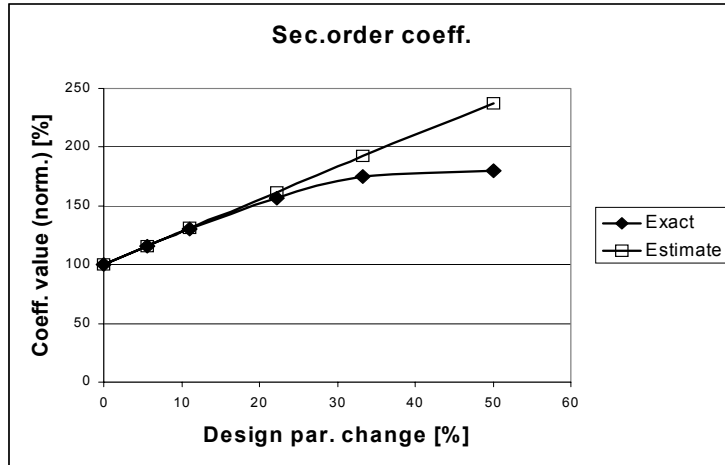
Figure 4.22: Dependence of a dominant second order stiffness coefficient on the relative change of the design parameter L, calculated with the complete reduced-order model and its linearization
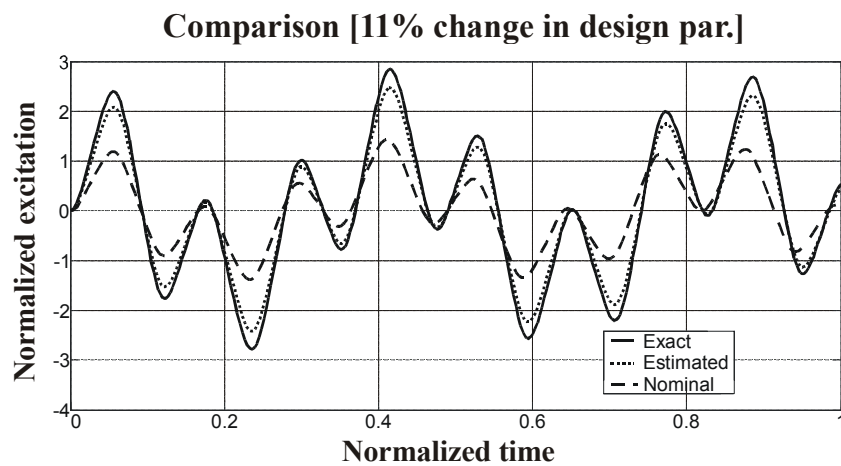
Figure 4.23: Comparison of mode excitation caused by nonlinear mode coupling, calculated with the complete reduced-order model (solid line) and its parameter-sensitive reduced model (dotted line) at 11 percent change in the design parameter L. Also shown: the excitation at the nominal value of L.

4.5.3   Discussion and summary

Here, we have shown how a reduced-order description of nonlinear, dynamical MEMS systems can be formulated analytically, allowing it to be used in predictive device design. A version of the formalism linearized with respect to design parameters is shown to be quite suitable for sensitivity analysis and design optimization.

In modelling the accelerometer, damping effects have been neglected. Hence the non-linear effects are geometrical non-linearites of the mechanics, since the material, single-crystalline silicon, is assumed to be perfectly linear.

As already mentioned, the asymptotic approach has a limited range of validity. Clearly, the same is true for the Taylor-expansion approximation of the eigenvectors and the nonlinear coefficients. Thence it follows that the parameter sensitive reduced model is not only limited in validity in terms of amplitude, but also in terms of changes in design-parameters. This does limit the applicability of the reduced model. However, we have seen that in the example above that the method is capable of handling design-parameter changes that significantly changes the system behaviour. The advantages of having a parameter-sensitive reduced model which more than indicates the non-linear effects are apparent.

4.6   Discussion and conclusion on invariant manifolds

In this chapter manifold-methods for conservative systems have been presented. We emphasized the asymptotic approach as presented by Pesheck and Pierre in [1]. We have demonstrated the accuracy of the method with respect to its ability to model large-amplitude nonlinearites. We have shown that the asymptotic approach is quite capable of handling weakly nonlinear systems. For stronger nonlinearities, other methods for finding the manifold must be used.

To the author's best knowledge, this is the first time a geometric interpretation of external forcing on the manifold has been presented. The geometric interpretation results in a more correct way of handling the forcing. At the same time, the interpretation also provides a measure of accuracy of the reduced manifold.

Also presented is a new method for generating parameter-sensitive invariant manifolds. The model is obtained by performing a Taylor-expansion of the formulation using an asymptotic approach for finding the manifold [57].

Generally, manifold-methods appear to be suitable for reducing weakly nonlinear systems. This results from the ability to maintain the correct nonlinear behaviour and from the intuitivity principle that lies behind the method. The latter is of fundamental importance for obtaining a simple model that is transparent and that gives further insight into the system behaviour.

Reduction based on manifold methods may be more difficult to realize for strongly nonlinear systems, primarily due to limitations arising from internal resonances between nonlinear normal modes.

Chapter 5
MOR: Manifolds For Dissipative Systems

In the previous chapter, we were concerned with invariant manifolds for conservative systems. To cover a broader range of systems, we will in this chapter look at dissipative systems. For linear systems, where one utilize a reduction based on a set of eigenvectors, conservative and dissipative systems may be treated equivalent. However, for nonlinear system the situation is more complex. Before looking more into manifolds for dissipative systems, we will briefly recapitulate our discussion of manifolds for conservative systems.

For conservative systems, we used the concept of an invariant manifold. This implies that the system behaviour would always stay on that manifold. However, nothing was said about periodicity of the reduced system behaviour, so as long as the manifold has at least 2 d.o.f.'s it still might be chaotic. We will not involve ourselves in a discussion of chaotic systems and their behaviour, but rather refer to books like [62].

Dissipative systems will behave differently than conservative systems. The states of the system will decay towards an equilibrium. Still, it might be possible to identify an invariant manifold on which the motion will always stay. Put in other words, the manifold for the dissipative system must contain the global attractor (the equilibrium) and have the invariance properties (i.e. always remain on the manifold). Such objects, apparently discovered at the end of the 80's, are called inertial manifolds [63]. Although a number of papers have been published within the topic of inertial manifolds, dissipative systems have received far less attention than conservative systems [64]. Also, many of the papers regarding inertial manifolds are heavily focused on strict mathematics and proofs of existence of inertial manifolds for given systems. An overview of the relatively newly introduced objects (i.e. inertial manifolds) can be found in [65].

Here, we take a less rigid mathematical view than is common in papers regarding inertial manifolds. This implies that we take the existence of the inertial manifold for granted. No attempt is made to prove its existence. Hence, the problem is reduced to finding the inertial manifold. This will be adressed in the following, and we will also give an example where our proposed method is used.

5.1   Methodologies

5.1.1 Naive adding of dissipation after reduction

In the chapters 4 and 3, we have discussed invariant manifolds for conservative systems and how they can be created. The subject of external forcing was also adressed.

A very simple method of creating a reduced model of a dissipative system is to regard the dissipative forces as external forces. Hence the system can be seen as a conservative system with external forces. The invariant manifold for the conservative system (disregarding the 'external forcing') can then be found, for instance, by using one of the methods presented earlier (see 4.1). The second step is to include the dissipative forces into the dynamics of the manifold. Possible ways of including external forcing has been outlined in a previous section (see 4.2). It is, however, again necessary to point out that this kind of treatment violates the invariance properties of the manifold, thus resulting in inaccuracies in the reduced model. By employing the method proposed in section 4.2 regarding consistent treatment of external forcing, this inaccuracy may to a certain extent be controllable, but at the cost of having a larger reduced model.

Despite the disadvantages pointed out, the simplicity of the method makes it very tempting to use. Any results should, however, be treated with care, having the drawbacks of the method in mind.

5.1.2 Galerkin-based method

In an earlier chapter, we briefly mentioned that Galerkin-methods may be used to find the invariant manifold for conservative systems. Such a method, and the use of it, has been presented recently in [50]. Although no examples for dissipative systems are given in the paper, it appears that the method can be used also for such systems. The nonlinear Galerkin method is commented on in section **??**.

5.1.3 A method based on simulations of the system

In the following we present a method that is capable of tracing the inertial manifold for dissipative systems. We have recently presented the method and the use of it in [66]. To give an outline of the method, we will first briefly review specific subjects regarding manifolds for conservative system. This will lead us to the newly proposed method for finding manifolds for dissipative systems.

In section 4.1.3, we presented very briefly a method relying on periodicity constraints [52], valid for conservative systems. The principle behind the method was to compare two simulations, one backward-in-time and one forward-in-time. Assuming periodicity and equal initial conditions on the manifold, the two simulations both lasting one period, should be equal.

Such a method, relying on periodicity constraints, appears to be useless for dissipative systems, since the trace backward in time and forward in time
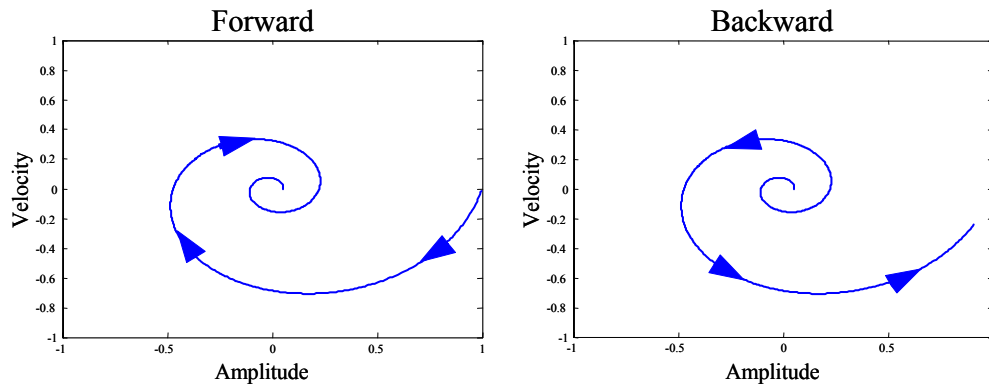
Figure 5.1: Left plot demonstrates the trajectory of a temporal simulation (forward in time) of a dissipative system. Right plot shows the same system simulated backwards in time. We note that the trajectories follows the same path.

from a given state clearly will never intersect. This is due to the dissipative nature, where energy is removed from the system as time passes. For the opposite case, where the time-axis is in opposite direction (i.e. backward in time), the system energy will increase with (negative) time.

At this stage we observe that the manifold for the systems is tangential to the phase-plane of the linear mode for low levels of energy. The challenge is therefore to find the manifold for increasingly larger amplitudes and energy-levels. Contrary to this, we see that dissipative systems will decrease energy level and amplitude with time.

At the same time, we note that the results from a temporal simulation, may be reproduced by starting with the final results and running backwards in time. Focusing on dissipative systems, we realize that this may not necessarily be correct in a numerical simulator, since certain modes may numerically have died out when doing the forward simulation. On the other hand, a simulation that is steadily injecting energy into the system, can be reversed and one will obtain the same results going forwards and backwards in time, see fig. 5.1. This procedure will, of course, be more complicated in the presence of instabilities, bifurcations, etc., but this is disregarded at present.

A temporal simulation (forward in time), starting off at a point on the manifold, will obviously always stay on the manifold. Following the earlier argument, so will a simulation running backward in time. Hence, one is capable of expanding the range of the known manifold, since simulations backwards in time means increasing amplitude.

While the principle appears simple, the method suffers from some drawbacks. One major drawback is that a single simulation only traces a line on the manifold. Performing a number of simulations with different initial

67

conditions will give more traces (that is, change phase of initial mode, but not amplitude, so that initial conditions still remain on the small signal manifold). From these traces, one may then approximate the shape of the rest of the manifold. Thus to obtain an accurate manifold a number of simulations must be performed. Following this approach, the construction of higher-degree manifolds requires a large number of simulations, making the method impractical for high-degree manifolds.

Numerical issues deserve special attention. Since the manifold is known at small amplitudes, the starting point is also known. Due to limited numerical accuracy, it is likely that other modes will be slightly inaccurately excited. While in dissipative systems, small errors will be damped out and disappear with time, the opposite will happen in a system where energy is injected. The initial small error will grow as more and more energy is injected into an incorrectly excited mode. Care must therefore be taken to ensure numerical accuracy.

As earlier mentioned, the way the method is outlined here, it is not capable of handling instabilities and bifurcations. However, also the other methods presented here, suffers from the same problem.

The implementation of this method is, in principle, quite simple, which is its clear advantage over the other methods. Nothing special is needed except a solver that is capable of performing temporal simulations both forward and backwards in time. An alternative is to change the definition of the system, a slight modification regarding signs is the same as running a simulation backward in time. A further advantage is that the method directly outputs the dynamics of the reduced system.

5.2 Example: Reduced-order model of a dissipative dual axis accelerometer

Following what we presented in [66], we will now present an example utilizing the methodology presented above. The example is based on the previously presented dual-axis accelerometer, see section 4.5, but with the difference that the top glass of the cavity is included here, see fig. 5.2. The relatively small distance between the glas and the masses, as compared to the surface area of the masses, gives rise to a squeeze-film effect (figure is not correctly scaled). While other dissipative effects will also be present, squeeze-film damping is by far the most important, given the system dimension and pressure of the surrounding gas. Therefore we have ignored other dissipative effects.

Altough the accelerometer considered here is equivalent to that in section 4.5, we do not use the same model description. One reason for this is that the reduction method applied earlier required a model description in polynomial form, whereas here we have chosen to use a nonlinear FE-model, where the nonlinearity is found numerically (i.e. using standard nonlinear
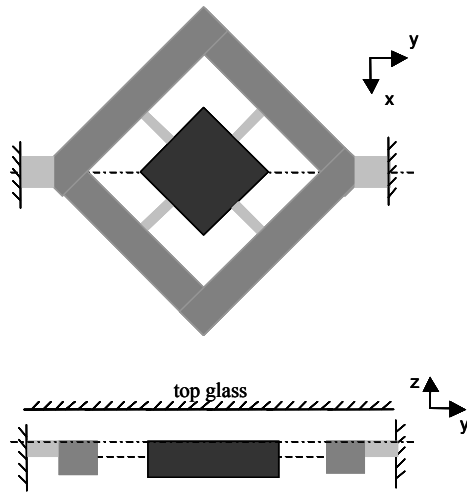
Figure 5.2: Schematic view of the dual-axis accelerometer investigated. Note that we have included the top glass. Detection is done for x- and z-axis acceleration (Courtesy of SensoNor ASA. Patent pending EP 00305807.0).

FE-formulation). Although possibly slower, this is clearly a more general scheme, and presumably also more accurate.

To accurately model the effects arrising from the surrounding gas, a complete CFD (computationally fluid dynamics) analysis should be performed coupled with the mechanical model. In principle, one may use available software packages for this, but this possibility is limited due to our special use. Furthermore, a CFD-analysis is quite extensive. Therefore we chose to implement a simplified model of the squeeze-film damping. Analytical squeeze-film damping, parallel to what was used in section 2.5 on reduced models of linear systems, was implemented. Stiffness introduced by the squeeze-film effects, early proved unimportant and was disregarded. However, since we at this stage are interested in nonlinear effects, we made the squeeze-film damping inverse proportional to the cube of the gap (i.e. gap between surface area of the mass and the top glas). Although not as precise as a full CFD-model, references indicate that this nonlinear adaption can be acceptable [34],[39].

5.2.1 The program package

The general process and main elements of the package is shown in fig. 5.3. It was buildt in the commercial mathematical program Matlab.

The first task is to establish the full nonlinear model, using the "Model-Builder", see fig. 5.3. The next step is to choose the basis-vectors of the reduced model. Although these vectors can in principle be chosen freely, our implementation limits the choice to the eigenvectors. In addition, we have

to define a suitable set of simulations that will span the manifold sufficiently. Since the manifold is approximated by interpolations between the states simulated, this choice is clearly important. This is further emphasized by the fact that simulation time is directly proportional with the number of simulations that must be done.

To facilitate the special needs of MEMS-structures, the simulation tool "SimTool", in fig. 5.3, is buildt to handle large displacements and a simple form of nonlinear squeeze-film damping. Fig. 5.3 indicates that "SimTool" can be run several times as defined by "ReductionChoice". Having obtained the set of solutions, the full-scale simulations are finalized.

With these results, the system's response is known within a defined range that is limited by the full-scale simulations, and a reduced dynamic model can be extracted. This is done within the elements "ManifoldCreate" and "ManifoldCreate2". In the former, we create the dynamics of the reduced model. From the temporal simulations (backwards in time) that trace out points on the manifold, we approximate the parameters in the reduced model. The reduced model is of the form:

$$
\begin{bmatrix} \dot{\phi} \\ \dot{A} \end{bmatrix} = \begin{bmatrix} \alpha \\ \beta \cdot A \end{bmatrix} + \begin{bmatrix} f_\phi\left(A, \phi\right) \\ f_A\left(A, \phi\right) \end{bmatrix} \tag{5.1}
$$

Here, ϕ and A are respectively phase and amplitude of the retained mode(s). The functions $f_\phi\left(A, \phi\right)$ and $f_A\left(A, \phi\right)$ approximate the nonlinearities of the manifold. Hence eq. 5.1 should be fitted to the simulation results. To approximate the nonlinear effects, we use:

$$
f_\phi\left(A, \phi\right) = \sum_m a_m A \cos\left(b_m \phi + \tau_m\right) \tag{5.2a}
$$

$$
f_A\left(A, \phi\right) = \sum_m c_m A^2 \cos\left(d_m \phi + \eta_m\right) \tag{5.2b}
$$

The parameters in eq. 5.1 and 5.2 are found using an optimal approximation of eq. 5.1 to the simulation results. Clearly, more complex functions that may capture more nonlinearities can be chosen in eq. 5.2 to improve performance.

In "ManifoldCreate2" the relation between the slave modes and the retained mode(s) is created. This can either be done by means of an approximating function, parallel to the procedure in "ManifoldCreate", using functions like:

$$
\phi_{\mathrm{modelled},j} = \sum_{n,m} o_{j,n,m} A^n \cos\left(p_{j,n,m} \phi + \sigma_{j,n,m}\right)
$$

$$
A_{\mathrm{modelled},j} = \sum_{n,m} q_{j,n,m} A^n \cos\left(r_{j,n,m} \phi + \psi_{j,n,m}\right)
$$

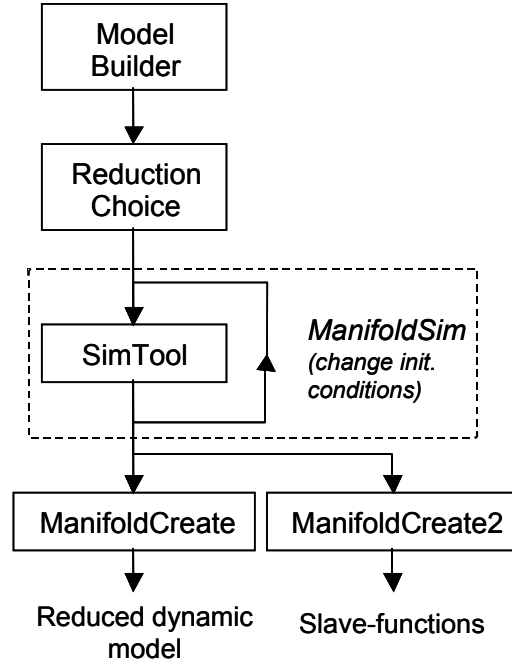Where the phase and amplitudes of the modelled (slave) modes ($\phi_{\mathrm{modelled},j}$,

Figure 5.3: Schematics of the program package, showing the sub-routines.

$A_{\text{modelled},j}$) becomes function of the amplitude and phase of the retained modes (ϕ, A). Another alternative is to use a numeric scheme, where the functions are defined by using linear interpolation of the simulation results.

The approach for finding the reduced model is in clear contrast to the method used in the asymptotic approach. In the latter, the relation between the slave and retained modes are first found, and then re-inserted into the full model description obtaining the dynamics of the reduced model. In the approach we present here, having the relation between the slave and retained modes is not a prerequisite to create the dynamics of the reduced model in terms of the retained degree of freedom. However, the information for creating the relations is at hand.

5.2.2 Simulation results

A preliminary analysis indicates that there are two dominant modes in the system, the torsion of the assembly about the y-axis (mode 1), and the z-axis deflection of the central mass (mode 2). This is parallel to our findings for the undamped system presented in section 4.5. In the analysis, we select one of the dominant modes as our retained modes, leaving the other modes as slave modes.

Creating the dynamics of the reduced model, we utilized the functions presented in eq. 5.1 and 5.2. Linear interpolation was used to obtain the
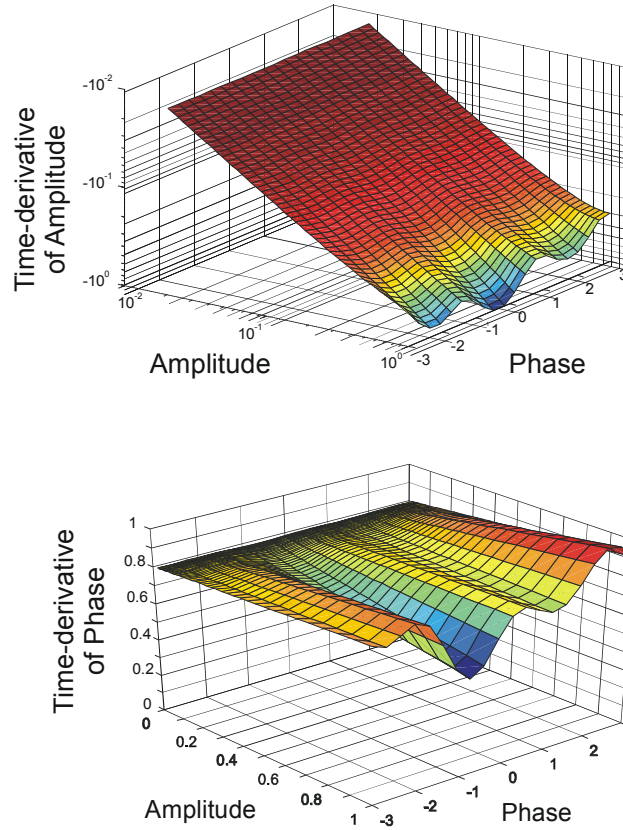
71

Figure 5.4: Plots of the dynamics of the retained mode (mode 2). Top: amplitude-velocity plotted as function of amplitude and phase. Bottom: Phase-velocity plotted as function of amplitude and phase. For both plots, wave-formation on right side are nonlinear effects. Note that the plots are normalised.

relations between the slave modes and the retained mode.

5.2.2.1 Mode 2 - manifold

In the first manifold we created, we used mode 2 as the retained mode, hence mode 1 and the other modes where modelled. The initial analysis showed that mode 2 was underdamped. The dynamics of the manifold we obtain are shown in fig. 5.4, where we clearly note the nonlinearities of the system. For the sake of example, we also show the obtained manifold for the relation between the retained mode and one of the slave modes, see fig. 5.5. In the plots, the amplitudes are normalized.

So far, we have not verified the key to success, namely the equivalence of the simulations backward in time with those performed forward in time. Early simulations performed backward in time, revealed that high-frequency
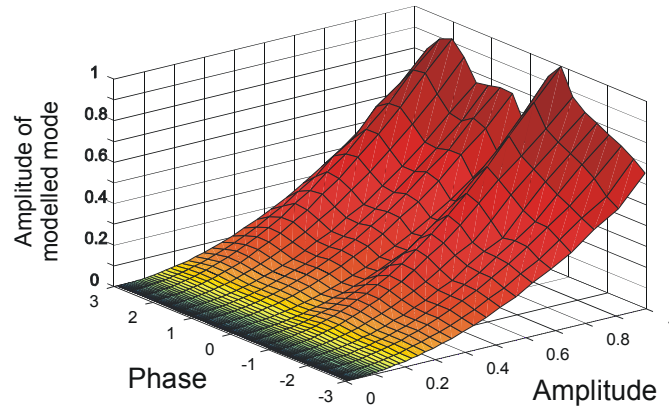
Figure 5.5: The plot shows how the amplitude of a slave mode varies with amplitude and phase of the retained mode (mode 2).

components grew quickly and unstable. Although the unstable growth may be said to be the core of the concept for finding the manifold, it was necessary to take proper measures to prevent unstable growth of high-frequency components in the backward in time simulations, resulting from inaccuracies in the numerical procedures. These measures have to be handled with care since they appear as a double-edged sword. The upside is that they should prevent the rapid growth of the high-frequency components, the downside is that these components may be part of the solution and therefore should not be removed. These issues where solved to an acceptable degree, but further improvement is clearly possible.

Having reduced numerical errors, the next step where to compare the simulations backward in time with those performed forward in time. Early simulations indicated that the equivalence degraded with longer simulation time. This is not surprising. To illustrate the accuracy of the manifold we created, we performed normal simulations (forward in time) both of the full system, and of the reduced model. Results are shown in fig. 5.6. Higher initial amplitude would result in larger deviation between the result from the reduced system and the full system. Lower initial amplitude would equally give more equivalent result.

The deviation between the results of the full system and the reduced system, has mainly two causes. The first stems from inaccuracies due to numerical issues, which both the backwards simulations and the forward simulations suffer from. However, the numerical errors may be different in nature for the two situations. Numerical errors in the backwards simulations lead to an inaccurate definition of the defining point on the manifold. Hence, any exact simulation of the full system is deemed to be only approximately equivalent
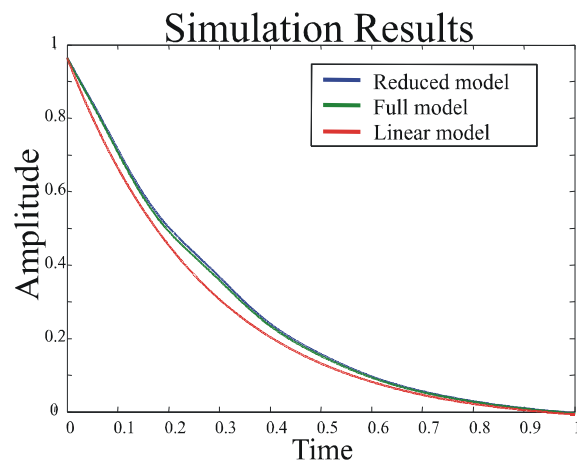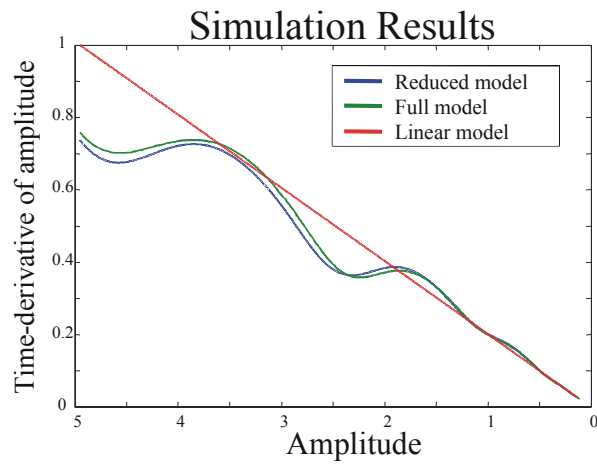
73

Figure 5.6: The plots illustrates the accuracy of the manifold we found. Temporal full-system simulations are compared with the simulations of the reduced model (all simulations forward in time). Shown is the retained mode, mode 2.

to those of the reduced system. The second cause of deviation is related to the limitation of the approximating functions of the nonlinearities (eq. 5.1, 5.2). The limited flexibility in these functions (eq. 5.2) restricts the shape of the manifold, so that it might be impossible to fit the approximate manifold to the simulation results that defines the manifold. Clearly, this problem may be alleviated by increasing the complexity of the approximating functions in eq. 5.1.

5.2.2.2 Mode 1 - manifold

In this second example, we choose mode 1 as the retained mode, leaving mode 2 and all other modes as slaves. Initial simulations showed that mode 1 was overdamped. The nature of an overdamped mode is significantly different from an underdamped mode. This manifests itself in the relation between displacement and velocity of the mode, assuming no external influence. If the displacement is known for an overdamped mode, the velocity is given, and hence the amplitude is a function of one parameter only (the displacement or alternatively velocity). For the underdamped mode, however, the amplitude is a function of both displacement and velocity, since the two are initially uncorrelated. The latter manifests itself in that an underdamped mode will stay on a surface, whereas the relation between amplitude and phase of an overdamped mode reduces the surface to a line.

Since mode 1 is overdamped, such a manifold may be simplified and described only by the amplitude. This is done in fig. 5.7, where the torsional amplitude is plotted versus amplitude of mode 1. Alongside, the linear mode 1's contribution is plotted, showing significant discrepancies at larger amplitudes. However, with the inclusion of one slave mode (mode 3), determined via numerical interpolation from the defining simulations, the estimation of the angular deflection becomes much better.

5.3 Discussion and conclusion

We have presented a methodology for constructing manifolds in dissipative systems. The procedure is simple, and may be easily implemented in solvers readily available. The numerical accuracy of the procedure may be increased by adding certain subroutines to the solver used. Although not discussed, problems related to bifurcations and instabilities apparently remain as a problem also within this methodology.

While only demonstrated for 1-d.o.f. manifolds, the method can easily be used for higher-degrees manifolds. This comes at an increased computational cost.

The methodology for tracing out manifolds has been applied to a dual-axis accelerometer. Quasi-analytical manifolds were obtained from a polynomial fit to the numerical results. This reduced model is nonlinear in nature and al-
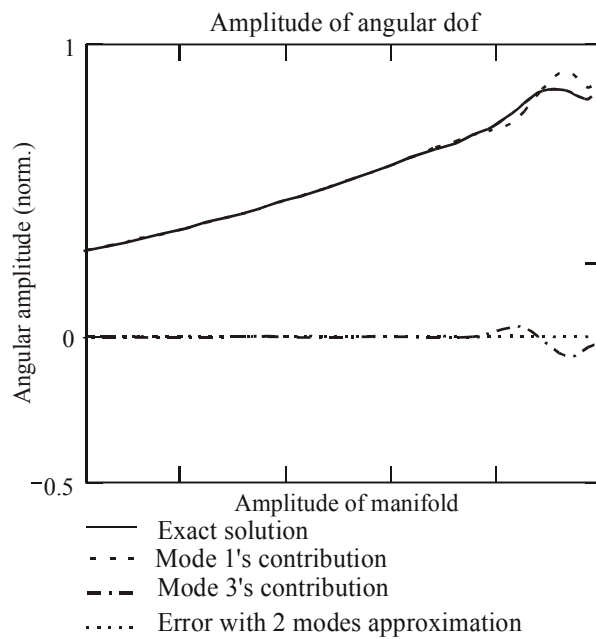
Figure 5.7: The (normalised) amplitude of angular deformation in torsional beam is plotted as function of amplitude of of the manifold. Mode 1 (over-damped) defines the manifold at small amplitudes. Note that estimating the physical deformation with only two linear modes gives a very small error.

lows for quasi-analytical inspection of the nonlinear behaviour of the system. Nonlinear behaviour of the system was successfully identified in the reduced model, although the second and third order polynoms used in the reduced model have limited validity at large nonlinearities.

PART II

Lumped Modelling

Chapter 6
Lumped Modelling Of A Microfilter

The purpose of this chapter is to present general modelling and simulation aspects, applicable to a microresonator. The knowledge and results obtained from that will also be presented. The microresonator's elements are in two main energy domains, namely the mechanical and the electrostatic. To be able to model the system there is a need for understanding mechanics and electrostatics. The necessary theory is presented. We choose to use equivalent circuits of the mechanics to be able to model the system in an electrical domain simulator.

Mechanical filters used in electronics have been a subject of research for a number of decades. A significant number of publications from the 1960's and the 70's can be found (see e.g. [67],[68] and references therein). Various types of mechanical filters have been proposed, and a number have also been produced in large numbers for industrial use [67]. Much of the advantages of MEMS was, however, at that time either unknown or inaccesible for practical use. However, with the continuously increasing knowledge and processing capabilities of microstructures, new opportunities have emerged in the area of mechanical filters/resonators for electronics. The microresonator described in [69] is an example of this, shown schematically in fig. 6.1. The structure is quite different from common structures seen in the 70's, but is still operating with the same mechanically principles. The electromechanical readout, however, is different. This is a direct result of the MEMS-technology.

While some research has been carried out in this intriguing area, it appears that there is still a long way to go before micromechanical filters/resonators have reached their full potential. The objective of this part is therefore to highlight modelling aspects, with a primary goal of constructing simple models that builds physical insight.

6.1   Operating principle and geometry of a microfilter/resonator

The microresonator investigated in this chapter is of a type proposed in [69]. The structure is shown in fig. 6.1. As can be seen, the system consists of two clamped beams, with an interconnecting beam between. The red areas denote pads, where electrical potential can be applied. With a potential applied, electrostatic forces will set the beam(s) in motion.

Assuming that one beam only has been excited and is vibrating, the interconnecting beam will couple the second beam to the motion of the initially excited beam. The coupling of the two beams results in a transfer-function
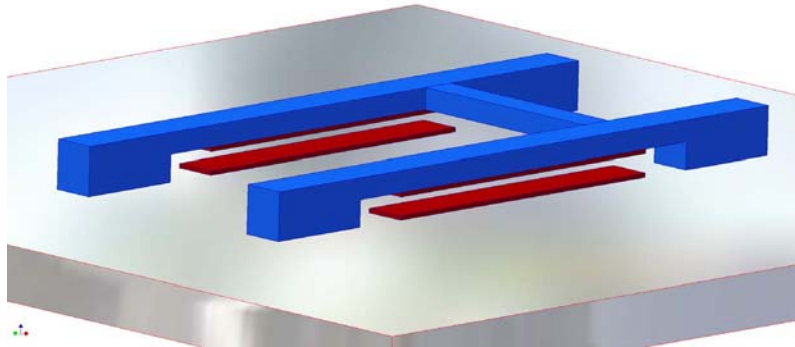
Figure 6.1: Figure of the microfilter. Red area denotes pads.

with certain properties, which will be discussed later. The deformation of the second beam may then be read by detecting capacitance since the capacitance is dependent upon the gap-size..

It is clear that modelling such a systems means describing both mechanical and electrical behaviour, including the electrostatic forcing, which links the electrical domain with the mechanical domain. Usually, in most systems, both domains are too complex to be fully described analytically. Instead the mechanical domain is often modelled by means of the finite element method whereas the electrostatics is best modelled using the boundary element method. Few simulators allows for using different methods in one calculation. Neither will such an approach establish a very good physical intuition about the system. For these reasons, we have chosen to separate the modelling of the two domains, and couple them to describe the full system at a later stage.

6.2 Governing equations in mechanics

The Cauchy-equation serves as the fundamental governing equation of mechanics, just as the Maxwell equations are the fundamental equations of electrodynamics. The assumption of continuity is observed, and the Cauchy-equation reads:

$$\nabla \cdot \mathbf{T} + \rho \mathbf{b} = \rho \mathbf{a}$$

Here $\mathbf{T}$ is the stress tensor, $\mathbf{b}$ is the body forces, $\mathbf{a}$ is acceleration, and ρ is the density of the material.

6.2.1 Beam theory

In this section a brief review of beam theory is given. This is obviously of importance, since the main mechanical building-blocks of the microresonator are beams.

The most commonly encountered beam is perhaps the slender beam. The modelling of long, thin beams is done using Euler-Bernoulli theory. Following this commonly used theory, the governing equation of forced lateral vibration of a nonuniform beam is [70]:

$$\frac{d^2}{dx^2}\left(EI(x)\frac{d^2}{dx^2}w(x,t)\right) + \rho A(x)\frac{d^2}{dt^2}w(x,t) = f(x,t)$$

The parameters are: E Young's modulus, I second moment of area, A cross-sectional area, x position along beam, t time, w transversal deflection of beam, f force. For a uniform beam, we obtain the governing equation:

$$EI\frac{d^4}{dx^4}w(x,t) + \rho A\frac{d^2}{dt^2}w(x,t) = f(x,t)$$

The equations are based on elementary beam theory. Proper boundary conditions must be imposed when solving the problem.

For thicker beams, effects of rotary inertia and shear deformation become increasingly important. These effects are included in the Timoshenko beam theory. The equation for forced vibration of a uniform beam is [70]:

$$EI\frac{d^4}{dx^4}w + \rho A\frac{d^2}{dt^2}w - \rho I\left(1 + \frac{E}{kG}\right)\frac{d^4}{dx^2dt^2}$$
$$+\frac{\rho^2 I}{kG}\frac{d^4}{dt^4}w + \frac{EI}{kAG}\frac{d^2}{dx^2}f - \frac{\rho I}{kA}\frac{d^2}{dt^2}f - f = 0$$

where k is the Timoshenko shear coefficent and G is the shear modulus. For free vibration of a simply supported beam, this reduces to:

$$EI\frac{d^4}{dx^4}w + \rho A\frac{d^2}{dt^2}w - \rho I(1 + \frac{E}{kG})\frac{d^4}{dx^2dt^2} + \frac{\rho^2 I}{kG}\frac{d^4}{dt^4}w = 0$$

We search for the natural frequencies of a simply supported beam. Assuming the deformation shape:

$$w(x,t) = C\sin\left(\frac{n\pi x}{L}\right)\cos\left(\omega_n t\right)$$

And the beam equation reduces to:

$$\omega_n^4 + \omega_n^2 K_1(n) + K_2(n) = 0$$

We note that for each n, we have two natural frequencies, the lower corresponding to bending deformation mode and the higher corresponding to the shear deformation mode. While the two natural frequencies are different, the mode shapes are equal [70], see also fig. 6.2.

Other and more sophisticated beam theories exist. E.g. does third-order theory take into account a more accurate stress-distribution than Timoshenko beam theory does [71]. Although these more advanced methods should be
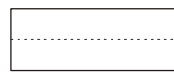
A) Undeformed beam
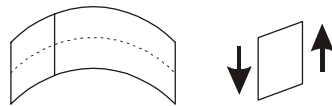
B) Shear deformation
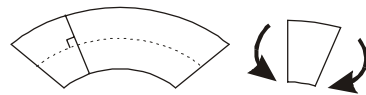
C) Bending deformation

Figure 6.2: Deformation shapes of a simply supported beam. The shape of the shear deformation mode and bending deformation mode are equivalent when we look at the central axis of the beam (broken line). The cross-sectional deformation of the beam is, however, dependent upon deformation mode.
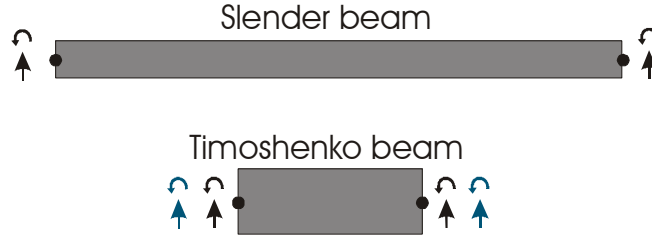
Figure 6.3: The notation for both Euler-Bernoulli elements and Timoshenko beam elements are shown above. The blue arrows are in the case of seperation between shear and bending deformation in the Timoshenko beam element.

more accurate, a possibly larger source of inaccuracy is, for short and thick beams, the complex stress-distribution (and for that case the dynamics) that possibly exists nearby the boundary conditions. These effects are not included in general beam theory. To analyse the effects of the boundary conditions, a more in-depth nuumerical analysis must be performed. The need for a truely accurate beam theory for short beams is therefore of limited value. For these reasons, no other advanced theories than the Timoshenko beam theory are presented here.

6.2.2 Beam elements of Euler-Bernoulli and Timoshenko beams

In the above, we presented the governing equation for an Euler-Bernoulli beam. However, the form of the equation limits the practical use. A more suitable form to describe the behaviour is by means of a finite element. This makes it much easier to model system with several joined elements, like beams, masses and dampers. The Euler-Bernoulli beam element is indeed well-known and commonly used. Presented with two degrees of freedom at each node, it is:

$$
\begin{bmatrix} F_1 \\ M_1 \\ F_2 \\ M_2 \end{bmatrix} = \begin{bmatrix} \frac{12EI}{L^3} & \frac{6EI}{L^2} & -\frac{12EI}{L^3} & \frac{6EI}{L^2} \\ \frac{6EI}{L^2} & \frac{4EI}{L} & -\frac{6EI}{L^2} & \frac{2EI}{L} \\ -\frac{12EI}{L^3} & -\frac{6EI}{L^2} & \frac{12EI}{L^3} & -\frac{6EI}{L^2} \\ \frac{6EI}{L^2} & \frac{2EI}{L} & -\frac{6EI}{L^2} & \frac{4EI}{L} \end{bmatrix} \begin{bmatrix} u_1 \\ \phi_1 \\ u_2 \\ \phi_2 \end{bmatrix} \quad (6.1)
$$

See fig. 6.3 for directions. In a more compact fashion and including also inertial forces, it is written as:

$$ [F] = [M] [\ddot{x}] + [K] [x] $$

While Timoshenko beam theory is quite well known, finite elements representing the Timoshenko beam are less often encountered. In the literature, various elements trying to replicate the properties of the Timoshenko beam have been presented [71], [72], [73], [74]. There are two basically different approaches to representing such an element. One way is to change the

mass and stiffness matrices so as to reflect the increased influence of rotary inertia and shear deformation with increased thickness of the beam. The other method is to split the state-vector into bending deformation and shear deformation, leading to an increased number of states. However, this method will directly give two natural eigenfrequencies per degree of freedom, whose existence are indicated in the Timoshenko beam equation. Below, general equations for both approaches are shown:

$$
\begin{aligned}
[F] &= [M + \Delta M][\ddot{x}] + [K + \Delta K][x] \\
\begin{bmatrix} F \\ 0 \end{bmatrix} &= \begin{bmatrix} M_{11} & M_{12} \\ M_{21} & M_{22} \end{bmatrix} \begin{bmatrix} \ddot{x}_{bend} \\ \ddot{x}_{shear} \end{bmatrix} + \begin{bmatrix} K_{11} & K_{12} \\ K_{21} & K_{22} \end{bmatrix} \begin{bmatrix} x_{bend} \\ x_{shear} \end{bmatrix}
\end{aligned}
$$

6.2.3 Nonlinear Beams

So far, only linear systems have been presented. This may be a serious over-simplification in some systems, since nonlinearities may be present. Non-linearities may stem from large displacement (large geometrical changes of structure) or material nonlinearity. External effects, like damping, may obviously also introduce nonlinearities in the system, but they are not discussed here. Nonlinear mechanical systems are often solved numerically by iteration. In this chapter, we will not discuss nonlinear beams.

6.2.4 Consistent forcing in finite element models

Consider a distributed external force over e.g. a part of a beam. Given the nodes, it is quite tempting to simply redistribute the external forcing so that it can be allocated to the nodes. Although apparently correct, simply re-distributing the external force over the nodes is in fact generally inconsistent. To find the consistent forces, the shape-functions of the elements need to be considered. The shape functions are the link between nodal displacement and the displacement between the nodes, and are used to derive the element matrices. Details on this can be found in i.e. [4].

6.3 Electrical equivalent of mechanical systems

The preference for using different strategies for different energy domains have already been mentioned. While there are good reasons for this, other arguments can be made for treating the different domains in a consistent environment. For example, mechanical finite element models can be represented in terms of electrical equivalent circuits, enabling the electrical circuit designer to use well-known simulators like SPICE. Equivalent circuits and how to build them will be presented here.

At a first glance, one should note similarities between mechanical lumped systems and electrical circuits. In electrical circuits, Kirchoff's voltage law and current law, are akin to Newton's 2. law and the kinematic equations in
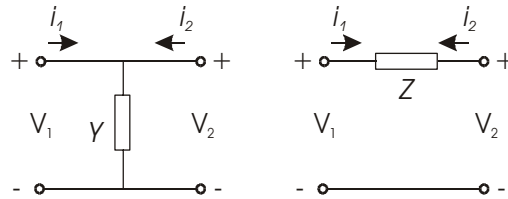
Figure 6.4: Two simple two-port elements.

mechanics. But before discussing how to construct electrical equivalents of mechanical finite element models, some basic knowledge regarding electrical systems are presented. The analogies between the electrical and the mechanical domains are also investigated to enable us to construct the equivalent circuits correctly.

6.3.1 Two-port elements

A convinient way of representing electrical circuits is by the use of two-port elements. Of course, n-port elements may also be used, but a two-port element suffices here. Assuming the element to be linear, a relation between voltage and current at the ports can be written in terms of the $[ABCD]$-matrix reference:

$$\begin{bmatrix} V_1 \\ i_1 \end{bmatrix} = \begin{bmatrix} A & B \\ C & D \end{bmatrix} \begin{bmatrix} V_2 \\ -i_2 \end{bmatrix}$$
$$ABCD = \begin{bmatrix} A & B \\ C & D \end{bmatrix}$$

Two simple general examples are shown in fig. 6.4 to demonstrate the method.For these two examples, the matrices becomes:

$$[ABCD] = \begin{bmatrix} 1 & 0 \\ Y & 1 \end{bmatrix}$$
$$[ABCD] = \begin{bmatrix} 1 & Z \\ 0 & 1 \end{bmatrix}$$

Besides the two basic elements presented, a few more elements may come in handy, these are presented in the table:

Figure	$[ABCD]$	Name
	$\begin{bmatrix} N & 0 \\ 0 & \frac{1}{N} \end{bmatrix}$	Transformer
	$\begin{bmatrix} 0 & -\frac{1}{f} \\ -g & 0 \end{bmatrix}$	Gyrator
	$\begin{bmatrix} 1 & 0 \\ j\omega C & 1 \end{bmatrix}$	
	$\begin{bmatrix} \frac{1}{Y_b}\left(Y_b + Y_c\right) & \frac{1}{Y_b} \\ Y_a + \frac{Y_a Y_c}{Y_b} + Y_c & \frac{Y_a}{Y_b} + 1 \end{bmatrix}$	π-network

6.3.1.1   Larger circuits

Two-ports can be combined in different ways to represent larger circuits. If the system is made up of a set of two-ports connected in cascade, the use of $[ABCD]$-matrices are simple and straight forward. In such cases, the resulting $[ABCD]$-matrix can be found by multiplying the $[ABCD]$-matrices of the two-ports (although one must take proper care of sign conventions):

$$[ABCD_{total}] = [ABCD_1]\,[ABCD_2]\dots[ABCD_N]$$

An alternative description involves the use of admittance matrices. How port-elements are connected using the admittance matrix is shown in fig. 6.5. Each of the two-ports may f.ex. consist of the previously shown π-network.
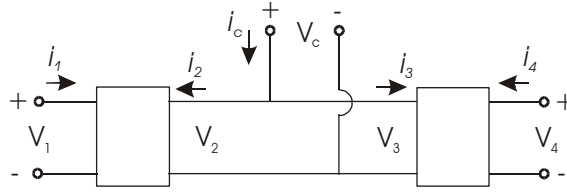
Figure 6.5: The cascading of 2 two-port elements, resulting in a three-port element.

In that case, we have the following admittance matrix before connection:

$$\begin{bmatrix} I_1 \\ I_2 \end{bmatrix} = \begin{bmatrix} Y_a + Y_b & -Y_b \\ -Y_b & Y_b + Y_c \end{bmatrix} \begin{bmatrix} V_1 \\ V_2 \end{bmatrix}$$

$$\begin{bmatrix} I_1 \\ I_2 \\ I_3 \\ I_4 \end{bmatrix} = \begin{bmatrix} Y_a + Y_b & -Y_b & 0 & 0 \\ -Y_b & Y_b + Y_c & 0 & 0 \\ 0 & 0 & Y_d + Y_f & -Y_f \\ 0 & 0 & -Y_f & Y_f + Y_g \end{bmatrix} \begin{bmatrix} V_1 \\ V_2 \\ V_3 \\ V_4 \end{bmatrix}$$

We join by equating currents and voltages at the connecting node:

$$\begin{bmatrix} I_1 \\ I_c \\ I_4 \end{bmatrix} = \begin{bmatrix} 1 & 0 & 0 & 0 \\ 0 & 1 & 1 & 0 \\ 0 & 0 & 0 & 1 \end{bmatrix} \begin{bmatrix} I_1 \\ I_2 \\ I_3 \\ I_4 \end{bmatrix} = [T_1] \begin{bmatrix} I_1 \\ I_2 \\ I_3 \\ I_4 \end{bmatrix}$$

$$\begin{bmatrix} V_1 \\ V_2 \\ V_3 \\ V_4 \end{bmatrix} = \begin{bmatrix} 1 & 0 & 0 \\ 0 & 1 & 0 \\ 0 & 1 & 0 \\ 0 & 0 & 1 \end{bmatrix} \begin{bmatrix} V_1 \\ V_C \\ V_4 \end{bmatrix} = [T_2] \begin{bmatrix} V_1 \\ V_C \\ V_4 \end{bmatrix}$$

This means that:

$$\begin{bmatrix} I_1 \\ I_c \\ I_4 \end{bmatrix} = [T_1] \begin{bmatrix} Y_a + Y_b & -Y_b & 0 & 0 \\ -Y_b & Y_b + Y_c & 0 & 0 \\ 0 & 0 & Y_d + Y_f & -Y_f \\ 0 & 0 & -Y_f & Y_f + Y_g \end{bmatrix} [T_2] \begin{bmatrix} V_1 \\ V_C \\ V_4 \end{bmatrix}$$

$$\begin{bmatrix} I_1 \\ I_c \\ I_4 \end{bmatrix} = \begin{bmatrix} Y_a + Y_b & -Y_b & 0 \\ -Y_b & Y_b + Y_c + Y_d + Y_f & -Y_f \\ 0 & -Y_f & Y_f + Y_g \end{bmatrix} \begin{bmatrix} V_1 \\ V_C \\ V_4 \end{bmatrix}$$

This example serve the purpose of demonstrating how n-ports may be created by adjoining 2-port elements. With this basic knowledge, the attention is turned to the electrical analogies.

87

6.3.2 The two analogies

Having presented both general two-port elements for electrical circuits and FE-description of mechanical beams, the next step is to look at how the mechanical system can be described in terms of electrical equivalents.

6.3.2.1 Basic electrical equations

The capacitor, resistor and inductor are described by the equations:

$$V = \frac{1}{C}\int I\,dt = \frac{1}{C}Q$$

$$V = RI = R\frac{d}{dt}Q$$

$$V = L\frac{d}{dt}I = L\frac{d^2}{dt^2}Q$$

We see the similarities with mechanical forces. Equivalent equations of the mechanical forces may be done in two manners, following either the $e \rightarrow V$ analogy (effort→voltage) or the $f \rightarrow V$ analogy (flow→voltage). In the mechanical domain, force is an effort while velocity is a flow.

		$e \rightarrow V$	$f \rightarrow V$
		Direct analogy	Mobility analogy
Mech.	El.		El.
F	V		I
$\frac{d}{dt}x$	I		V
$M\frac{d^2}{dt^2}x$	$L\frac{d^2}{dt^2}q = L\frac{d}{dt}I$		$C\frac{d}{dt}V = I, \qquad CV = q$
$D\frac{d}{dt}x$	$R\frac{d}{dt}q = RI$		$\frac{1}{R}V = I, \qquad \frac{1}{R}\frac{d}{dt}V = q$
Kx	$\frac{1}{C}q = \frac{1}{C}\int I\,dt$		$\frac{1}{L}\int V\,dt = I, \qquad \frac{1}{L}\int\int V\,dt^2 = q$

Recalling that a 1-d.o.f. mechanical system is written in the manner:

$$M\frac{d^2}{dt^2}x + D\frac{d}{dt}x + Kx = F$$

we see that the electrical equivalent in the $f \rightarrow V$-convention is:

$$C\frac{d}{dt}V + \frac{1}{R}V + \frac{1}{L}\int V\,dt = I \quad (f \rightarrow V)$$

From this it is seen that the mechanical elements that are placed in parallel have an equivalent circuit with electrical elements also placed in parallel. In the case of creating an electrical equivalent in the $e \rightarrow V$-convention, the result is:

$$L\frac{d^2}{dt^2}q + R\frac{d}{dt}q + \frac{1}{C}q = V \qquad (e \rightarrow V)$$
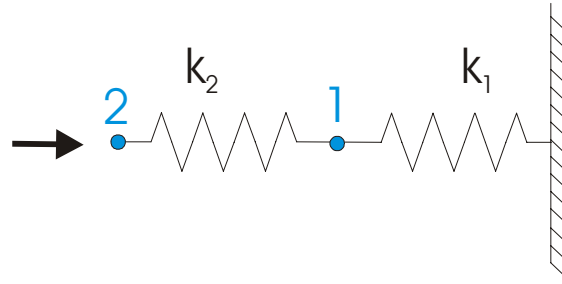
Figure 6.6: A simple mechanical system consisting of two springs.

This can be realized by placing the electrical elements in series. Hence it appears to be a relation between parallel mechanical elements and serial electrical elements and vice versa in the $e \rightarrow V$ analogy. For the general case, the system may have n d.o.f.'s. How these equivalent circuits can be constructed for such systems will be considered more closely in the following.

6.3.3 $e \rightarrow V$ (Direct analogy)

For the case of creating a network parallel to a mechanical finite element model with n d.o.f.'s, it is of importance to realize that the parallel to the stiffness and mass-matrix is the impedance matrix. Also, in many practical cases, the stiffness matrix may be inverted to obtain the compliance matrix. This, in turn, is the equivalent admittance matrix. From what was shown earlier, the relation between the admittance matrix and the circuit is quite simple. However, understanding the relationship between the electrical equivalent and the mechanical system need not to be based on the complicated matrix-inversion process, since this is not a very transparent process. A better alternative may be to look at single elements and what forces attack them. From this, equivalent circuits of each single element can be created. The second step will then be to join these electrical elements that can be connected without violating the governing equations. Doing this, it soon becomes apparent that there is a very close relationship between mechanical elements in parallel and electrical elements in series, and vice versa. However, for the general case, coupling elements exist that make it impossible to directly use the parallel-serial relation.

6.3.3.1 Example 1

Assume two springs connected in series, with the right side of the first spring fixed, see fig.6.6. The stiffness matrix for such a system is:

$$[K] = \left[\begin{array}{cc} k_1 + k_2 & -k_2 \\ -k_2 & k_2 \end{array} \right]$$
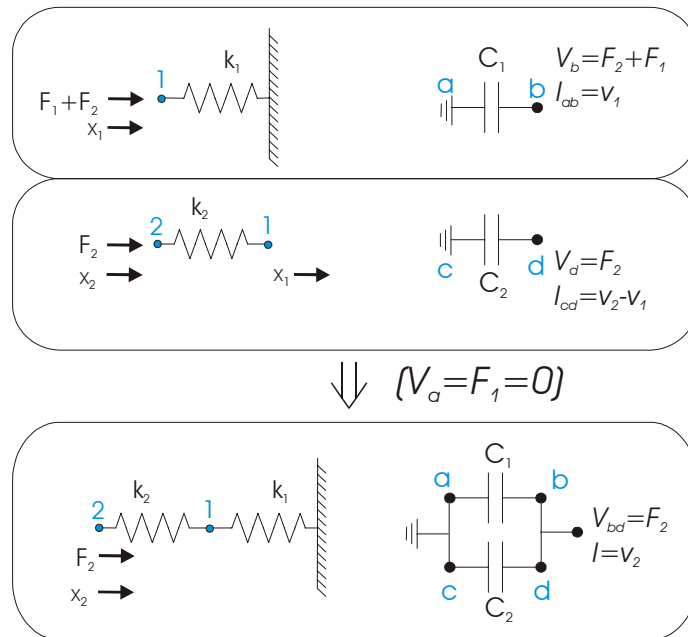
89

Figure 6.7: In the two upper boxes, the springs are separated, and the proper displacements and forces are shown. On the right side, the equivalent circuits are shown ($\frac{d}{dt}x = v$, $C = \frac{1}{K}$). The bottom box shows how these two springs are connected and what the equivalent circuit looks like. ($e \rightarrow V$ convention)

The admittance and impedance matrices then becomes:

Admittance, $[Y]$:	Impedance, $[Z]$:
$j\omega \begin{bmatrix} \frac{1}{k_1} & \frac{1}{k_1} \\ \frac{1}{k_1} & \frac{1}{k_1} + \frac{1}{k_2} \end{bmatrix}$	$\frac{1}{j\omega} \begin{bmatrix} k_2 + k_1 & -k_2 \\ -k_2 & k_2 \end{bmatrix}$

For this simple system, it is quite tempting to use the admittance matrix directly to create an equivalent circuit. However, we will here demonstrate the generally more transparent method of constructing an electrical equivalent of each single mechanical element, and then connect these small circuit-elements to form the equivalent of the full system. First, an equivalent of each single spring element is created, without being connected to any other elements, see fig. 6.7. Hence, each spring is designated its own equivalent electrical element (capacitance):

$$\begin{bmatrix} V_{ab} & \left(= & F_1 + F_2 \\ V_{cd} & & F_2 \end{matrix} \right) \end{bmatrix} = \begin{bmatrix} \frac{1}{Y_1} & 0 \\ 0 & \frac{1}{Y_2} \end{bmatrix} \begin{bmatrix} I_{ab} & \left(= & v_1 \\ I_{cd} & & v_2 - v_1 \end{matrix} \right) \end{bmatrix}$$

Secondly, the elements should possibly be joined. To aid in this, the mechanical analogies have been included in the equations. This is also done in fig. 6.7, where the task of joining the subcircuits appears quite manageable and understandable.
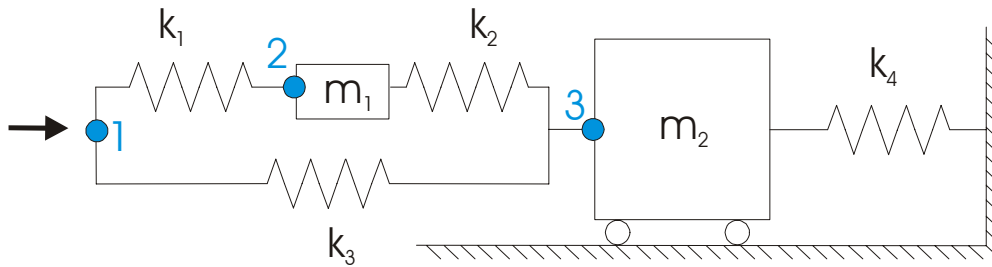
90

Figure 6.8: A system of 4 springs and 2 masses.

Here F_1 and F_2 are external forcing on the respective nodes.

6.3.3.2 Example 2

A more complex structure will now be analyzed. Assume the mechanical system shown in fig. 6.8. In this example, the starting point is to create electrical equivalents of each single spring element. From the topography, the electrical elements are joined to form the electrical equivalent of the static system, see left side in fig. 6.9. However, the circuit is not complete before the inertial effects are incuded in the electrical equivalent. Trying to implement the inertial effects in the same manner as the springs, reveals a problem. The inertial effects are a function of acceleration relative to ground. However, in fig. 6.9 it is apparent that the variables (current/displacement) needed are not directly available. Therefore, the inertial force must be reformulated to be in terms of available variables in the electrical equivalent:

$$
\begin{aligned}
m_1\ddot{x}_2 &= m_1\left(\ddot{x}_2 - \ddot{x}_3\right) + m_1\ddot{x}_3 \quad &\text{Reformulated} \\
m_2\ddot{x}_3 &= m_2\ddot{x}_3 \quad &\text{Ok}
\end{aligned}
$$

The effect can now be readily implemented in the equivalent circuit, which can be seen in right side of fig. 6.9.

Inserting the inertial effects in the electrical equivalent demonstrated that single mechanical elements may result in a number of electrical elements. The same can be true for spring elements, if their connections do not match available variables. These spring elements must be implemented in the same manner as the inertial effects was.

6.3.4 $f \rightarrow V$ (Mobility analogy)

While in the $e \rightarrow V$ analogy, the impedance matrix is the equivalent to the stiffness matrix, the admittance matrix is the equivalent to the stiffness matrix in the $f \rightarrow V$ convention. We recall that building an admittance-matrix for larger circuits, involved adding the admittance-values for the smaller two-ports to form the full admittance matrix. This is in direct parallel to the
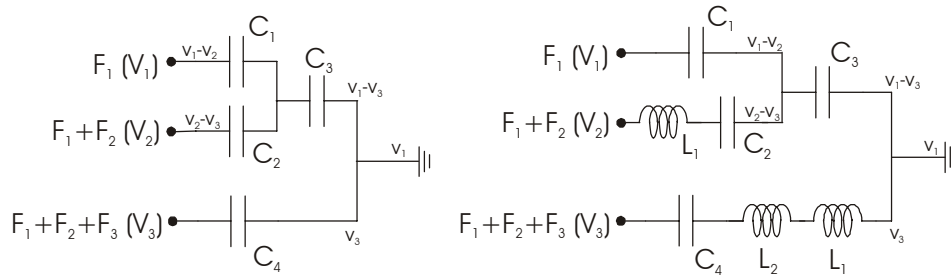
Figure 6.9: LEFT SIDE: Mechanical system with 4 springs, excluding the inertial forces. RIGHT SIDE: Equivalent circuit of the mechanical system with 4 springs, including the 2 masses.($e \rightarrow V$ convention)
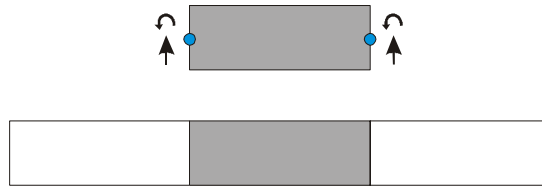
Figure 6.10: Picture of beam section along with directions used. Below is shown how a number of sections may be joined to form a longer beam.

creation of a stiffness matrix, where any new stiffnesses, e.g. arrising from a spring, is implemented in the matrix by simply adding it in at the correct places. Hence adjoining beam elements to nodes in the mechanical structure is equivalent to adjoining electrical equivalent to the nodes in the electrical circuit ([75], [76]).

6.3.4.1 Example with static 2–D beam elements

In this section it is demonstrated how to build an electrical equivalent of a slender beam. The beam in itself may be discretized into a number of subsections, see fig. 6.10. The element formulation of an Euler-Bernoulli subsection is expressed analytically in eq. 6.1. Expressed by the equivalent electrical parameters in the $f \rightarrow V$ analogy it is:

$$
\begin{bmatrix} I_1 \\ I_2 \\ I_3 \\ I_4 \end{bmatrix} = \frac{1}{j\omega} \begin{bmatrix} \frac{12EI}{L^3} & \frac{6EI}{L^2} & -\frac{12EI}{L^3} & \frac{6EI}{L^2} \\ \frac{6EI}{L^2} & \frac{4EI}{L} & -\frac{6EI}{L^2} & \frac{2EI}{L} \\ -\frac{12EI}{L^3} & -\frac{6EI}{L^2} & \frac{12EI}{L^3} & -\frac{6EI}{L^2} \\ \frac{6EI}{L^2} & \frac{2EI}{L} & -\frac{6EI}{L^2} & \frac{4EI}{L} \end{bmatrix} \begin{bmatrix} V_1 \\ V_2 \\ V_3 \\ V_4 \end{bmatrix}
$$

Assuming the circuit in fig. 6.11, it is noted that the admittance matrix ex-
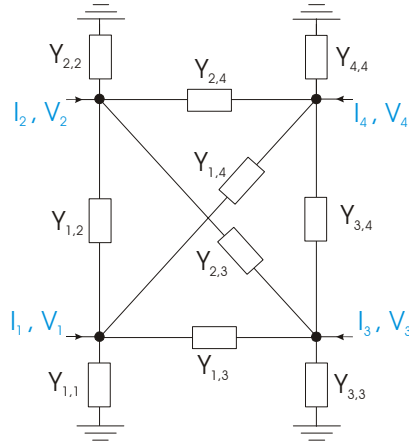
Figure 6.11: The electrical equivalent of a 2-d Euler-Bernoulli beam element in the $f \to V$ convention.

pressed in terms of the admittances are:

$$
\begin{bmatrix} I_1 \\ I_2 \\ I_3 \\ I_4 \end{bmatrix} = \begin{bmatrix} \sum Y_{1,j} & -Y_{1,2} & -Y_{1,3} & -Y_{1,4} \\ -Y_{2,1} & \sum Y_{2,j} & -Y_{2,3} & -Y_{2,4} \\ -Y_{3,1} & -Y_{3,2} & \sum Y_{3,j} & -Y_{3,4} \\ -Y_{4,1} & -Y_{4,2} & -Y_{4,3} & \sum_j Y_{4,j} \end{bmatrix} \begin{bmatrix} V_1 \\ V_2 \\ V_3 \\ V_4 \end{bmatrix}
$$

From this it can be seen that:

$$
Y_{i,i} = \sum_j \frac{1}{j\omega} K_{i,j}
$$

$$
Y_{i,j} = -\frac{1}{j\omega} K_{i,j} \qquad i \neq j
$$

The values of the inductances may be negative. So far we have obtained the electrical equivalent for the static problem of the single beam element.

The second stage is to connect two elements, forming a longer beam (one could simply change the length of the beam element instead, but that would not demonstrate the principle we want to show). For simplicity, the elements are assumed to be identical. The procedure mentioned above, namely adding the admittance values at the correct nodes, is followed. This is equivalent to connecting the subcircuits at the proper nodes, see fig. 6.12.The subcircuits are clearly recognized.

6.3.4.2 The case of a dynamic system

In the above, the system was assumed to be static. A further developement of the tool is to allow for dynamic models. Recall that the equivalent of the stiffness and mass matrices is the admittance matrix. Hence the admittance

93
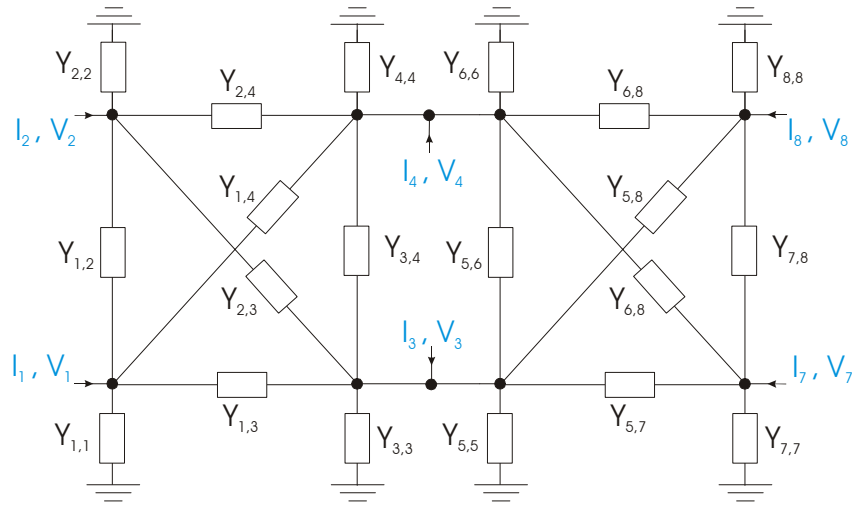
Figure 6.12: The equivalent circuit of two beam elements connected. The nodes 3 and 4 are connected with nodes 5 and 6 respectively. $(f \to V$ convention)
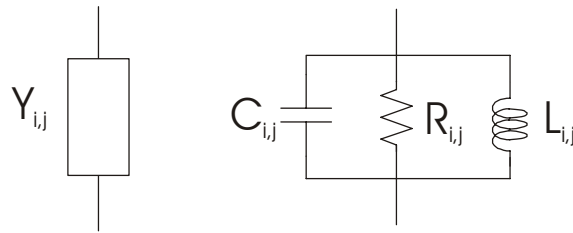
Figure 6.13: Equivalent circuit when stiffness, damping, and inertial effects are included. $(f \to V$ convention)

matrix must be equivalent to the sum of the stiffness, the damping, and the mass matrices:

$$Y_{i,i} = \sum_j \left(\frac{1}{j\omega} K_{i,j} + B_{i,j} + j\omega M_{i,j} \right)$$

$$Y_{i,j} = -\frac{1}{j\omega} K_{i,j} - B_{i,j} - j\omega M_{i,j} \qquad i \neq j$$

Elements with such an admittance is simply an inductor, a resistor and a capacitor in parallel, see fig. 6.13. This proves to be a convenient property, since it means that the equivalent static model (inductances) can be constructed first, and then the dynamic effects (resistors and capacitances) can be included by simply placing the elements in parallel to the inductances.

Above, the creation of electrical equivalent models of linear FEM-models

have been presented. The question of external forcing has been indirectly answered by the introduction of the current injection at the electrical nodes.

6.3.5 Conclusions and discussion on electrical equivalents

Both the $f \to V$ analogy and the $e \to V$ have now been presented. Both methods prove to be able to replicate mechanical systems described in terms of stiffness, damping and mass matrices. The two analogies obviously result in very different electrical equivalents. From the above, it can be concluded that in the $f \to V$ analogy there is a 1 to 1 mapping of mechanical elements and variables into electrical equivalents. This is generally not true in the $e \to V$ convention, making the system less transparent in terms of seeing the relation between the electrical equivalent and the mechanical system. Also the way external forces are applied to the electrical equivalent in the $e \to V$ analogy appears more complicated and less transparent than in the $f \to V$ analogy.

There is a discussion of choice of analogy in [75], where the relation between electrical and mechanical switches is shown to be perfectly natural in the $f \to V$ analogy. The $e \to V$ analogy, on the other hand, gives a much less logical relation. For example, on/off states in a mechanical switch is represented by the opposite states in the equivalent electrical switch.

The case of having nonlinear effects present is also of importance. Nonlinear effects are most often described either as a black-box model, where the FEM-matrices are generated iteratively, or as an analytical formulation. In the former case, the circuit must be regenerated each single time for the piecewise linearized model and no advantage of one analogy over the other appears to exists. In the latter case, the nonlinearity is known a priori, and may be directly implemented. The analytical description of the nonlinear element is often based on the nonlinear relation between the nodes of an element. For the case of the $f \to V$ analogy, the implementation can be done directly, but in the case of utilizing the $e \to V$ analogy, the nonlinearity may have to be reformulated to fit the available states in the circuit constructed. This is analogous to the implementation of m_1 in example 2 in section 6.3.3.2 regarding $e \to V$ analogy.

As shown, the $e \to V$ analogy is generally inferior to the $f \to V$ analogy. The drawbacks can, however, for certain types of systems be diminshed. E.g. can some mechanical systems be expressed in the eigenspace with diagonal stiffness, damping, and mass matrices. For such systems, the drawbacks associated with large connectivity are removed.

6.4 Electrostatic transducers

6.4.1 A transducer element

Many types of transducer elements and their electrical equivalent structures
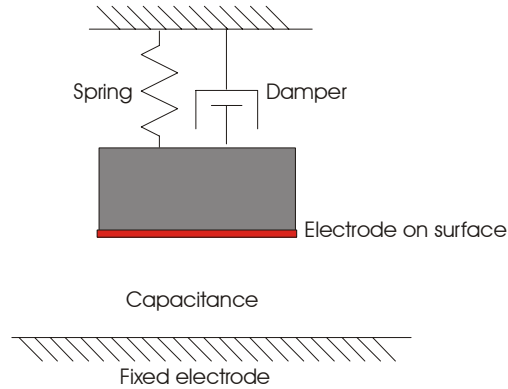
Figure 6.14: A transducer-element including mass and damper elements. Note that positive direction for force and displacement is upwards.

have been discussed in the literature, see e.g. [67] and references therein. However, older publications tend to not consider the electrostatic transducers.

In the MEMS-world, however, the electrostatic transducer is a key element, being used for excitation of mechanical elements and for electrical read-out of mechanical states ([77],[78],[36]). An important property of electrostatic transducer elements is their nonlinearity. This is obviously a complicating matter for both modelling and utilization of these transducers. A simple transverse electrostatic transducer element, including mass and damper elements, is shown in fig. 6.14.

To develope the governing equations for such a system, it is convinient to look at the energy conserved in such a system:

$$E = \frac{1}{2}kx^2 + \frac{q^2(d+x)}{2\varepsilon_0 A_e} + \frac{1}{2}mv^2$$

where A_e is area of capacitance, q is charge and d is initial height of gap between the electrodes with the spring relaxed. The displacement of the upper electrode is given by x, while the velocity is v. Spring stiffness and mass is given by k and m. From the energy expression, the relations between force, voltage, current, and displacement can be developed.

6.4.2 $e \rightarrow V$ analogy

The $e \rightarrow V$ analogy of electrostatic transducers have been thoroughly investigated to create equivalent circuits in i.e. [77], [78]. The equivalent circuit of the system shown in fig. 6.14 is presented in fig. 6.15 (taken from [77]).Note that the equivalent circuit is linearised around a bias-point. The variables are:
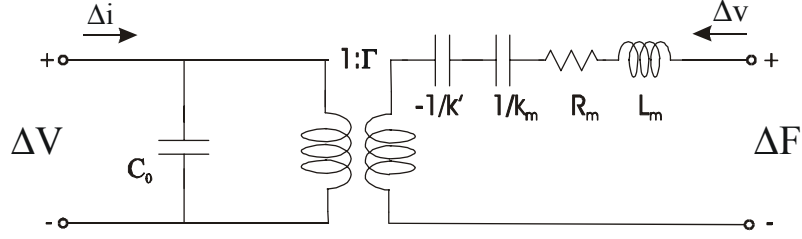
Figure 6.15: The $e \rightarrow V$ equivalent circuit of the system shown in 6.14. The left side of the transformer is the electrical input, while the right side is the electrical analogy of the mechanics. (Taken from [77])

$$
\begin{aligned}
C_0 &= \frac{Q_0}{V_0} = \frac{\varepsilon_0 A_0}{d + x_0} \\
\Gamma &= \frac{Q_0}{x_0} = \frac{\varepsilon_0 A_0 V_0}{(d + x_0)^2} \\
k' &= \kappa^2 k = \frac{\Gamma^2}{C_0} = \frac{\varepsilon_0 A_0 V_0^2}{(d + x_0)^3} \\
k^* &= k_m - k' \\
k_m &= \text{- spring stiffness} \\
R_m &= \text{- viscous damping} \\
L_m &= \text{- mass} \\
v &= \text{- velocity} \\
d &= \text{- gap} \\
x_0 &= \text{-displacement of spring at } V_0
\end{aligned}
$$

We note the amplitude dependency (nonlinearity) of the parameters. The $[ABCD]$-matrix is:

$$
\begin{aligned}
[ABCD] &= \begin{bmatrix} 1 & 0 \\ i\omega C_0 & 1 \end{bmatrix} \begin{bmatrix} \frac{1}{\Gamma} & 0 \\ 0 & \Gamma \end{bmatrix} \begin{bmatrix} 1 & \left(\frac{k^*}{i\omega} + R_m + i\omega L_m\right) \\ 0 & 1 \end{bmatrix} \\
[ABCD] &= \begin{bmatrix} \frac{1}{\Gamma} & \frac{1}{\Gamma}\left(\frac{k^*}{i\omega} + R_m + i\omega L_m\right) \\ i\omega\frac{C_0}{\Gamma} & i\omega\frac{C_0}{\Gamma}\left(\frac{k^*}{i\omega} + R_m + i\omega L_m\right) + \Gamma \end{bmatrix} \\
[ABCD] &= \begin{bmatrix} \frac{1}{\Gamma} & \frac{1}{\Gamma}\left(\frac{k^*}{i\omega} + R_m + i\omega L_m\right) \\ i\omega\frac{C_0}{\Gamma} & i\omega\frac{C_0}{\Gamma}\left(\frac{k_m}{i\omega} + R_m + i\omega L_m\right) \end{bmatrix}
\end{aligned} \tag{6.2}
$$

As seen in the example it is rather straight forward to construct this equivalent circuit for a system with 1 mechanical degree of freedom. More often, the systems are distributed, and a number of mechanical d.o.f.'s may be influenced

97
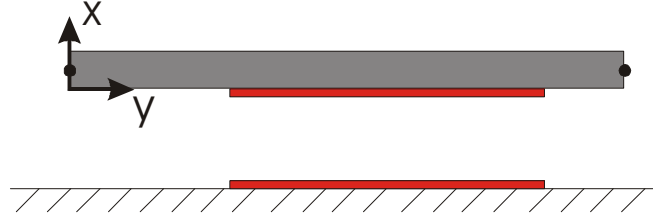
Figure 6.16: A beam with a capacitor placed arbitrarily underneath. The ccapacitors are marked in red. Boundary-conditions for the beam are not included in the schematic, and can be chosen freely.

by the capacitor.

6.4.3 Distributed-parameter system for a beam

In [78], a distributed-parameter system is presented for the case of a single-sided fixed beam with an electrode covering the length of the beam. The mechanical system is represented in terms of eigenvectors, which makes the construction of the equivalent circuit of the mechanical system easier (since the $e \rightarrow V$ convention is assumed).

The equations given in [78] can be slightly modified to allow for the more general case of a uniform beam with shorter electrodes placed at an arbitrary position along the beam, see fig. 6.16.

The developement of the equations need to be done in a correct manner. A good starting point is to look at the electrical energy stored in each infinitesimal transducer element ($U_{s,e}$ is the energy density per area, while dA_n is the infinitesimal electrode area. Surface charge density is given by σ, and x is change in gap due to deformation of beam):

$$U_{s,e} = \frac{1}{2} \frac{\left(\sigma\left(y,z\right)\right)^2}{\frac{\varepsilon_0}{d+x(y)}}$$

$$W_e = \sum_j U_{s,e,j} dA_j = \sum_j \frac{1}{2} \frac{\left(\sigma_j\right)^2}{\frac{\varepsilon_0}{d+x_{j,0}}} dA_j$$

Clearly, this is an analytical approximation that does not include fringing fields. From the energy expression, we can find the potential and force:

$$V\left(y,z\right) = \frac{d}{d\sigma} \left(\frac{1}{2} \frac{\left(\sigma\left(y,z\right)\right)^2}{\frac{\varepsilon_0}{d+x(y)}}\right)_{w=\text{constant}} = \frac{\sigma\left(y,z\right)}{\frac{\varepsilon_0}{d+x(y)}}$$

$$F_{density}\left(y,z\right) = \frac{d}{dx} \left(\frac{1}{2} \frac{\left(\sigma\left(y,z\right)\right)^2}{\frac{\varepsilon_0}{d+x(y)}}\right)_{\sigma=\text{constant}} = \frac{\left(\sigma\left(y,z\right)\right)^2}{2\varepsilon_0}$$

Assuming that the operation is small around a bias point, it follows:

$$\Delta V\left(y\right) = \frac{dV}{d\sigma}\Delta\sigma + \frac{dV}{dx}\Delta x = \frac{d + x_0}{\varepsilon_0}\Delta\sigma + \frac{V_0}{d + x_0}\Delta x$$

$$\Delta F_{density}\left(y\right) = \frac{dF_{density}}{d\sigma}\Delta\sigma + \frac{dF_{density}}{dx}\Delta x = \frac{V_0}{d + x_0}\Delta\sigma + 0\Delta x$$

For convinience, the position dependencies of the parameters have been ignored. With a perfect conductor, the potential will be constant and the equations may be simplified:

$$\Delta V\left(y\right) = \frac{d + x_0\left(y\right)}{\varepsilon_0}\Delta\sigma\left(y\right) + \frac{V_0}{d + x_0\left(y\right)}\Delta x\left(y\right)$$

$$\Delta F_{density}\left(y\right) = \frac{V_0}{d + x_0\left(y\right)}\Delta\sigma\left(y\right)$$

Next stage now, is to discretize the equations, giving:

$$\Delta V_j = \frac{d + x_{j,0}}{\varepsilon_0}\Delta\sigma_j + \frac{V_0}{d + x_{j,0}}\Delta x_j \tag{6.4a}$$

$$\Delta F_j = \frac{V_0}{d + x_{j,0}}\Delta\sigma_j \tag{6.4b}$$

$$\begin{bmatrix} \Delta V_1 \\ \vdots \\ \Delta V_N \\ \Delta F_1 \\ \vdots \\ \Delta F_N \end{bmatrix} = \begin{bmatrix} B_1 & 0 & 0 & C_1 & 0 & 0 \\ 0 & \ddots & 0 & 0 & \ddots & 0 \\ 0 & 0 & B_N & 0 & 0 & C_N \\ A_1 & 0 & 0 & 0 & & 0 \\ 0 & \ddots & 0 & & & \\ 0 & 0 & A_N & 0 & & 0 \end{bmatrix} \begin{bmatrix} \Delta\sigma_1 \\ \vdots \\ \Delta\sigma_N \\ \Delta x_1 \\ \vdots \\ \Delta x_N \end{bmatrix} \tag{6.4c}$$

With the latter sub-equation in mind (eq. 6.4c), we may impose the assumption of a perfect conductor. Such an added assumption gives a strong relation between the voltage, the distributed surface charge, the distributed force, and the deformation.

To be able to construct the exact equivalent circuit, the bias-point around which the system is linearised must be found. This is done by solving the full nonlinear system at the given voltage (or charge).

Continuing to focus on the $e \rightarrow V$ convention, we are now ready to create the full equivalent circuit with the discretized description of the transducer. In the previous discussions, problems encountered in constructing equivalent circuits in the $e \rightarrow V$ convention of arbitrary mechanical systems were emphasized. Very often, the best choice would be to represent the mechanical system in the eigenspace, and not the original k-space of the system. Nonetheless, consideration should be given to the modelling of the transducer when the mechanical system is represented in the k-space. Eq. 6.4c appears to be

similar to a number of unconnected transducer elements. However, with the assumption of a perfect conductor, the transducer elements may be connected to have the same voltage. This means that the equivalent circuit may be constructed as given in fig. 6.17 (the equivalent circuit of the mechanical part has been omitted for simplicity, since the electrical equivalent of the mechanical system in the $e \rightarrow V$ analogy is not obvious). The parameters are given as:

$$
\begin{aligned}
C_0 &\approx \int_{A_{electrode}} \frac{\varepsilon_0}{d + \bar{x}_0} dA \quad \bar{x}_0\text{-average displacement over electrode} \\
\Gamma_j &= \int_{A_{electrode\,j}} \frac{\varepsilon_0 V_0}{(d + x_{0,j})^2} dA_j \\
k'_j &= \frac{V_0^2 \varepsilon_0}{(d + x_{j,0})^3}
\end{aligned}
$$

Another alternative in creating the equivalent circuit is to represent the mechanical system in the eigenspace. The advantage of this is that the mechanical system will become a set of uncoupled ordinary differential equations, hence it is very easy to create an equivalent circuit of the mechanical system. Looking only at the capacitance and the transformer, i.e. disregarding the mechanical system and the electrostatic spring effect, it holds :

$$
\left[\begin{array}{c} \Delta V \\ \Delta I \end{array} \right] = \left[\begin{array}{cc} \left[\frac{1}{\Gamma}\right] & [0] \\ \left[i\omega\frac{C_0}{\Gamma}\right] & [-\Gamma] \end{array} \right] \left[\begin{array}{c} \Delta F_{transformer} \\ \Delta x_{transformer} \end{array} \right]
$$

For the distributed system, the variables $\Delta V, I, \Delta F_{transformer}$, and $x_{transformer}$ are obviously vectors, while the elements $\left[\frac{1}{\Gamma}\right]$, $\left[\frac{C_0}{\Gamma}\right]$, and $[-\Gamma]$ are diagonal matrices. The goal is now to diagonalize the mechanical system by transforming it into the eigenspace. In doing so, the electrostatic spring effect must be included. The eigenvectors can be found by solving the eigenproblem of the equation:

$$
[M][\ddot{x}] + ([K] + [K_{es}])[x] = [0]
$$

where $[K_{es}]$ resembles the electrostatic spring effect. With the eigenvectors, $[Q]$, at hand, the transformation of the governing equation is done:

$$
\begin{aligned}
\left[\begin{array}{c} \Delta V \\ \Delta I \end{array} \right] &= \left[\begin{array}{cc} \left[\frac{1}{\Gamma}\right] & [0] \\ \left[i\omega\frac{C_0}{\Gamma}\right] & [-\Gamma] \end{array} \right] \left[\begin{array}{cc} [Q] & [0] \\ [0] & [Q] \end{array} \right] \left[\begin{array}{c} \Delta F^q_{transformer} \\ \Delta x^q_{transformer} \end{array} \right] \\
&= \left[\begin{array}{cc} \left[\frac{1}{\Gamma}\right][Q] & [0] \\ \left[i\omega\frac{C_0}{\Gamma}\right][Q] & [-\Gamma][Q] \end{array} \right] \left[\begin{array}{c} \Delta F^q_{transformer} \\ \Delta x^q_{transformer} \end{array} \right]
\end{aligned}
$$

And from the latter it is clear that the submatrices $\left[\frac{1}{\Gamma}\right][Q]$, $\left[i\omega\frac{C_0}{\Gamma}\right][Q]$, and $[-\Gamma][Q]$ are no longer diagonal (except in special cases). This means that the transducer elements can no longer be described in the simple manner
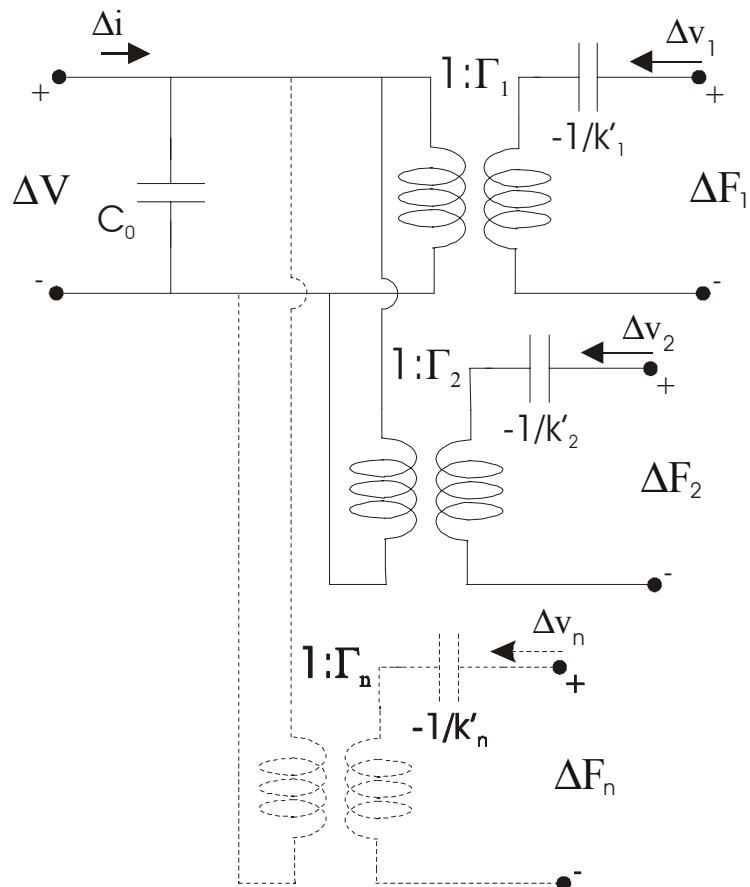
Figure 6.17: An equivalent circuit of the electrostatic transducer. This figure assumes that the mechanical part is represented in its k-space and modeled in the $e \rightarrow V$ convention. ($v_j = \dot{x}_j$).

depicted in fig. 6.17. A more complex topology of the transducer elements linking the voltages and charges with the displacement and forces defined in the eigenspace must be created. This can be examplified by applying a force in a single d.o.f. (defined in the eigenspace) implies that energy may be transmitted through a number of capacitors. This is in contrast to a system where the mechanics is represented in the k-space, where applying a force on a single node only interfere with a single capacitor.

6.4.4 $f \rightarrow V$ analogy

We have earlier discussed the differences between the $f \rightarrow V$ analogy and the $e \rightarrow V$ analogy in section 6.3, where we noted the clear advantages of using the $f \rightarrow V$ analogy. The importance of having an equivalent circuit for the electrostatic transducer for the mobility analogy is therefore unquestionable. In this section we develope such an equivalent circuit. From eq. 6.2, we have the $[ABCD]$-matrix for the $e \rightarrow V$ analogy. A simple interchange of variables, and disregarding damping and inertia, leads to :

$$
\begin{bmatrix} \Delta V \\ \Delta I \end{bmatrix} = \begin{bmatrix} \frac{1}{\Gamma} & \frac{1}{\Gamma}\frac{k^*}{i\omega} \\ i\omega\frac{C_0}{\Gamma} & i\omega\frac{C_0}{\Gamma}\frac{k^*}{i\omega} + \Gamma \end{bmatrix} \begin{bmatrix} \Delta F \\ -\Delta u \end{bmatrix} \quad \text{direct analogy}
$$

$$
\begin{bmatrix} \Delta V \\ \Delta I \end{bmatrix} = \begin{bmatrix} -\frac{k^*}{i\omega\Gamma} & -\frac{1}{\Gamma} \\ -\frac{C_0}{\Gamma}k^* - \Gamma & -i\omega\frac{C_0}{\Gamma} \end{bmatrix} \begin{bmatrix} \Delta u \\ -\Delta F \end{bmatrix} \quad \text{mobility analogy}
$$

This $[ABCD]$-matrix may be expressed in terms of three simpler $[ABCD]$-matrices in cascade. Refering to the multiplicative properties of the $[ABCD]$-matrices, we see that:

$$ [ABCD_{total}] = [ABCD_1][ABCD_2]\dots[ABCD_N] $$

And hence the full $[ABCD]$-matrix can be decomposed into three cascaded $[ABCD]$-matrices:

$$
\begin{bmatrix} \Delta V \\ \Delta I \end{bmatrix} = \begin{bmatrix} -\frac{k^*}{i\omega\Gamma} & -\frac{1}{\Gamma} \\ -\frac{C_0}{\Gamma}k^* - \Gamma & -i\omega\frac{C_0}{\Gamma} \end{bmatrix} \begin{bmatrix} \Delta u \\ -\Delta F \end{bmatrix}
$$

$$
= \begin{bmatrix} 1 & 0 \\ i\omega C_0 & 1 \end{bmatrix} \begin{bmatrix} 0 & -\frac{1}{\Gamma} \\ -\Gamma & 0 \end{bmatrix} \begin{bmatrix} 1 & 0 \\ \frac{1}{i\omega}k^* & 1 \end{bmatrix} \begin{bmatrix} \Delta u \\ -\Delta F \end{bmatrix}
$$

This decomposition gives us the circuit in fig. 6.18.

6.4.4.1 Distributed transducers

As in the previous section 6.4.3, we expand the single d.o.f. system to a NDOF-system. The same methodology as was used for the $e \rightarrow V$ analogy, can be applied here.The results are similar, hence there is generally no way of decoupling the mechanical system and still keep the topology as indicated by fig. 6.19. However, the reasons for decoupling the mechanical system is
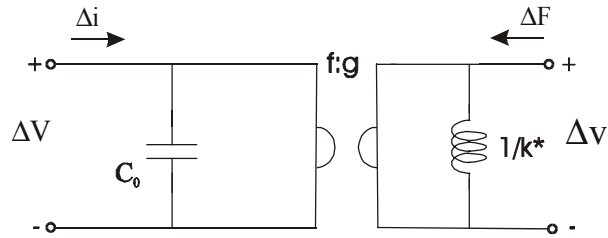
Figure 6.18: The equivalent circuit of the transverse electrostatic transducer. The mechanical spring is included.
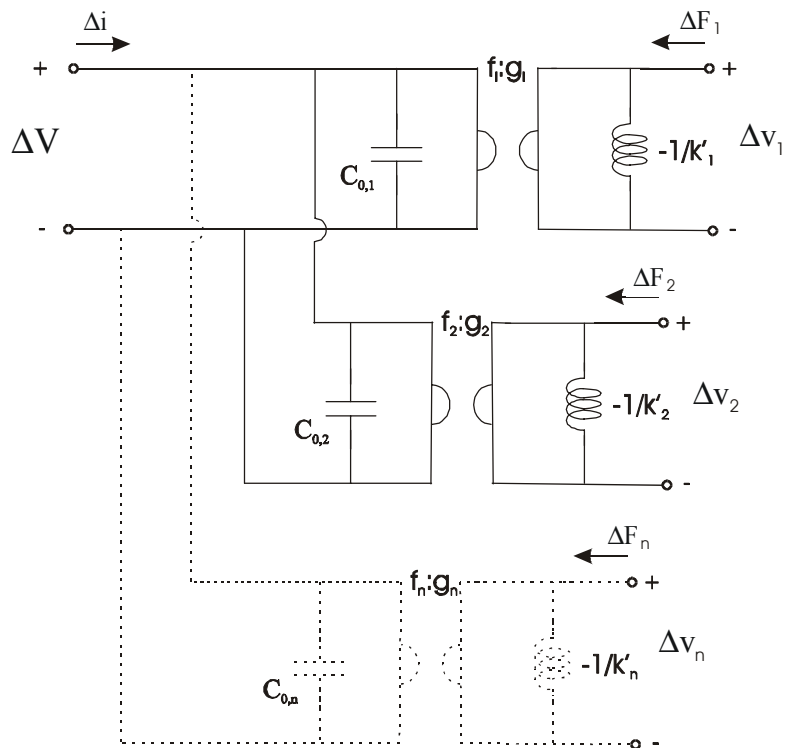

Figure 6.19: Equivalent circuit of a distributed transducer-element in the $f \rightarrow V$ analogy

103

not as accentuated in the $f \to V$ analogy as it is in the $e \to V$ analogy. For reasons of transparency and understanding, a decoupling of the mechanical system may in many situations still be very advantageous. This can obviously be done, but as indicated earlier when discussing the $e \to V$ analogy, at the cost of introducing more complex transducer circuitry. Transparency of the transducer element is best attained in the original k-space, since this only involves a number of simple gyrator elements.

6.4.5 Equivalent circuits without physical interpretation

In the literature there exists examples where the equivalent circuits have been further elaborated, to create simpler circuits. These circuits have, however, the drawback that physical interpretation of the parameters and (internal) states no longer exists (see e.g. [68]). Since a main objective of this work is to maintain and increase the understanding of system behaviour via modelling no further attention is given to such circuits.

6.4.6 Transducer elements with numerically calculated fields

In the above, we demonstrated how to build transducer elements based on analytical approximations of the total energy and the electric field. This method has obvious drawbacks, due to the inherent inaccuracies of the analytical approximations. To overcome this, the electrostatic problems may be solved numerically, e.g. using the boundary element methods. Results from these simulations may then be used directly to obtain the various parameters in the electrical equivalent. Another possibility is to use the numerical results in combination with the analytical results, i.e. adjusting the analytical results to fit with the numerical results, but still keep the parameter dependencies.

Here, basic equations regarding electrostatics and energy are presented and elaborated on to match the context in which it is used. A natural starting point is the energy contained in a set of capacitances:

$$W = \sum_{i,j} V_i C_{i,j} V_j$$

where we have that $[C]$ is the capacitance matrix. From the energy we can find the charge and the forces on each conductor:

$$Q_i = \frac{dW}{dV_i}_{|x=\text{constant}} = \left(\sum_j \left(C_{i,j} + C_{j,i} \right) V_j \right) - C_{i,i} V_i$$

$$F_i = \frac{dW}{dx_i}_{|V=\text{constant}} = \sum_{k,j} \left(\frac{d}{dx_i} C_{k,j} \right) V_k V_j - \sum_k \left(\frac{d}{dx_i} C_{k,k} \right) \frac{1}{2} V_k^2$$

With the equations for the charges and forces available, we may do a linearization of the equations, obtaining the relations for the linearized transducer

104

element:

$$\Delta Q\left(x\right) \;\; = \;\; \frac{dQ}{dV}\Delta V + \frac{dQ}{dw}\Delta x$$

$$\Delta F\left(x,z\right) \;\; = \;\; \frac{dF}{dV}\Delta V + \frac{dF_{density}}{dw}\Delta x$$

$$[\Delta Q] \;\; = \;\; [a]\left[\Delta V\right] + [b]\left[\Delta x\right]$$

$$[\Delta F] \;\; = \;\; [c]\left[\Delta V\right] + [d]\left[\Delta x\right]$$

To find the derivatives (or the matrices $[a]$, $[b]$, $[c]$, and $[d]$), we use the above equations and get:

$$\frac{dQ_i}{dV_m} \;\; = \;\; C0_{i,m} + C0_{m,i} - C0_{m,m}$$

$$\frac{dQ_i}{dx_m} \;\; = \;\; \sum_j \left(\frac{d}{dx0_m}\left(C0_{i,j} + C0_{j,i}\right) \right) V0_j - \left(\frac{d}{dx0_m}C0_{i,i} \right) V0_i$$

$$\frac{dF_i}{dV_m} \;\; = \;\; \sum_k \left(\frac{d}{dx0_i}C0_{k,m} + \frac{d}{dx0_i}C0_{m,k} \right) V_k - \left(\frac{d}{dx0_i}C0_{m,m} \right) V0_m$$

$$\frac{dF_i}{dx_m} \;\; = \;\; \sum_{k,j} \left(\frac{d^2}{dx0_i dx0_m}C0_{k,j} \right) V0_k V0_j - \sum_k \left(\frac{d^2}{dx0_i dx0_m}C0_{k,k} \right) \frac{1}{2}V0_k^2$$

where the zeros indicate the bias point ($C0$, $V0$, $x0$). Furthermore, we also recall the importance of the $[ABCD]$-matrix, and we may formulate the n-port matrix:

$$\left[\begin{array}{c} [\Delta Q] \\ [\Delta F] \end{array} \right] \;\; = \;\; \left[\begin{array}{cc} [a] & [b] \\ [c] & [d] \end{array} \right] \left[\begin{array}{c} [\Delta V] \\ [\Delta x] \end{array} \right]$$

$$\left[\begin{array}{c} [\Delta V] \\ [\Delta Q] \end{array} \right] \;\; = \;\; \left[\begin{array}{cc} [c]^{-1} & -[c]^{-1}[d] \\ [a][c]^{-1} & [b] - [a][c]^{-1}[d] \end{array} \right] \left[\begin{array}{c} [\Delta F] \\ -[\Delta x] \end{array} \right]$$

6.5   Boundary element method and parasitic capacitances

We have earlier argued for using lumped models, or finite element models for modelling mechanical structures, since such structures often tend to be too complex to model analytically. Likewise does electrostatic problems tend to be difficult to accurately model analytically. Just like the mechanical problem, the electrostatic problem can be solved by the finite element method. However, this is not a very efficient way of solving the electrostatic problem, since the whole volume must be divided into elements, and a solution for every element must be found. Another method, the boundary element method (BEM), does not use volume elements, but boundary elements. That is, conducting surfaces and interface surfaces are meshed (as surface). From this, equations relating voltage and surface charges on the various surfaces

105

are set up. Hence a more compact model, with less superfluous information, is created. A drawback, although seldomly of importance, is that the electric field distribution over the volume is not directly at hand. The field distribution can be calculated on the basis of the voltages and charges on the surfaces, if needed. In this work, the most useful property of the BEM, is the compact and accurate description of relations between charge and voltage on the surfaces.

We have implemented a very simple program that solves 2-D electrostatic problems by means of the boundary element method. Without going into much detail, we will briefly present some fundamental aspects of the boundary element method related to the electrostatic problem. The electrostatic problem is governed by the Laplace-equation:

$$\bigtriangledown^2 \phi = 0$$

where ϕ is the potential. This equation can be reformulated to Fredholm's equations of the first and second kind [79]. These equations then become the basis of the boundary element formulation. The Fredholm equation of the first kind governs the behaviour in a volume of constant permittivity, while Fredholm's equation of the second kind ensures that continuity is preserved over dielectric boundaries. The discretization of the Fredholm equations gives us the means to calculate the elements in the BE-matrix. Hence the Fredholm equations define the relation between charges and voltages on given surfaces, lines or points.

Fredholm's equations can be discretized in various manners. A Galerkin-method attempts to satsify the boundary conditions over the surface [79]. An alternative is the "charge collocation"-method which satisfies the boundary conditions at a discrete number of points. The latter method is inferior to the Galerkin-method [79], but nevertheless we chose to use it, due to simpler implementation. The governing system of equations for an electrostatic system described by the boundary element method appears as:

$$\begin{bmatrix} A_{1,1} & A_{1,2} \\ A_{2,1} & A_{2,2} \end{bmatrix} \begin{bmatrix} \rho_{\text{charge}} \\ \rho_{\text{interface}} \end{bmatrix} = \begin{bmatrix} V_{\text{charge}} \\ 0 \end{bmatrix}$$

Here V_{boundary} is a vector consisting of the voltages on the boundary-elements. ρ_{charge} is the corresponding surface charges on the elements. $\rho_{\text{interface}}$ is the charges on the dielectric interfaces.

6.6   Modelling and simulations of the microfilter

In this section, we create models of the microfilter with varying number of degrees of freedom. From the smallest models, the operational principle can easily be understood, whereas the larger models gives a more accurate picture of the real system behaviour. Models are created in the order that the smallest and simplest models are created first, whereas the more complex are created

106

afterwards. Simulation results are presented and the results are discussed, with a special focus on accuracy versus model size.

In the below, we present the parameter values used for the system-simulations:

$L_{beam\_1} = 50\mu m$	Length of main beam 1
$L_{beam\_2} = 50\mu m$	Length of main beam 2
$W_{beam} = 10\mu m$	Width of main beams
$T_{beam} = 2\mu m$	Thickness of main beams
$L_{couple} = 20\mu m$	Length of coupling beam
$W_{couple} = 3\mu m$	Width of coupling beam
$T_{couple} = 2\mu m$	Thickness of coupling beam
$\rho = 2.329 \cdot 10^3 \frac{kg}{m^3}$	Density of main beam
$E = 1.6 \cdot 10^{11} Pa$	Young's modulus
$d = 2\mu m$	Electrode gap
$L_{cap} = 30\mu m$	Length of electrode
$W_{cap} = 10\mu m$	Width of electrode
$\varepsilon = 8.854 \cdot 10^{-12} \frac{F}{m}$	Permittivity of vacuum

6.6.1 A 2-d.o.f. model of the microfilter

The starting point for us is to identify a model as small as possible. We will in the forthcoming do this, describing the process, ending up with a simple model capturing the main characteristics of the real system.

Referring to fig. 6.1, showing the microfilter, three important mechanical objects are identified, namely the two main beams and the coupling beam. While each beam truely contains an infinite number of degrees of freedom (with the continuum assumption), the models of each beam can be simplified to contain a finite number of d.o.f.'s.

Looking at the to main beams, they are fixed at the end-points, while the coupling beam is connected at a point along the beam. For the simulations here, we assume the coupling beam is connected at the centre (hence not equivalent with fig. 6.1). We also note that the capacitances are centred. The electrostatic forces from the capacitances may therefore be approximated to be attacking at the centre point. With all forcing attacking at the centre point, the deformation will in large be described by a sinusoidal curve, equivalent to the lowest eigenfrequency mode. Therefore, we choose the lowest eigenfrequency mode as the only degree of freedom to model the deformation of each of the main beams, see fig. 6.20. Each main beam is therefore modelled by a single stiffness and a single mass.

The coupling beam is connected to the main beams at each end-point. These are also the only points that are controllable and observable. Therefore, we are only interested in the link between force and deformation of the end-points, where possible deformation of the end-points are defined by possible deformation-shapes of the main beams. This gives us a stiffness and a mass

Figure 6.20: The solid line symbolizes the undeformed main beam. The dotted line shows the lowest eigenfrequency mode, which is used in the 2-d.o.f. model.

that arises from the coupling beam. We will, however, assume the mass of the coupling beam to be insignificant to the system behaviour, and therefore disregard it.

Each of the two main beams have their respective (uncoupled) eigenfrequencies at $\omega_1 = \sqrt{\frac{k_1}{M_1}}$ and $\omega_2 = \sqrt{\frac{k_2}{M_2}}$. Further details of the equations used, are given as:

$$
\begin{aligned}
\omega_{beam} &\cong 4.7^2 \sqrt{\frac{EI}{\rho A L^4}} \\
k_{beam} &\cong \frac{423}{1.68} \frac{EI}{L^3} \\
m_{beam} &\cong \frac{0.845}{1.68} \cdot \rho A L \\
k_{couple} &= 12 \frac{EI}{L^3}
\end{aligned}
$$

Here, I is second moment of area, A is cross-sectional area, and L is length of beam. These equations are consequences of the earlier made assumptions applied to the Euler-Bernoulli beam theory.

The system described above can be shown schematically. This is done in fig. 6.21, where also the electrical equivalent of the model is shown (in the $f \rightarrow V$ analogy). Furthermore, the system can be described in terms of a
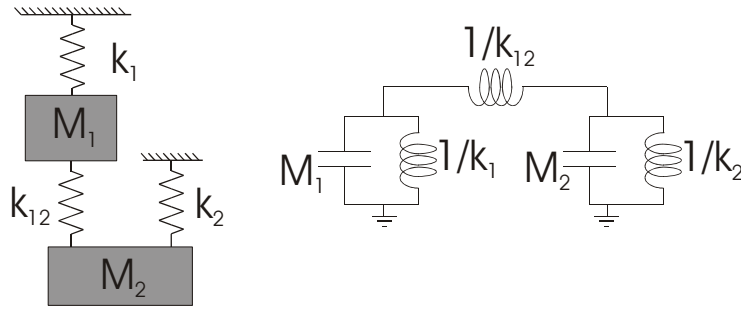
Figure 6.21: A 2-dof mechanical system and its electrical analogy ($f \rightarrow V$). The values should be so that $\omega_1 = \sqrt{\frac{k_1}{M_1}}$ and $\omega_2 = \sqrt{\frac{k_2}{M_2}}$

state-space description:

$$
\begin{bmatrix} \dot{x}_1 \\ \dot{x}_2 \\ \ddot{x}_1 \\ \ddot{x}_2 \end{bmatrix} = \begin{bmatrix} 0 & 0 & 1 & 0 \\ 0 & 0 & 0 & 1 \\ -\omega_1^2 - \frac{k_{couple}}{m_1} & \frac{k_{couple}}{m_1} & 0 & 0 \\ \frac{k_{couple}}{m_2} & -\omega_2^2 - \frac{k_{couple}}{m_2} & 0 & 0 \end{bmatrix} \begin{bmatrix} x_1 \\ x_2 \\ \dot{x}_1 \\ \dot{x}_2 \end{bmatrix} \tag{6.5}
$$

$$
+ \begin{bmatrix} 0 \\ 0 \\ \frac{1}{m_1} \\ 0 \end{bmatrix} f(t)
$$

$$
y = \begin{bmatrix} 0 & 1 & 0 & 0 \end{bmatrix} \begin{bmatrix} x_1 \\ x_2 \\ \dot{x}_1 \\ \dot{x}_2 \end{bmatrix}
$$

Where $f(t)$ is the mechanical force excitation on the first main beam. y is equivalent to the maximum displacement of the second main beam. With the state-space description at hand, it is straight-forward to find the transfer-function for the system:

$$
\begin{aligned}
H(s) &= \frac{y(s)}{f(s)} \\
&= m_1 \frac{k_{couple}}{\left(\begin{array}{c} s^4 m_1 m_2 \\ +s^2 \left(m_1 k_{couple} + m_2 k_{couple} + m_1 m_2 \omega_1^2 + m_1 m_2 \omega_2^2 \right) \\ +m_1 m_2 \omega_1^2 \omega_2^2 + m_1 \omega_1^2 k_{couple} + m_2 \omega_2^2 k_{couple} \end{array} \right)} \\
&= \frac{k}{(s^2 + a^2)(s^2 + b^2)}
\end{aligned}
$$

109

- 2-dof mechanical system
- 1-dof mechanical system

Figure 6.22: Normalized plot of the transfer-function of the idealized purely mechanical 2-d.o.f. system. Also included are a plot of a similar system with only 1 d.o.f. (detection node and excitation node is equivalent for the 1-d.o.f. system)
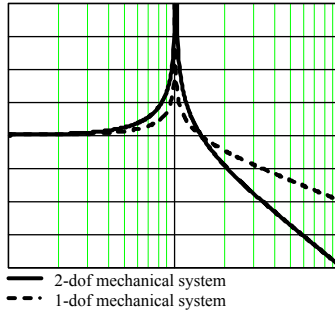
Here, the constants a, b, and k are functions of the properties of the beams. However, by assuming the coupling stiffness, k_{couple} to be small compared to the spring stiffness of the main beams, the transfer-function can be simplified:

$$H_{simple}(s) \cong \frac{k_{couple}}{m_2} \frac{1}{(s^2 + \omega_1^2)(s^2 + \omega_2^2)}$$

The transfer-function demonstrates the underlying principle of the filter. By trimming the eigenfrequencies to be as close as possible, we obtain a transfer-characteristic of a resonator, see fig. 6.22. Note that the plot is idealized in that the poles are at the same frequencies. In the same figure, we have also included the transfer-function of a system with only one main beam (and hence no second main beam or coupling beam, $H(s) = \frac{k}{(s^2 + \omega_1^2)}$). By investigating the two transfer-functions, it is seen that sharper fall-off after the peak can be obtained with systems with more degrees of freedom.

6.6.2 Electrical excitation and detection

The mechanical filter is meant to replace electrical components, and the input and output of the system should therefore be electrical. We use an electrostatic transducer to create the coupling between the mechanical and the electrical parts. For the excitation, we assume a voltage controlled system, and hence the mechanical forcing can be said to be proportional to the voltage (for simplicity we disregard nonlinearities at this stage). Obviously, excitation can also be done assuming a current-controlled system, however, the principal behaviour stays much the sames. How detection should be done is, on the other hand, quite important for system response. Here, two principal methods will be mentioned, which results in different transfer-functions. The first method is capacitive detection. The (detection) capacitance is dependent
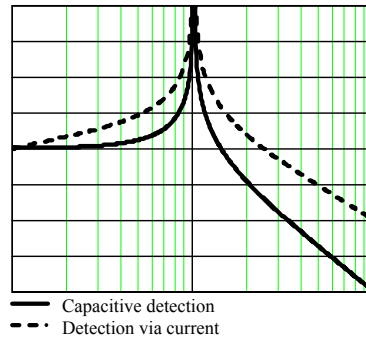
Capacitive detection
Detection via current

Figure 6.23: Normalized transfer-function plots of the 2-d.o.f. mechanical system, when capacitive detection and detection via current monitoring is employed.

upon gap, and thus one may simply monitor the change in capacitance, which is proportional to displacement (to first order). The other method relies upon the same effect, but instead of monitoring the capacitance value directly, the current that is generated by the (changing) capacitance is monitored. This assumes that a constant voltage is applied to the detection capacitance. The result is a current that is proportional to the velocity, and not the displacement of the detectional degree of freedom. The transfer-characteristics of the two methods are shown in fig. 6.23, and the transfer-functions becomes:

$$
\begin{aligned}
H_{cap}(s) &\propto \frac{x(s)}{f(s)} \cong \frac{k_{couple}}{m_2} \frac{1}{(s^2 + \omega_1^2)(s^2 + \omega_2^2)} \\
H_{current}(s) &\propto \frac{\dot{x}(s)}{f(s)} \cong \frac{k_{couple}}{m_2} \frac{s}{(s^2 + \omega_1^2)(s^2 + \omega_2^2)}
\end{aligned}
$$

A very convinient property of the nonlinear transducer element is that at small-signal values, there is a nonlinear effect that appears as addditional stiffness. This means that the transducer element can partly change the mechanical system's stiffness, hence the mechanical system's frequency response can be tuned electrically.

6.6.3 2-d.o.f. model with electrical excitation and detection

The 2-d.o.f. model presented above, only includes the mechanical domain, where excitation is force and detection is displacement. Clearly, we would prefer a model that has an electrical input and output. This can be done by including the capacitances into the model. This is done by introducing the

111

electrostatic transformers to the model, where we use the analytical equations:

$$
\left[\begin{array}{c} \Delta F \\ \Delta I \end{array} \right] = \left[\begin{array}{cc} \Gamma & \left(\frac{k_{beam}-k'}{i\omega} + i\omega m_{beam} \right) \\ -\Gamma & i\omega C_0 \end{array} \right] \left[\begin{array}{c} \Delta V \\ \Delta \dot{x} \end{array} \right]
$$

$$
C_0 = \frac{\varepsilon_0 A_{electrode}}{d + x_0}
$$

$$
\Gamma = \frac{\varepsilon_0 A_{electrode} V_0}{(d + x_0)^2}
$$

$$
k' = \frac{\varepsilon_0 A_{electrode} V_0^2}{(d + x_0)^3}
$$

We assume the excitation to be voltage-controlled. For this simplified model, we also assume the electrostatic transducer for detection to be voltage-controlled:

$$
\left[\begin{array}{c} \Delta F_n \\ \Delta I_n \end{array} \right] = \left[\begin{array}{cc} \Gamma_n & \left(\frac{k_{mech,n}-k'_n}{i\omega} + i\omega m_{mech,n} \right) \\ -\Gamma_n & i\omega C_{0,n} \end{array} \right] \left[\begin{array}{c} \Delta V_n \\ \Delta \dot{x}_n \end{array} \right]
$$

Note that this is the linearized equation around an operating point. Inserting the above into eq. 6.5, we get the linearized state-space model:

$$
\left[\begin{array}{c} \Delta \dot{x}_1 \\ \Delta \dot{x}_2 \\ \Delta \ddot{x}_1 \\ \Delta \ddot{x}_2 \end{array} \right] = \left[\begin{array}{cccc} 0 & 0 & 1 & 0 \\ 0 & 0 & 0 & 1 \\ -\omega_1^2 + \frac{k'_1 - k_{couple}}{m_1} & \frac{k_{couple}}{m_1} & 0 & 0 \\ \frac{k_{couple}}{m_2} & -\omega_2^2 + \frac{k'_2 - k_{couple}}{m_2} & 0 & 0 \end{array} \right] \left[\begin{array}{c} \Delta x_1 \\ \Delta x_2 \\ \Delta \dot{x}_1 \\ \Delta \dot{x}_2 \end{array} \right]
$$

$$
+ \left[\begin{array}{cc} 0 & 0 \\ 0 & 0 \\ \frac{\Gamma_1}{m_1} & 0 \\ 0 & \frac{\Gamma_2}{m_2} \end{array} \right] \left[\begin{array}{c} \Delta V_1 \\ \Delta V_2 \end{array} \right]
$$

$$
y = \frac{\varepsilon_0 A_{electrode}}{d + x_2}
$$

$$
\left(\begin{array}{c} \Gamma_n = \frac{\varepsilon_0 A_n V_{dc,n}}{gap + x_{n,static}} \\ k'_n = \frac{\varepsilon A_n V_{dc,n}^2}{(gap + x_{n.static})^3} \end{array} \right)
$$

Note that we have assumed a capacitive detection that is voltage-controlled. The electrical equivalent, including the electrostatic transducer is shown in fig. 6.24.

6.6.4   Simulation results

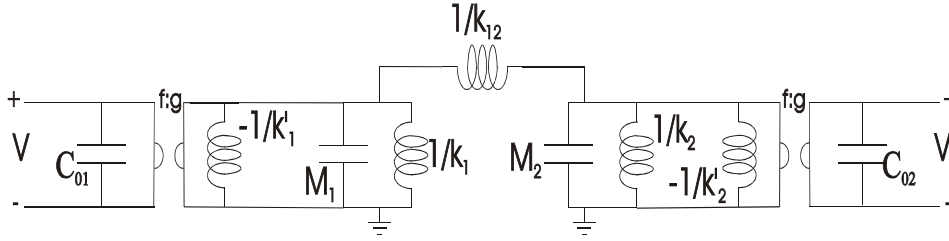In the simulations, we have assumed that both excitation and detection have a

Figure 6.24: The electrical equivalent of the 2-d.o.f. model, where the electrostatic transducer is included ($f \rightarrow V$ analogy).

static offset on voltage equivalent to 1 Volt:

$$V_{1,static} = 1Volt$$
$$V_{2,static} = 1Volt$$

With the static voltage, the system is solved nonlinearly with respect to static deformation. This information is again used in the state-space model, to obtain a linear approximation to the system response. Vital information and results can be summed up in the below table:

	Beam 1	Beam 2
Frequencies of beams	$\omega = 4.28 \cdot 10^7$	$\omega = 4.28 \cdot 10^7$
Applied static voltage	$1V$	$1V$
Static deformation (Δx_{dc})	$1.54 \cdot 10^{-7} \mu m$	$1.54 \cdot 10^{-7} \mu m$
Static capacitance ($C_{0,dc}$)	$1.328 \cdot 10^{-15}$	$1.328 \cdot 10^{-15}$
Applied AC-voltage	$0.5V$	$0V$
Low-frequency deformation (Δx_{ac})		$2.38 \cdot 10^{-8} \mu m$
Low-frequency Δcapacitance (ΔC_{ac})		$3.17 \cdot 10^{-23}$
Eigenfrequencies of system	$\omega_1 = 4.28 \cdot 10^7$	$\omega_2 = 5.15 \cdot 10^7$

(Δ symbolizes the amplitude of the sine)

Of importance at this stage, is the fact that we have ignored dissipative effects. Surrounded by an appropriate atmosphere with low pressure, litterature suggests that dissipation will generally be quite low, with examples ranging from Q's in the 100's to measurements over 10^5 for the mechanical structure ([80], [81], [82], [83]).This implies that the amplitudes in the table will at resonance be likely to be augmented by a factor in the range 10^3-10^5, assuming a linear system.

In fig. 6.25, we also show the frequency-response of the detection. This is calculated using a linearized system and assuming no dissipation, but due to vizualisation the infinite peaks are not shown.
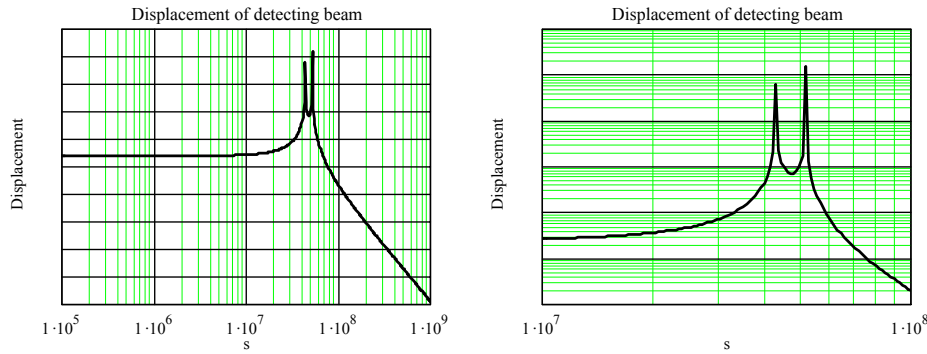
Figure 6.25: The transfer-functions of the system, with voltage as input and displacement of second beam as response. Right plot is shows a section of left plot.

6.6.5 Nonlinear analysis

Whilst the calculations apparently give good information about what values to expect, there are nonlinear effects in the system that we so far have ignored to a large extent. Looking at the definition of the parameters in the state-space model, we realize that there are two nonlinear effects, namely voltage-dependent nonlinearities and displacement-dependent nonlinearities. Comparing with the linear simulation above, it becomes clear that the displacement-dependent nonlinearities are comparatively small, since the gap at all times are much larger than the displacement. The voltage–dependent nonlinearities are, on the other hand, apparently very large. This is due to the excitation, which is quadratic in voltage($\propto V_1^2$). This becomes a significant nonlinearity with the values we have used, where $V_1 = 1V + 1V \cdot \sin(\omega t)$. It is therefore in place to analyse the full system. The nonlinear state-space model is:

$$
\begin{bmatrix} \dot{x}_1 \\ \dot{x}_2 \\ \ddot{x}_1 \\ \ddot{x}_2 \end{bmatrix} = \begin{bmatrix} 0 & 0 & 1 & 0 \\ 0 & 0 & 0 & 1 \\ -\omega_1^2 - \frac{k_{couple}}{m_1} & \frac{k_{couple}}{m_1} & 0 & 0 \\ \frac{k_{couple}}{m_2} & -\omega_2^2 - \frac{k_{couple}}{m_2} & 0 & 0 \end{bmatrix} \begin{bmatrix} x_1 \\ x_2 \\ \dot{x}_1 \\ \dot{x}_2 \end{bmatrix}
$$

$$
+ \begin{bmatrix} 0 \\ 0 \\ \frac{-\varepsilon A_1 V_1^2}{2(g+x_1)^2} \frac{1}{m_1} \\ \frac{-\varepsilon A_2 V_2^2}{2(g+x_2)^2} \frac{1}{m_2} \end{bmatrix}
$$

$$
y = \frac{\varepsilon_0 A_{electrode}}{d + x_2}
$$

114

Once again we note that the nonlinearities due to displacement are small (this can be verified by looking at static displacement and scale it with the Q-factor). This is not generally true, since one may obtain static displacements as large as $\frac{1}{3}$ of the gap before pull-in, given sufficient voltage. Since we do not look at such large voltages, the nonlinearity in excitation voltage is much more interesting. As indicated in the earlier section demonstrating the linear system, this nonlinearity may be utilized to adjust the system by applying a DC-voltage over one of the capacitances. For small AC-values of the voltage, the system behaves linearly. However, for larger values, a sine-excitation in voltage will have two frequency-components in mechanical forcing:

$$
\begin{aligned}
V^2 &= (V_{dc} + \Delta V \sin{(\omega t)})^2 \\
&= V_{dc}^2 + \frac{\Delta V^2}{2} + 2V_{dc}\Delta V \sin{(\omega t)} - \frac{\Delta V^2}{2}\cos{(2\omega t)}
\end{aligned}
$$

For excitations at frequencies at or above the system's two eigenfrequencies, this can often cause little problem since the parasitic frequency is twice that of the main part. For lower frequencies, however, this can be a problem since an excitation at low frequencies may be meant to be filtered out. The main part will in such a case be filtered out, put the parasitic frequency might be close to the system's eigenfrequencies and thereby not filtered out.

To conclude, the nonlinearities in the voltage is not a problem if the system is meant to operate as a resonator. In the case of using the system as a filter, however, the AC-part of the excitation voltage must be sufficiently low compared to the DC-part so that the parasitic effect is reduced to an acceptable level.

6.6.6 A 4-d.o.f. model of the microfilter

In the previous section (6.6.1), we built a small model of the microfilter with 2 degrees of freedom. In this section we will build a model with 2 additional degrees of freedom. This will hopefully demonstrate some shortcomings of the previous model.

From the state-space description of the previous model, it is seen that the coupling beam is modelled as massless. Although the mass of the coupling beam could be added to the model in the previous section, we will here first add another 2 degrees of freedom to the coupling beam and then add the mass of the beam to the model.

6.6.6.1 Shape functions

In the 2-d.o.f. model, the coupling beam was simply modelled as a spring. This was found by modelling the beam in a finite element fashion, where

Euler-Bernoulli beam theory gives us (eq. 6.1):

$$\begin{bmatrix} F_1 \\ M_1 \\ F_2 \\ M_2 \end{bmatrix} = \begin{bmatrix} \frac{12EI}{L^3} & \frac{6EI}{L^2} & -\frac{12EI}{L^3} & \frac{6EI}{L^2} \\ \frac{6EI}{L^2} & \frac{4EI}{L} & -\frac{6EI}{L^2} & \frac{2EI}{L} \\ -\frac{12EI}{L^3} & -\frac{6EI}{L^2} & \frac{12EI}{L^3} & -\frac{6EI}{L^2} \\ \frac{6EI}{L^2} & \frac{2EI}{L} & -\frac{6EI}{L^2} & \frac{4EI}{L} \end{bmatrix} \begin{bmatrix} u_1 \\ \phi_1 \\ u_2 \\ \phi_2 \end{bmatrix} \tag{6.6}$$

By applying the appropriate boundary conditions, $\phi_1 = \phi_2 = 0$, we obtain the equivalent spring stiffness.

At this stage it is important to realize the link between the nodal displacements and the displacements over the length of the beam. Generally, each nodal displacement causes a displacement over the whole of the beam. The shape of the displacement is defined by the shape function:

$$u_n(x) = u_n \cdot f_n(x)$$

Where $u(x)$ is the displacement at position x along the beam, u_n is the displacement at the nodal point n, and $f_n(x)$ is the shape function. The sum of all the displacements is equivalent to the total displacement:

$$u_{total}(x) = \sum_n u_n(x)$$

Generally, any shape function is legal as long as it satisfies two requirements. The first is that the function must be equivalent to the nodal displacement at the node. The second is that the shape function must be zero at all other nodes. A commonly used shape function is a polynomial function:

$$u_n(x) = u_n \sum_n a_n x^n \tag{6.7}$$

Here, the a's are chosen so that the shape function satisfies the above-mentioned criterias, and n is the order of the shape-function. These shape-functions are then applied to the governing equations, and the result is a finite element, like that of eq. 6.6. To develope the finite element of eq. 6.6, second-order shape functions are used. Due to the second-order degree of the shape-function, the shape of the function is determined by the translatory displacement (u_n) and also the gradient of the translatory displacement (ϕ_n). More on this subject can be found in books like [4], [84].

The shape-functions have large impact on the accuracy of the modelling. The overall deformation of the structure is governed by the shape functions, hence the structure is not free to deform in an energy-minimzing shape. Thus the energy in the deformed structure may be over-estimated. The effects of the shape-function approximation can therefore be summed up in two points main points, with the first being that the stiffness of the structure will be too high. The second effect is that the overall displacement will not be exactly
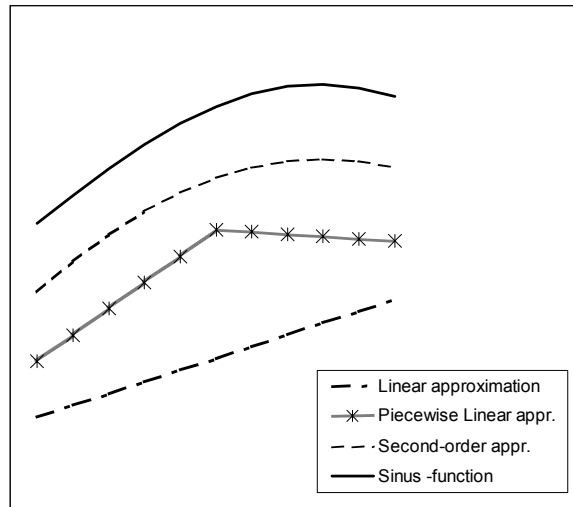
Figure 6.26: The full line demonstrates some function to be approximated. Underneath are respectively a second-order approximation, a piecewise first-order (linear) approximation, and single first-order approximation.

equivalent to the exact solution. More about the topic can be found in i.e. [4], [85].

Both the two mentioned effects appears to make the finite element method inaccurate. But as pointed out above, the inaccuracy is due to lack of the shape-function to approximate the true deformation. Hence, a shape function that is capable of approximating the true deformation better, would improve the accuracy. This can be accomplished by increasing the order of the shape-function (see eq. 6.7). Alternatively, the structure can be divided into two parts, where deformation of each part is described by the shape function. In fig. 6.26, we demonstrate the two approaches, using a zero-order shape function as basis. Both increasing the order of the shape-function, and dividing the structure into smaller elements, makes the FE-solution converge towards the exact solution.

6.6.6.2 Modelling of the coupling beam

In the discussion above, we gave reasons for why lumped models are inaccurate. A possible solution to increase accuracy was to divide the structure in more elements. We will do this with the coupling beam, and incorporate this into a full state-space model of the filter.

The finite element we use is the commonly used beam element of eq. 6.6. We write the element in a more compact fashion:

$$
\begin{bmatrix} f_n \\ f_{n+1} \end{bmatrix} = \begin{bmatrix} {}^eK_{1,1} & {}^eK_{1,2} \\ {}^eK_{2,1} & {}^eK_{2,2} \end{bmatrix} \begin{bmatrix} x_n \\ x_{n+1} \end{bmatrix}
$$

Here the states (u_n, ϕ_n) at each node is gathered in x_n, equivalent treatment is done with the force and moment, expressed as f_n. The stiffness matrix, ${}^eK$ is divided into 4 submatrices. The n indicates the number of the node, whereas the e indicates element. Two such elements can be gathered together:

$$
\begin{bmatrix} f_1 \\ f_2 \\ f_3 \end{bmatrix} = \left(\begin{bmatrix} {}^1K_{1,1} & {}^1K_{1,2} & 0 \\ {}^1K_{2,1} & {}^1K_{2,2} & 0 \\ 0 & 0 & 0 \end{bmatrix} + \begin{bmatrix} 0 & 0 & 0 \\ 0 & {}^2K_{1,1} & {}^2K_{1,2} \\ 0 & {}^2K_{2,1} & {}^2K_{2,2} \end{bmatrix} \right) \begin{bmatrix} x_1 \\ x_2 \\ x_3 \end{bmatrix}
$$

$$
= \begin{bmatrix} {}^1K_{1,1} & {}^1K_{1,2} & 0 \\ {}^1K_{2,1} & {}^1K_{2,2} +{}^2 K_{1,1} & {}^2K_{1,2} \\ 0 & {}^2K_{2,1} & {}^2K_{2,2} \end{bmatrix} \begin{bmatrix} x_1 \\ x_2 \\ x_3 \end{bmatrix}
$$

Finally, appropriate boundary conditions are applied. We have chosen them to be $\phi_1 = \phi_3 = 0$, which is consistent with no torsional deformation of the main beams. Furtermore, the displacements u_1 and u_3 are connected directly to the displacement of the main beams. Equivalent treatment is done with the mass matrix.

6.6.7 Electrical equivalent

In the above, we showed how the state-space model was buildt. We will here show how the same model is buildt using the electrical equivalent approach. Our starting-point is the 2-d.o.f. model of the filter, see fig. 6.21. We can identify the coupling beam as the inductance with the value $1/k_{12}$.

Returning to an earlier section in this chapter, we demonstrated how a beam element could be modelled using an electrical equivalent in the $f \rightarrow V$ convention, see fig. 6.11. We also showed how two such beam elements could be coupled in fig. 6.12. We use the latter and apply appropriate boundary conditions (no rotation at ends of the coupling beam.). Thus we obtain a model of the coupling beam more complex, and with a potential to be more accurate, than the single conductance used in the 2-d.o.f. model. The slightly more involved beam model is then connected to the main beams. The procedure is shown in fig. 6.27, along with the final model.

6.6.8 Simulation results

The simulations of the 4-d.o.f. model could clearly be done using either the equivalent circuit or the state-space model. Either model would give the same result. Here, we use the state-space model.

A plot of the transfer-function is shown in fig. 6.28. Comparing with the transfer-function of the 2-d.o.f. model (see fig. 6.25), we see that the 4-d.o.f. model have two additional resonance-peaks. This is expected, since an undamped 2-d.o.f. model generally have 2 resonance frequencies, while an
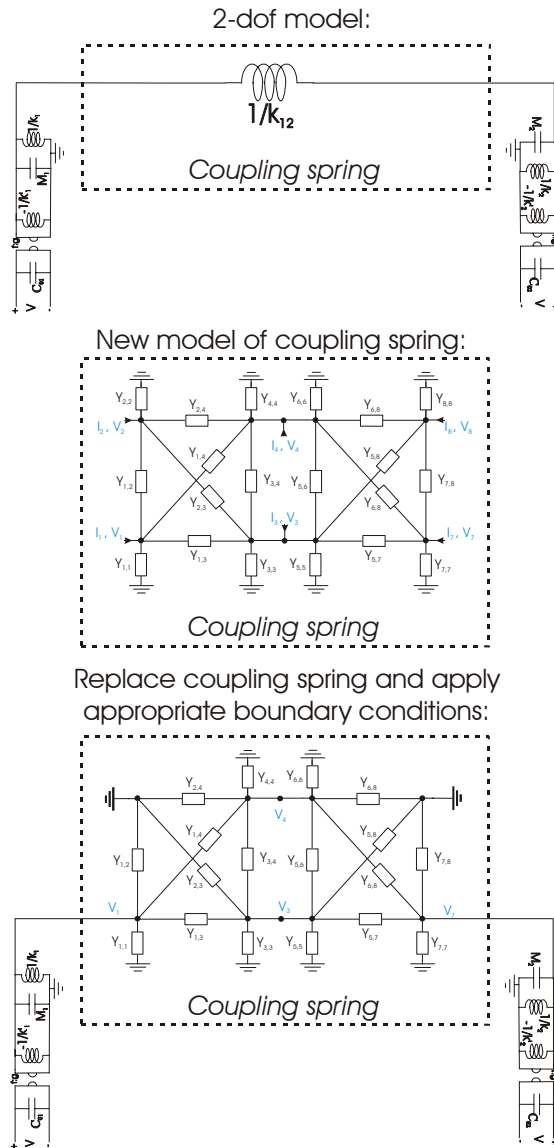
Figure 6.27: Top: Showing the earlier presented 2-d.o.f. model, where the coupling spring is identified. Middle: Shows a more involved model of the coupling spring. Bottom: The simple spring model is replaced by the more involved. Boundary conditions are imposed (bold lines).
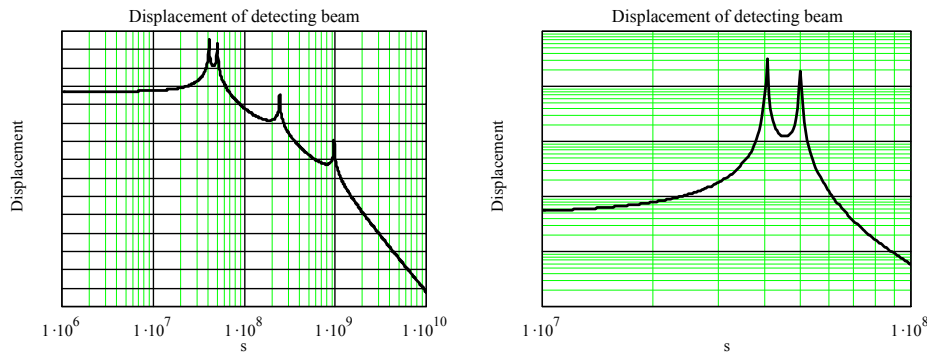
Figure 6.28: The transfer-function of the 4-d.o.f. model (right plot shows a section of left plot).

undamped 4-d.o.f. model generally have 4 resonance frequencies.

Simulations of the 4-d.o.f. shows that static behaviour is equivalent to those of the 2-d.o.f. model. Dynamic behaviour of the system is indicated by the eigenfrequencies. The eigenvalues of the 4-d.o.f. model is plotted in the below table, alongside those of the 2-d.o.f. model:

	4-d.o.f. model	2-d.o.f. model
ω_1	$4.045 \cdot 10^7$	$4.28 \cdot 10^7$
ω_2	$4.998 \cdot 10^7$	$5.15 \cdot 10^7$
ω_3	$2.41 \cdot 10^8$	-
ω_4	$9.58 \cdot 10^8$	-

Comparing the two lowest eigenfrequencies of the two models, we realize that those of the 4-d.o.f. model indicate much lower resonance frequencies of the system. Since the static behaviour of the two systems are equivalent, this implies that it must be the inertial modelling that gives the different eigenfrequencies. We recall that we ignored mass of the coupling beam in the 2-d.o.f. model, but included it in the 4-d.o.f. model. A heuristic conclusion of that fact, would be that the resonance frequencies of the 4-d.o.f. model would be expected to be lower than those of the 2-d.o.f. model. This is also what we see from the above table.

The mass of the coupling beam could easily be implemented in the 2-d.o.f. model in an analytical manner. This would greatly improve the accuracy of the eigenfrequencies. However, this would not give any more information about other eigenfrequencies, and as we can see from the transfer-plot in fig. 6.28, other eigenfrequencies are in the neighbourhood of the two lower eigenfrequencies, threatening the system performance. Clearly, this information is important.

6.6.9 An n-d.o.f. model of the microfilter

In the previous we have presented two compact models of the microfilter. The analytical expression of the elements in the models, combined with the compact size of the models, make them attractive as macromodels. However, by comparing the 2-d.o.f. model with the 4-d.o.f. model, it was indicated that the models had a lack of accuracy and validity for certain properties. It is therefore in place to build a larger model. This is both to verify the accuracy of the smaller models and to get knowledge about complex behaviour.

The objective of such an involved model is to create a model that as accurate as possible describe both the mechanical and the electrostatic behaviour. A possible solution to this, is to use a couple simulator that allows one to model both the mechanics and the electrostatics in a finite element environment. However, solving electrostatic problems using finite elements are not very efficient. An alternative is to use a coupled simulator allowing the mechanics to be solved using a FE-method, whereas the electrostatics is solved in a boundary-element fashion. For both the mechanics and the electrostatics to be modelled accurately, the structures need to be discretized sufficiently.

In this section, we will discretize the mechanical structure into a number of beam-elements. This means that each beam is divided into a number of beam-elements. The beam elements we use take three degrees of freedom, namely displacement in z-direction, and rotation around the x- and y-axis.

6.6.9.1 Simplifications for the electrostatic problem

The electrostatics is modelled using a BE-method. A precise model of the electrostatics of the microfilter would include an accurate 3-D description of the geometry and the dielectric interfaces. To simplify the description of the system and the size of the governing matrix, we consider a 2-dimensional model. Furthermore, only the elements stemming directly from the filter are included in the model. This means that parasitics from nearby conductors etc. are ignored. All these simplifications concern accuracy, computation time, and degrees of freedom in model.

With the simplifications listed above, the BE-model still have a significant number of degrees of freedom, since each electrode is discretized into a number of elements. Hence the governing equation is:

$$[A]\left[\rho_{\text{charge}}\right] = [V]$$

Note that the conductors between the collocation points have been ignored in the governing equations. We assume that the potential on a given electrode is constant, independent of how many elements that electrode was divided into. The surface charge density on the electrode may therefore vary. This may lead to a significant reduction of matrix-size in one dimension ($n \times n \rightarrow n \times N$).

$$
\begin{aligned}
[A]\left[\rho_{\text{charge}}\right] &= [V] & \text{(6.8a)} \\
[A]\left[\rho_{\text{charge}}\right] &= [B_V][V_{small}] & \text{(6.8b)} \\
\left[\rho_{\text{charge}}\right] &= [A_{red}]^{-1}[B_V][V_{small}] & \text{(6.8c)} \\
\left[\rho_{\text{charge}}\right] &= [A_{small}][V_{small}] & \text{(6.8d)}
\end{aligned}
$$

Where $[B_V]$ is the matrix linking the voltages of the element with the voltages on the electrodes. Parallel to this, one may also sum up the charges on each electrode to find the total charge on each electrode:

$$
\left[\rho_{\text{charge\_small}}\right] = [D_{\text{charge}}]\left[\rho_{\text{charge}}\right] = [D_{\text{charge}}][A_{small}][V_{small}] \qquad \text{(6.9)}
$$

Here, $[D_{\text{charge}}]$ links the charges of each element to the charges of each electrode.

6.6.10   Electrostatic forcing

Following 6.6.9.1, we are able to express the relation between charge and voltage on the electrodes. While the capacitances have been calculated more accurately using a numerical approach (BEM), the results does not give direct access to the electrostatic forcing. However, by applying the scheme presented in 6.4.6, we may create the full transducer description from numerical results.

The obtained description is then of the form:

$$
\begin{bmatrix} \Delta V_{electrodes} \\ \Delta F_{electrodes} \end{bmatrix} = [A_{small}] \begin{bmatrix} \Delta I_{electrodes} \\ \Delta \dot{x}_{electrodes} \end{bmatrix}
$$

It is of importance to realize that the BEM-results stems from a 2D-simulation, where the electrodes are assumed to be infinitely long. It then follows that the displacement of an electrode must be a true translation, which must be the same for all points along the electrode for the model to be truely valid. The beams are, however, doomed to bend, making the displacement dependent upon position on the electrode. Each capacitor must therefore be replaced by a number of capacitances in parallel. The full procedure from the initial full 2D boundary model, to obtaining the distributed model along the beam axis is shown schematically in fig. 6.29. The first step in the figure, that is reducing initial 2D boundary element model, was explained mathematically in 6.6.9.1. The last step in fig. 6.29, is actually two-fold. The first step is simply to create a number of distributed elements:

$$
\begin{bmatrix} \Delta V_{element} \\ \Delta F_{element} \end{bmatrix} = \frac{1}{N} \cdot [A_{small}] \begin{bmatrix} \Delta I_{element} \\ \Delta \dot{x}_{element} \end{bmatrix}
$$

Where $x_{element}$ is a vector equivalent to that in $x_{electrodes}$, except that the

matrix has now been scaled to match the length of the elements. This is seen since N is the number of elements along the length of the beam axis (assumed to be equal in length). All these elements are now stacked together to form the full transducer system:

$$
\begin{bmatrix} \Delta V_{element\#1} \\ \Delta F_{element\#1} \\ \vdots \\ \Delta V_{element\#N} \\ \Delta F_{element\#N} \end{bmatrix} = \frac{1}{n} \cdot \begin{bmatrix} A_{small} & 0 & 0 \\ 0 & \ddots & 0 \\ 0 & 0 & A_{small} \end{bmatrix} \begin{bmatrix} \Delta I_{element\#1} \\ \Delta \dot{x}_{element\#1} \\ \vdots \\ \Delta I_{element\#N} \\ \Delta \dot{x}_{element\#N} \end{bmatrix}
$$

With a little rearrangement, we have obtained the matrix governing the transducer system. However, the final step still lacks, where the forcing vector in the above equation needs to be reformated. This is needed both because the forcing ought to be consistent (in terms of what was explained in 6.2.4), but also because the discretization of the electrostatic problem not necessarily match that of the mechanical problem.

6.6.11   Full model

In this section, we discuss a model of the microfilter in fig. 6.1 based on the above results and methods. The model is presented schematically in fig. 6.30, as an equivalent circuit in the $f \to V$ analogy.

First, the three main beams can be easily distinguished in the figure, by recognizing that each beam consists of a number of beam elements (since the two main beams are equal in geometry and discretization, they use the same type of beam elements). These beam elements are electrical equivalents similar to that given in fig. 6.11. The difference being that here we use three degrees of freedom, namely z (translation), ϕ_y (angle), and ϕ_x (angle) instead of two in the example in fig. 6.11.

Secondly, the transducer elements are also easily identified by the gyrator elements. Note that in the schematics, the parasitic effects between electrodes have been ignored for better visualization. Another point to observe is that the transducer elements give excitation both in force and moment. At a first glance, this may appear incorrect. However, according to earlier discussions on external forcing on finite elements, this is generally correct when consistent loading is used (6.2.4).

6.6.12   Simulation results and discussion

We have used the above model to simulate the behaviour of the system. The result will be presented alongside some of the results obtained from the 2-d.o.f. model and the 4-d.o.f. model. We compare and discuss the results.

An important characteristic of the system, is its frequency-behaviour. In fig. 6.31, we see a plot of the transfer-function obtained from the n-d.o.f. model. Immediately we recognize the much more involved transfer-function
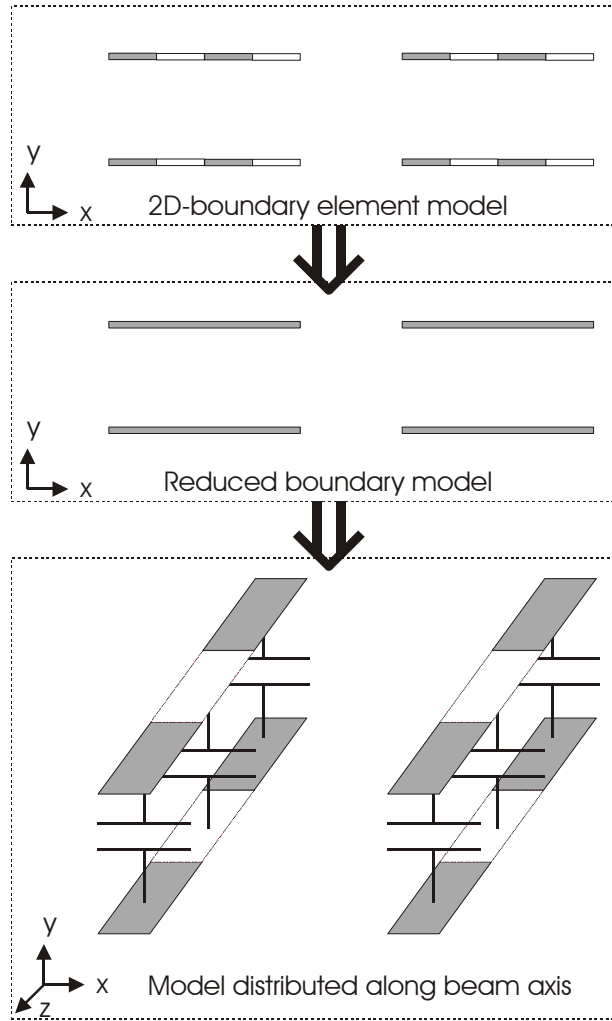
Figure 6.29: Schematics demonstrating how the initial 2D electrostatic model is first reduced, and then distributed along (parts of) the length of the beam. In the bottom part, the capacitances between electrodes on left and right side have not been plotted. This is to simplify the schematics.

Figure 6.30: The schematics of the equivalent circuit ($f \rightarrow V$ analogy) of the microfilter. Some details are left out, like that the transducer elements do not necessarily have the same values.

than indicated by the 2-d.o.f. model and the 4-d.o.f. model (see figs. 6.25, 6.28). At the same time, we compare the resonance-frequencies of the system, obtained from the three models:

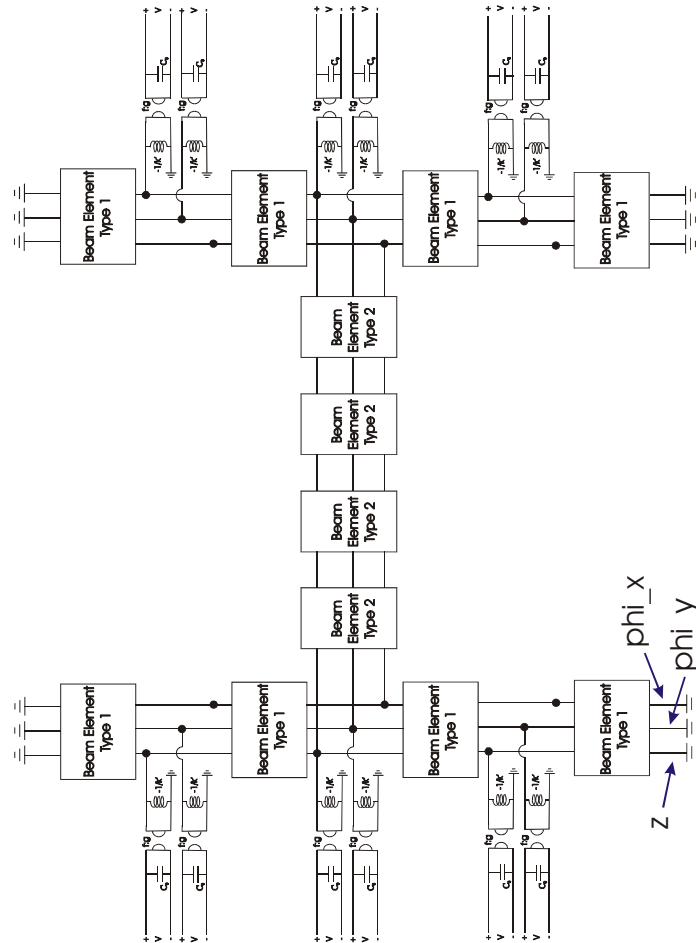|	n-d.o.f. model	4-d.o.f. model	2-d.o.f. model
ω_1	$3.873 \cdot 10^7$	$4.045 \cdot 10^7$	$4.28 \cdot 10^7$
ω_2	$4.644 \cdot 10^7$	$4.998 \cdot 10^7$	$5.15 \cdot 10^7$
ω_3	$1.05 \cdot 10^8$	$2.41 \cdot 10^8$	-
ω_4	$1.086 \cdot 10^8$	$9.58 \cdot 10^8$	-
ω_5	$1.667 \cdot 10^8$		
ω_6	$1.792 \cdot 10^8$		
$\vdots$	$\vdots$		

Most obvious is the fact that the higher-degree models have more resonance frequencies than the lower. It is however, also interesting to note the value of the first two resonance frequencies. We note that the simplest model indicate a higher resonance frequency, while the largest model indicate the lowest value. This is consistent with our earlier discussion on degrees of freedom versus energy-minimization. Looking at resonance frequencies 3 and 4, they don't appear to be comparable at all for the two models. This is due to the restriction upon the main beam deformation in the 4-d.o.f. model. In the larger model, these restrictions are effectively loosened, and the main beams are much more free to move. In this case we see that we have introduced 'new' resonance frequencies, and not only a more accurate calculation of the resonance frequencies obtained from the 4-d.o.f. model. This indicates that our choice of freedom in the 4-d.o.f. model is not optimal.

We see that the smallest model give us a good understanding of the fundamental behaviour of the system. However, as we can see from the transfer-function plots (see figs. 6.25, 6.31) the model does not give us information about significant parasitic effects. The two larger models, however, are more or less capable of giving us information about possible important parasitic effects. One can clearly see the use of all these models, where the simplest model gives the designer a very transparent and simple parametrized model. However, the model is not very accurate and fails to predict important parasitic effects. The 4-d.o.f. model is more accurate, but is still small and transparent. It does give information about parasitic effects, albeit inaccurately. The largest model is of special interest, not because it fulfill the requirements of a macromodel, which it hardly does, but because it can, and should, be used as a standard when evaluating the smaller models performance. Clearly, if a more involved model where available this would be used instead.

For the performance of the system, we can see that a main problem of this design is to isolate the two main resonance peaks from the parasitic resonances. Although the geometry can be optimized to reduce this problem, it is a difficult task. A major problem in this respect is the processing capabilities,
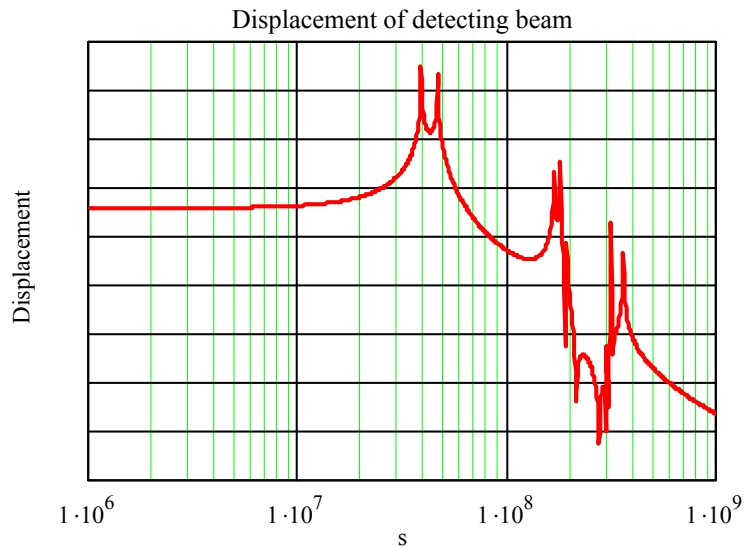
Figure 6.31: Transfer-function for the system as given by the n-d.o.f. model.

giving restrictions to geometric size and giving rise to process tolerances of the geometry. An approach to improving system behaviour is to create a more complex systems of beams, which one can see has been done for mechanical filters created in the 1970's [67].

6.7 Discussion and conclusions

We have in this chapter presented general theory regarding modelling of basic mechanical and electrical elements. Furthermore, we have used this knowledge to demonstrate how mechanical systems can be presented in terms of electrical equivalents. It was shown that the $f \rightarrow V$ analogy is generally more intuitive than the $e \rightarrow V$ analogy for creating electrical equivalents. This is since the $f \rightarrow V$ analogy has a more intuitive link between variables in the electrical domain and variables in the mechanical domain.

Furthermore, we looked at an electrostatic transducer element. We presented the element in the $e \rightarrow V$ analogy, and reformulated it to the $f \rightarrow V$ analogy. The latter circuit involves the use of a gyrator.

We continued by investigating a microresonator by means of lumped modelling. Simulations of the system where done with three different models, where each model had a different number of degrees of freedom. As expected, the overall performance of the models degraded with fewer degrees of freedom in the model. However, the operational principle becomes very clear in the most compact (lumped) models. To capture parasitic effects the

lumped models must be slightly more involved. It is, however, in many cases difficult for an engineer to create a lumped model that captures the parasitic behaviour accurately. This difficulty can be strongly alleviated by performing high-precision simulations that reveals the basic (and more complex) parasitic effects. This knowledge can then be used to choose the degrees of freedom of the lumped model in a more optimal manner.

We utilized a microfilter to examplify equivalent electrical modelling of mechanical systems. These models presents the behaviour of the microfilter in a more or less accurate manner. We see that the microfilter operate in the MHz-range, but is by no means optimized for a specific use. We can f.ex. see that the system has a quite wide passband in the primary band, making it useless as a resonator. We can furthermore see that the system have a number of parasitic resonances quite close to the primary resonances, hence degrading the system's performance used as a filter. However, we note that we have made no attempts to optimize the system behaviour.

Chapter 7
The Modelling Of A Cavity Based Electromagnetic Suspension System

In this chapter we will investigate an electromagnetic levitation system comprising a detuned microwave cavity. The cavity takes the form of a ring-resonator supporting a TM mode, the fields of which generate suspension forces on an unattached 'free' wall of the cavity. In fig. 7.1, we show the cavity with a disc shaped wall. Also included in the figure is a possible embodiment of a suspended disc shaped conducting plate, utilizing two cavities. This chapter is largely based on [86], where we present the analysis of the single cavity suspension system and the results.
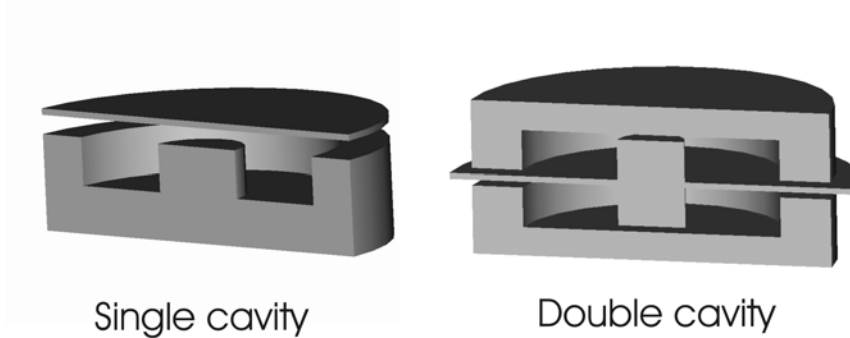
Figure 7.1: SINGLE CAVITY: TM-mode ring resonator levitating a disc shaped conducting plate. DOUBLE CAVITY: Possible embodiment of disc shaped conducting plate suspended between two TM-mode ring resonators.

In the earlier chapters, focus was on how to create a simplified model based on an initially large and potentially complex mathematical model. As indicated in the opening chapters, a different approach can be taken, where the model is created on the basis of "engineering knowledge". This may involve building-blocks for which the behaviour is generally well-known. An alternative is to attack the governing equations directly, and perhaps discretize them in a proper manner, resulting in some kind of lumped model.

In this chapter we adopt the latter strategy. From the outset, there were two main reasons for choosing such a strategy. The first reason was merely that "accurate" and fully discretized modelling results in an impractically large model, hence reducing such a model would also be difficult. The second

reason was that a quasi-analytical compact model would give better physical insight into the system behaviour.

7.1 Electromagnetics and waveguides

Preparing for an investigation of the electromagnetic system, we present some fundamental equations that are used at a later stage. For a more thorough introduction to the field, we refer the reader to introductory books on electrodynamics, like e.g. [87],[88].

In electromagnetics, Maxwells equations play much the same role as do Newton's laws in mechanics. Maxwells equations are:

$$\nabla \cdot \mathbf{D} = \varrho_V \qquad \text{(Gauss's law)}$$
$$\nabla \cdot \mathbf{B} = 0 \qquad \text{(Gauss's law for magnetism)}$$
$$\nabla \times \mathbf{E} = -\frac{d\mathbf{B}}{dt} \qquad \text{(Faraday's law)}$$
$$\nabla \times \mathbf{H} = \mathbf{J} + \frac{d\mathbf{D}}{dt} \qquad \text{(Ampere's law)}$$

The variables are as follows: $\mathbf{E}$ is the electric field, $\mathbf{D}$ is the electric flux density, $\mathbf{B}$ is the magnetic flux density, $\mathbf{H}$ is the magnetic field, while $\mathbf{J}$ is the current density. ϱ_V represents the volume charge density. Furthermore we have the consitutive equations (for linear, isotropic nonferromagnetic media, [87]):

$$\mathbf{D} = \varepsilon \mathbf{E}$$
$$\mathbf{B} = \mu \mathbf{H}$$

where ε is the permittivity and μ is the permeability.

7.1.1 Waveguides

Waveguides are hollow devices being relatively long compared to their transverse dimensions. They are surrounded by metals or dielectric media. Inside, wave modes can be excited, and they can be made to travel along the longitudinal direction of the waveguide. Examples of waveguides are coaxial cables and rectangular waveguides, where the latter are a common feature for guiding antenna signals.

We consider a time-harmonic solution of Maxwells equations:

$$\nabla \cdot \bar{\mathbf{E}} = 0$$
$$\nabla \cdot \bar{\mathbf{H}} = 0$$
$$\nabla \times \bar{\mathbf{E}} = -i\omega\mu\frac{d\bar{\mathbf{H}}}{dt}$$
$$\nabla \times \bar{\mathbf{H}} = i\omega\varepsilon\frac{d\bar{\mathbf{E}}}{dt}$$

where the line over the vectors implies phasor-notation. Since we are exam-

ining waves travelling in the $+z$-direction, this means that we have defined:

$$
\begin{aligned}
\bar{\mathbf{E}} &= \mathbf{E}\left(x, y\right) e^{-ik_z z} \\
\bar{\mathbf{H}} &= \mathbf{H}\left(x, y\right) e^{-ik_z z}
\end{aligned}
$$

where k_z is a wavenumber.

Focusing on two-dimensional waveguides, we can classify a number of important waveguide modes. If $E_z = H_z = 0$, we have a transverse electromagnetic (TEM) mode (here, the z-axis is the longitudinal direction along the waveguide). Parallel to this, we obtain a transverse electric (TE) mode if only $E_z = 0$. Hence we have an transverse magnetic (TM) mode when only $H_z = 0$.

7.1.2 Magnetostatic forces

A second area of interest is the magnetostatic forces. The conducting walls in a cavity will experience magnetostatic forces. They can be derived using the Lorentz force law:

$$
\mathbf{F} = q\mathbf{v} \times \mathbf{B}
$$

where $\mathbf{F}$ is the mechanical force, q is a charge, and $\mathbf{v}$ is the velocity of the moving charge. This can be reformulated so that we obtain the distributed force density, $\mathbf{F}_{surface}$:

$$
\mathbf{F}_{surface} = -\mathbf{J} \times \mu\mathbf{H}
$$

where $\mathbf{J}$ is the (surface) current density. The surface current in the conducting walls of a waveguide can easily be found:

$$
\mathbf{J} = \mathbf{n} \times \mathbf{H}
$$

Here, $\mathbf{n}$ is the normal vector to the surface. Using these equations, we obtain a simple relation between the magnetic field and the force, which is valid for the waveguide-walls:

$$
\mathbf{F}_{surface} = -\left(\mathbf{n} \times \mathbf{H}\right) \times \mu\mathbf{H}
$$

7.2 Fundamentals of the device

Despite the advances of the MEMS-area, severe problems continue to be presented by the very high frictional (in relative terms) forces and wear associated with micro-sized moving parts in MEMS devices [89]. A possible solution to this problem is attainable through levitation of the motive element of the micro-machine. For example in references [90] and [91] levitation in a micro-machine is procured by using electrostatic forces, but the system is complicated, and expensive to implement, because of the need to provide

sensing and control to ensure stability. It has also been suggested [92] that intrinsically stable magnetic suspension of the rotor of an electrostatic micromotor could, in principle, be procured by using diamagnetic materials to stabilise the system. However, the slow response time of such a system to rotor misalignment could present a major obstacle to its likely effectiveness.

On the other hand, it has been shown [89], that responsive intrinsically stable levitation of a small (millimetre and sub-millimetre sized) conducting rotor within an electro-static micromotor can be achieved if the rotor forms part of the capacitive element of a detuned resonant LC circuit. This solution has been demonstrated in practice, only for relatively large planar ($\tilde{}$2 cm^2) conducting pads [93], which permit the easy realisation of the capacitive and inductive components at resonant frequencies in the MHz range. More recently, however, by employing microwave (10 GHz approximately) cavity resonators rather than L-C circuits, it has been shown that modal field patterns can be set up which permit a 'floating' wall to be lifted without quenching the resonance. This suggests that the stable suspension of millimetre scale flat conducting discs [94],[95],[96] should be possible. Furthermore, the relatively high Q, which is available from cavity resonators, offers the added advantage that useful levitation fields can be attained at relatively low power levels which are easy to generate. An illustration of the ring resonator system for a thin disc shaped conducting plate levitated above the TM-mode ring resonator was presented in fig. 7.1 (single cavity). Electromagnetic field computations on ring-cavities, of the single cavity depicted in fig. 7.1, indicate that the ratio of the levitation force (F_l) to the gravitational force (F_g) in a single cavity system incorporating an aluminium disc-shaped 'float' of commensurate dimensions, is given approximately by the relation:

$$\frac{F_l}{F_g} \tilde{\simeq} 4 \frac{f^2 P Q}{c^3 \rho g t} \tag{7.1}$$

where is the resonant frequency in Hz, P is the power supplied in watts, Q is the quality factor for the cavities, c ($\frac{m}{s}$) is the speed of light, ρ ($\frac{kg}{m^3}$) is the density of the disc, g is the gravitational acceleration and t is the disc thickness in metres. The equation clearly shows that for a given power input, high operating frequency secures high relative levitation force. At 300 GHz, for example, a cavity system with $Q = 10000$, $P = 1mW$, $t = 0.5mm$, $\rho = 1\frac{gram}{cm^3}$, produces a levitation force which is approximately 25 times the gravitation force. For an actuator in a MEMS device, weighing typically $0.1mg$, this means that levitation forces of the order of several micro-newtons are predicted. It is interesting to note [97] that without cavity enhancement, electromagnetic pressure using a $750mW$, $10mm$ diameter, laser beam generates a force of 5 nano-Newtons when perfectly reflected by a mirror surface. This is shown to be sufficient to drive a MEMS actuator.

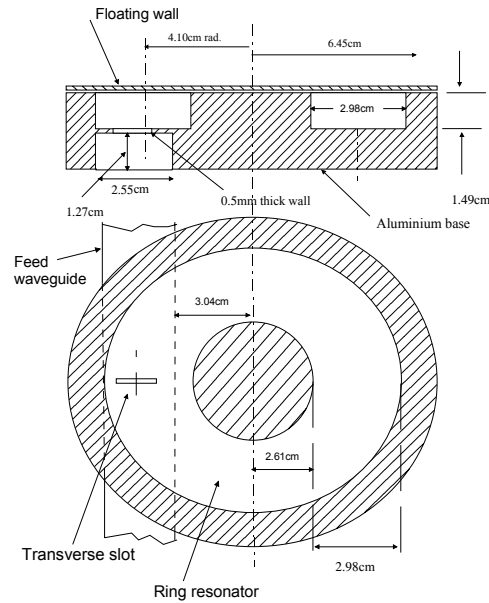While sufficient force is potentially available to secure electromagnetic

Figure 7.2: Schematic of the ring resonator as used in levitation experiments.

levitation using a high-Q microwave cavity resonator, the stability of such systems remains to be assessed. It is the purpose of the following sections to examine the electromagnetic boundary problem represented by a ring-mode cavity resonator with a floating outer wall in order to determine the level and distribution of the suspension forces over the surface of the wall for various levitation conditions. These forces are then used, in an assessment of the mechanics of the disc shaped float subjected to the electromagnetic pressure from below, to assess stability criteria.

7.3   Analysis

Macroscopic levitation experiments performed at approximately 11.5 GHz have been carried out using a TM mode rectangular waveguide ring resonator model. The reasons behind this choice were manifold. Firstly, when operated in a TM mode (TM$_{11}$ in this case, the meaning of the subscript is explained later) the waveguide-ring supports circumferential wall currents which means that the TM mode is not significantly disturbed by loss of contact between the floating wall (fig. 7.2) and the ring resonator base. Secondly it is relatively easy to couple to the TM mode through a transverse (radial) slot in the waveguide. Thirdly directional coupling is readily achievable using two slots (not shown). Fourthly the travelling-wave ring mode provides potentially uniform levitation forces around the ring.

133

The levitation mechanism can be illustrated, and the force available as a function of power and frequency can be determined, by first considering the field expressions for a TM_{11} mode in a rectangular waveguide with major dimension a and minor dimension b. For a ring-resonator whose inner radius of curvature is greater than λ (the wavelength), it is possible without too much loss of generality to formulate the modal equations from the Maxwell equations by using a linearized version of the cavity. The key requirement in setting up this model is the enforcing of boundary conditions at the input and output ports of the linear cavity which ensure that the transverse fields in the ports are in the same phase and magnitude relationship which they would possess in the ring. The linearized version has the advantage that deviations of the floating wall from parallel alignment with the base can be more easily modelled. The resulting fields can generally be expressed as:

$$\bar{\mathbf{E}}_0 = \begin{bmatrix} E_x \\ E_y \\ E_z \end{bmatrix} = \begin{bmatrix} -\frac{\gamma}{k_c^2} \frac{n\pi}{L_x} \sin\left(\frac{m\pi}{L_y}y\right)\cos\left(\frac{n\pi}{L_x}x\right) \\ -\frac{\gamma}{k_c^2} \frac{m\pi}{L_y} \cos\left(\frac{m\pi}{L_y}y\right)\sin\left(\frac{n\pi}{L_x}x\right) \\ \sin\left(\frac{m\pi}{L_y}y\right)\sin\left(\frac{n\pi}{L_x}x\right) \end{bmatrix}$$

$$\bar{\mathbf{H}}_0 = \begin{bmatrix} H_x \\ H_y \\ H_z \end{bmatrix} = Y_{TM} \begin{bmatrix} \frac{\gamma}{k_c^2} \frac{m\pi}{L_y} \cos\left(\frac{m\pi}{L_y}y\right)\sin\left(\frac{n\pi}{L_x}x\right) \\ -\frac{\gamma}{k_c^2} \frac{m\pi}{L_y} \sin\left(\frac{m\pi}{L_y}y\right)\cos\left(\frac{n\pi}{L_x}x\right) \\ 0 \end{bmatrix}$$

$$Y_{TM} = \frac{\sigma + i\omega\varepsilon}{\gamma}$$

$$k_c = \sqrt{\left(\frac{n\pi}{L_x}\right)^2 + \left(\frac{m\pi}{L_y}\right)^2}$$

Where γ is the propagation constant, L_x and L_y is the dimension of the rectangle, and σ is the conductivity of dry air. The angular frequency is given by ω. The n and m are integers.

Looking at the fields, the origin of the TM_{nm}-labelling can be found, selecting a TM_{11} mode means setting $n = m = 1$.

To correctly model the ring resonator fields it is essential that both the forward travelling-wave $(-z)$ and the backward travelling-wave $(+z)$ in the linearized cavity are accommodated. The full field set can be written as follows, using subscript F for the forward wave and subscript B for the

134

backward wave:

$$
\begin{aligned}
\bar{\mathbf{E}}_{0\_F}\left(x,y,z,t\right) &= \bar{\mathbf{E}}_0\left(x,y\right)e^{i\omega t}e^{-i\gamma z} \\
\bar{\mathbf{H}}_{0\_F}\left(x,y,z,t\right) &= \bar{\mathbf{H}}_0\left(x,y\right)e^{i\omega t}e^{-i\gamma z} \\
\bar{\mathbf{E}}_{0\_B}\left(x,y,z,t\right) &= \mathbf{T}\,\bar{\mathbf{E}}_0\left(x,y\right)e^{i\omega t}e^{i\gamma z} \\
\bar{\mathbf{H}}_{0\_B}\left(x,y,z,t\right) &= \bar{\mathbf{H}}_0\left(x,y\right)e^{i\omega t}e^{i\gamma z} \\
\mathbf{T} &= \begin{bmatrix} -1 & 0 & 0 \\ 0 & -1 & 0 \\ 0 & 0 & 1 \end{bmatrix}
\end{aligned}
$$

However, we must also take into account the amplitude of the fields. When this is done the fields in the cavity becomes:

$$
\begin{aligned}
\bar{\mathbf{E}}_F\left(x,y,z,t\right) &= f\left(z\right)\cdot\bar{\mathbf{E}}_{0\_F} && \text{(7.2a)} \\
\bar{\mathbf{H}}_F\left(x,y,z,t\right) &= f\left(z\right)\cdot\bar{\mathbf{H}}_{0\_F} && \text{(7.2b)} \\
\bar{\mathbf{E}}_B\left(x,y,z,t\right) &= g\left(z\right)\cdot\bar{\mathbf{E}}_{0\_B} && \text{(7.2c)} \\
\bar{\mathbf{H}}_B\left(x,y,z,t\right) &= g\left(z\right)\cdot\bar{\mathbf{H}}_{0\_B} && \text{(7.2d)}
\end{aligned}
$$

The functions $f(z)$ and $g(z)$ represents the amplitude and its z-dependence, which is due to power loss, for the forward and backward waves respectively. Power flow density in the waveguide can be expressed using the Poynting vector and has the following form:

$$
\bar{\mathbf{P}} = \bar{\mathbf{E}}\times\bar{\mathbf{H}}^* = \left(\bar{\mathbf{E}}_F+\bar{\mathbf{E}}_B\right)\times\left(\bar{\mathbf{H}}_F+\bar{\mathbf{H}}_B\right)^*
$$

The axial time-averaged power flow along the waveguide, both in the forward and backward directions is then given by:

$$
\bar{P}_{z\_area} = \oint_S \bar{P}_z\cdot d\vec{S}
$$

where S denotes a surface enclosing the interior of the waveguide. In an air filled cavity some of this power will be absorbed by the waveguide walls. For a rectangular waveguide the time-averaged absorbed power per unit length is given by:

$$
P_{loss}\left(z\right) = \frac{1}{2}\oint_c R_s\left|\bar{\mathbf{H}}_{F\_TAN}+\bar{\mathbf{H}}_{B\_TAN}\right|^2 dl
$$

where R_s is surface resistance, c denotes the circumference of the guide cross-section, and the $\_TAN$ subscripts denotes the tangential components of the fields with respect to the cavity wall surface.

7.3.1 Resonant case:

When the cavity is operating in its resonant state, with an 'ideal feed' arrangement which is 'invisible' to the cavity fields, the length of the cavity is an exact

multiple of a guide-wavelength, for both the clockwise and anticlockwise travelling wave. In this case an E-field maximum (node) in the cavity mode occurs where the power is injected into the cavity and signal phase becomes irrelevant. Power can be inserted into the cavity by simply introducing it at a selected node. The differential equation governing the behaviour the cavity mode can, in this case, be obtained by applying power conservation. This requires that the rate of change of axial power flow should equal the power loss into the waveguide walls and leads to the differential equation:

$$0 = \frac{1}{2} \frac{d}{dz} \operatorname{Re}\left(\bar{P}_{z\_area}\right) + P_{loss}$$

For the steady state solution, the equation can be rewritten in a much simplified manner:

$$0 = \frac{d}{dz}\left(P_0 \cdot \left(f^2\left(z\right) - g^2\left(z\right)\right)\right) + A_0 \cdot \left(f\left(z\right) - g\left(z\right)\right)^2 \qquad (7.3)$$

where we define the parameters as:

$$P_0 = \frac{1}{2} \oint_S \operatorname{Re}\left(\left(\bar{\mathbf{E}}_{0\_F} + \bar{\mathbf{E}}_{0\_B}\right) \times \left(\bar{\mathbf{H}}_{0\_F} + \bar{\mathbf{H}}_{0\_B}\right)^*\right) \cdot d\vec{S}$$

$$A_0 = \frac{1}{2}\frac{1}{2} \oint_c R_s \left|\bar{\mathbf{H}}_{F\_0\_TAN} + \bar{\mathbf{H}}_{B\_0\_TAN}\right|^2 dl$$

The solution to the differential equation will give us the field expressions needed for calculating the forces acting on the plate. A solution to the differential equation above must satisfy the following requirements:

$$f\left(z\right) = a_0 + a_1 z$$
$$g\left(z\right) = b_0 + b_1 z$$

The solution will, for the symmetrically loaded case, also fulfil:

$$f\left(0\right) = g\left(L\right)$$
$$f\left(L\right) = g\left(0\right)$$

From this we note that the standing-wave field maxima are of equal magnitude as they should be in a ring-resonator.

The above analysis is strictly applicable to the case where the floating wall is levitated uniformly from the base, i.e. there is no tilting involved.

7.3.2   Tilting float

The problem of tilting of the floating wall (as illustrated in fig. 7.3) cannot be directly solved using the simplified differential equation given above (eq. 7.3). This is because the parameters P_0 and A_0 are no longer invariant along the z-axis, since the cross-sectional area of the cavity now changes as a function of
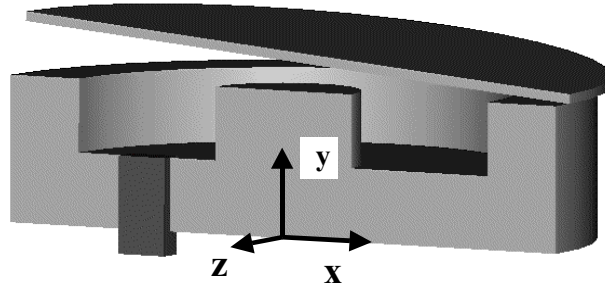
Figure 7.3: Ring-cavity with tilting float. Also shown is the coordinate system used for describing lift and tilt of the plate (as opposed to the coordinate system used for finding the electromagnetic fields). Note the relation between the coordinate system and the excitation slot (symbolized by the dark area on the cut-plane).

z. The solution can be found by formulating P_0 and A_0 exactly as functions of z, and then solving the differential equation directly. Alternatively, the differential equation can be solved by means of a finite element model, which is the method chosen here. Each element is assigned values for P_0 and A_0, according to cavity geometry/float height within the element. This means that each element is assigned an average cross-sectional area. Within each element, the solution to the field amplitude is linear, in accordance with eq. 7.4.

In fig. 7.4, the linearized cavity model is presented showing the way in which the tilting float and cavity are portrayed using finite elements.

It is finally noted that when solving the discretised model, energy levels and power flow must be continuous over element boundaries. However, owing to the adoption of 0th-order approximations for P_0 and A_0 in the calculations, the fields can be discontinuous over element boundaries. Provided that these discontinuities are small, and this can be controlled by employing a sufficient number of elements, the model remains representative of the physics of the problem.

7.3.3 Non-resonant case

The non-resonant case is slightly more complicated than the resonant case since, in addition to the level of the power injected, it is now necessary to take into account the phase relationship between waves entering an element and waves leaving the same element. These relative phases must now be
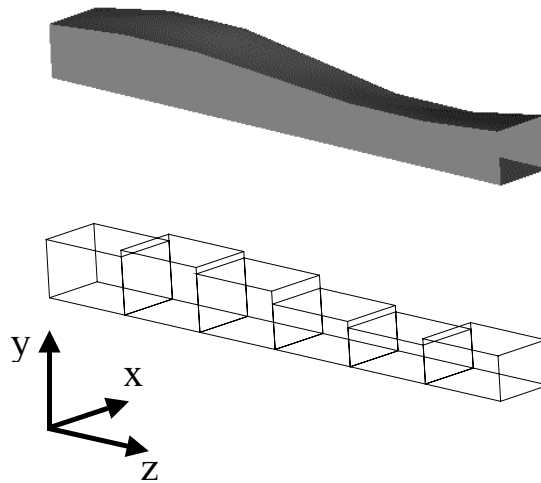
Figure 7.4: Schematic drawing showing the development of the linearized finite element model for a tilting float. Also shown is the coordinate system used for describing the fields in the cavity.

fully accounted for, when the fields expressions (eq. 7.2) are employed in the formulation of the non-resonant version of the discretized model.

It should be noted that the model assumes that all power is injected into the TM_{11} mode of the waveguide. Furthermore, the model also assumes that power reflected at the small cross-sectional changes associated with the discretization of the cavity, are negligible.

A methodology to calculate the fields of a ring cavity with a floating upper wall has been outlined, which is applicable to a tilting float. The main assumptions that have been introduced in the model are:

- The air gap between the float and the waveguide channel is assumed to be lossless. For TM_{11} mode operation this is a good approximation for small gaps.
- The model assumes steady-state operation.
- All power is inserted into a single mode – the TM_{11} mode.
- Reflection of travelling waves at element boundaries is disregarded.
- The method of excitation of the cavity is assumed to be ideal. The model is therefore most accurate for frequencies where the length of the cavity is equal to or close to an odd number of half-wavelengths for the TM_{11} mode.

7.3.4 Mechanical model of the plate

With the electromagnetic fields readily available from the solution of the boundary value problem represented by the cavity, it is a simple task to calcu-

late the electromagnetic forces acting on the floating wall. These forces will obviously be a function of both the degree of tilt and the lift magnitude of the float. Furthermore, calculating the inertial and gravitational forces on the plate is a simple task. Since the mechanical system is much slower than the electromagnetic system, it is justifiable to use the steady-state EM-solution at given positions.

The resultant model is comprehensive and takes into account 3 degrees of freedom of the plate, namely, y movement (levitation), ϕ_x movement (asymmetric tilt), and ϕ_z movement (symmetric tilt). Symmetry is taken with respect to x-y plane through the excitation slot, as illustrated in fig. 7.3.

It should be noted that to construct a more accurate dynamic model of the float movement, squeeze-film damping should also be taken into account. Squeeze-film damping is experienced when two closely adjacent and parallel flat plates are moving normally to each other. A simplified model of the squeeze film mechanism is presented in [33], see also section 2.5, where it is demonstrated that it can be modelled by means of a spring and a damper. Additionally, contact forces between float and the waveguide channel could also be included in the model.

7.4 Modelling results

7.4.1 1-dimensional case

Preliminary computations using the model described above were performed for a float having only one degree of freedom. That is pure lifting and no tilting was considered. It was assumed that the system was fed from a source producing a fixed single-frequency signal close to the resonant frequency of the cavity. The computed levitation force as a function of float height is presented in fig. 7.5 which shows that the force on the float is similar in shape to a resonance curve for the cavity, which typically plots field amplitude as a function of frequency. The reason for this behaviour is that the natural resonant frequency of the cavity changes with float height. The force will therefore peak when the cavity's natural resonant frequency coincides with the frequency of the source.   From fig. 7.5, it is seen that if the power to the cavity is sufficient to generate an EM-force that is larger than the gravitational force (and sticking forces), the float will levitate and reach a stable equilibrium. At the same time we note that if the source frequency changes with the power held constant, the levitation force graph would be shifted either to the right or to the left. A left shift (higher frequency) would mean that the stable levitation height would decrease and eventually there would be no lift at all. A small right shift (lower frequency) would mean that levitation height increases. However, at larger shifts, the system will eventually no longer be capable of reaching the stable point since the increase in power merely
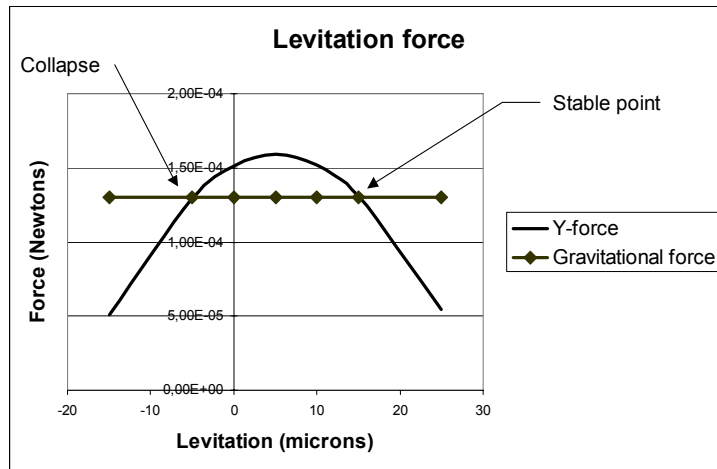
Levitation force

Figure 7.5: The figure shows levitation force as a function of plate levitation. Also included is the gravitational force on the float.

supplies the electromagnetic leakage through the gap between the float and the cavity body. It is noted that the above behaviour puts strict limits on the choice of operating frequency for the source.

7.4.2   2-dimensional case

Having modelled and demonstrated the essential nature of the cavity based electromagnetic levitation system using the simplified 1-dof system described above, the next step is to introduce tilting of the float around its z-axis (float coordinate system) as an additional degree of freedom. Assuming that the system is again excited by a single-frequency source, it is clear that as the float tilts, this frequency may no longer match the resonant frequency of the cavity. The extent and the sensitivity of this frequency mismatch to tilt is clearly a function of float height. The mismatch between excitation frequency and resonant frequency means that the nodes of the modal fields in the cavity will move with respect to the z-axis. This in turn results in a moment being generated on the float due to the non-uniform distribution of the modal fields. This can be seen clearly from fig. 7.6. However it can also be seen that the moment decreases again when the float height results in a large deviation of the cavity resonance from the excitation-frequency. This is due to a general reduction of the field amplitudes.

Any moment of forces acting on the plate will cause it to tilt. Any such tilt will in turn change the cavity dimensions and its resonant frequency, and this implies that further changes will be induced in the forces and moments. In investigating the behaviour related to tilt, one finds that a stable equilibrium of the moment does exist within a limited range of levitation heights (fig. 7.7). However, outside this region there is no equilibrium in free "float". The
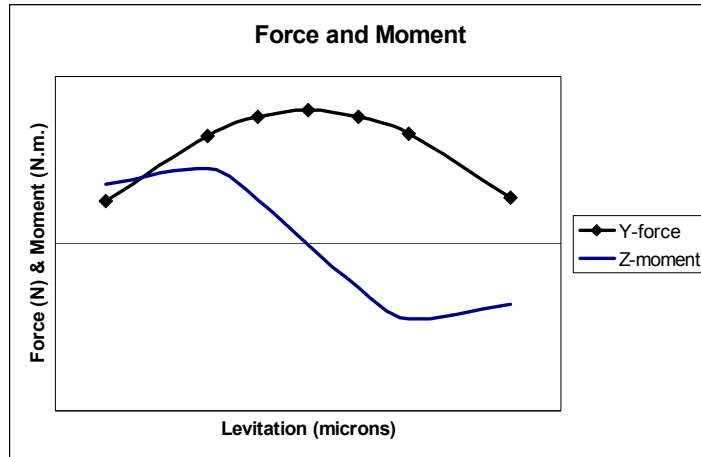
140

Figure 7.6: Normalized levitation forces and moments around the *z*-axis as a function of float height.
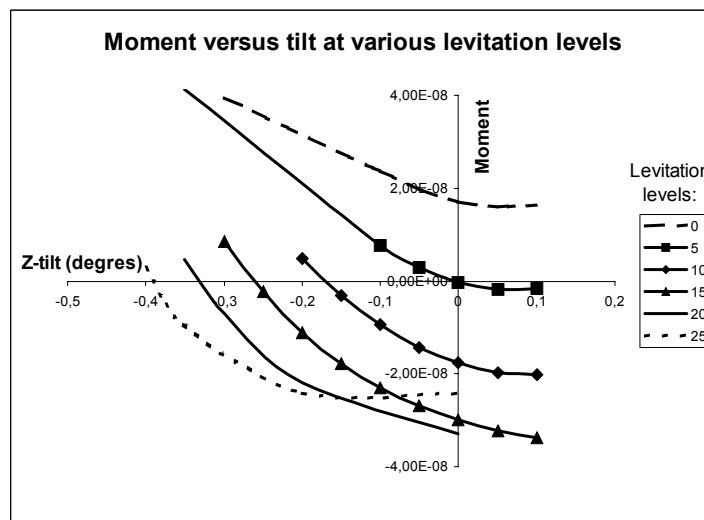

Figure 7.7: Moment as a function of tilt for a range of levitation heights (Levitation heights in microns).
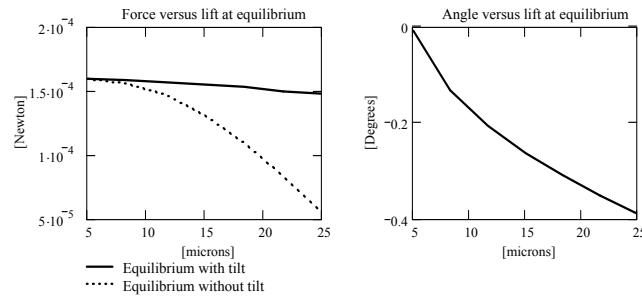
Figure 7.8: LEFT: Levitation force as a function of lift with and without tilt at equilibrium. RIGHT: Tilt as a function of lift at equilibrium.
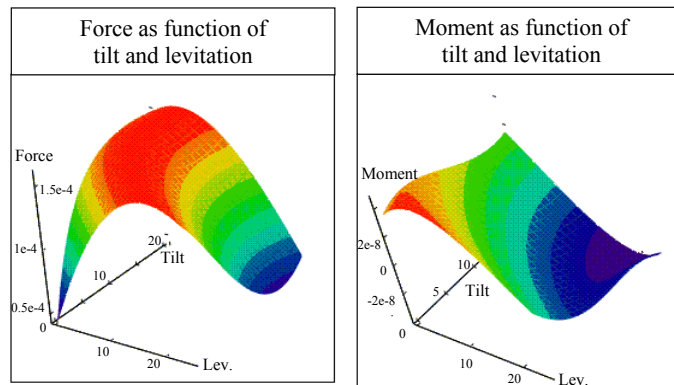

Figure 7.9: Plot of force and moment as function of float height and tilt.

enforced tilt at equilibrium will change the natural frequency of the cavity, and strongly counter-acts the rapid fall-off in the force, as compared to untilted levitation, see left part of fig. 7.8. A plot of the relation between tilt and levitation at equilibrium can also be produced, as can be seen from right part of fig. 7.8. It is also noted that this puts strict limitations on the levitation heights that are practically available for this configuration, since large tilts are unwanted. This is clearly demonstrated by how force and moment depend upon levitation and tilt, as shown in fig. 7.9.

The apparent angular instability at levitation heights below the natural frequency of the cavity is not a significant problem, simply because the system will reach stability when levitated further by introducing more power. At higher levitation heights, the degree of stability can be described by $\frac{dM_z}{d\phi_z}$, (derivative of the z-moment with respect to the angular tilt). On investigating this function it is noted that the angular stability increases with levitation height, see fig 7.10, however at higher levitation heights the field amplitudes
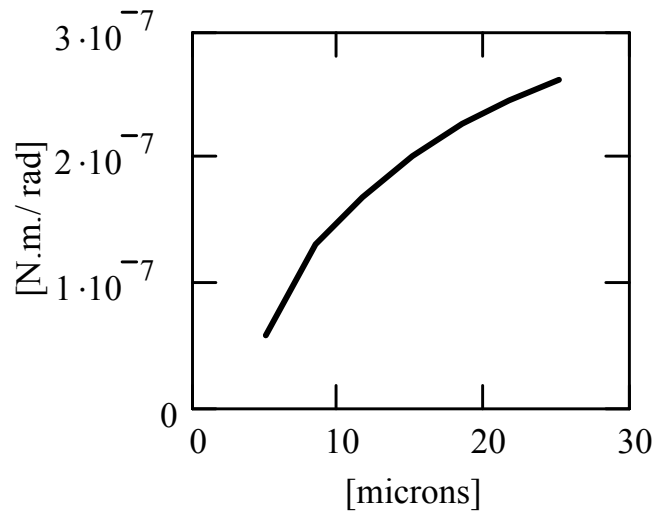
Figure 7.10: Derivative of the z-moment with respect to z-angle at equilibrium state as a function of levitation height. This can be viewed as the linearized angular stiffness acting on the plate.

will degrade strongly due to leakage and reduce the stability. This plot can be compared to a plot of spring stiffness (angular spring).

7.4.3 3-dimensional case

While we have presented the behaviour of the system considering 2 degrees of freedom, it is clear that the plate may also be perturbed about the x-axis. It is noted that a tilt around the x-axis (of the plate coordinate system, see fig. 7.3), is not truly the same as a tilt around the z-axis, due to the location of the feed point. The analysis shows that there will be a restoring moment for a tilt about the x-axis. At the same time, it is revealed that there will be a simultaneous moment about the z-axis. The reason for this is that, as for the tilt about the z-axis, the peaks of the field will change position slightly. However, due to the position of the power input, the symmetry is lost resulting in the moment about the z-axis.

7.4.4 Scaling effects

Above we presented an approximate equation that illustrates the scaling effects of the system (eq. 7.1). However, we have also developed a more accurate model. This more accurate model is used to find more precise estimates of the scaling effects in the system. In this model we have also implemented limitations due to the dielectric strength of dry air. We have disregarded the fact that the dielectric breakdown limit may increase with decreasing geometry. The scaling effects, showing both the inertial forces due to gravity and
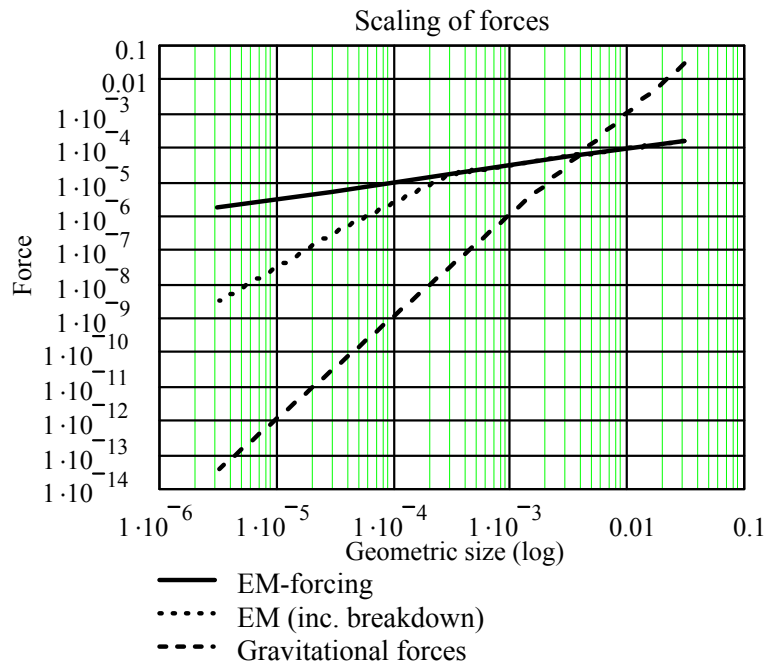
Figure 7.11: The plot shows how the gravitational forces and the electromagnetic forces will scale in the system. For small devices, levitation of the 'float' is possible.

the electromagnetic forces on the 'float' is shown in fig. 7.11.

7.4.5 Conclusion

The analysis gives valuable insight into the physics of the system comprising a ring resonator and disc shaped float. The analysis shows that the system exhibits a stable levitation height for the float even when tilted. The 2-D analysis presented here, demonstrates that a limited range of levitation heights and tilts about the z-axis exists at which the float will be at equilibrium. The computations show that if there is an external moment normal to the face of the float, the plate will show simple rotational behaviour. However, if the external moment is not normal to the face of the plate (e.g. for large tilts), but rather to the surface of the waveguide channel, the float may either have a pure rotation about the z-axis as described above, or some kind of 'wobbling' motion. To decide the exact motion, a more thorough analysis with respect to external forces, inertial forces, and squeeze-film damping needs to be done. Such an analysis of the stability of the system can be done without too much difficulty. The model would include all three degrees of freedom for the float and a linearized "stiffness" matrix could be introduced on the basis of the electromagnetic forces calculated. This will give further insight into the

144

stability mechanisms associated with a disc floating on an electromagnetic cushion.

The compact model enables us, after the construction of the model, to swiftly investigate the system in a manner that clearifies the nature of the system behaviour. Using the insight obtained, it is seen that the limitation on levitation height, due to the tilting effect, can be reduced strongly by leaking energy into the cavity through more than one slot. Equally well may a configuration with two cavities (e.g. as in fig. 7.1) be used to reduce the tilting effect. Any of the two approaches are bound to influence and improve the stability of the system, and a more thorough analysis is required to assess this possibility. However, the general knowledge emanating from the analysis performed here already gives strong indications of what results to expect.

Chapter 8
Conclusion

The aim of this work has been to develop knowledge about macromodelling of microsystems. In doing so, we have followed two different approaches for generating macromodels, namely model order reduction and lumped modelling. The latter is a rather mature method, which has been widely recognized and used for a relatively long period of time. Model order reduction, on the other hand, is a relatively new area still in rapid development. Due to this, the focus is therefore different for the two approaches. The parts considering reduced order modelling is strongly biased towards methodology and concepts, whereas the parts on lumped modelling are biased towards systems and devices.

In the first part of the thesis, we focus on model order reduction. We introduce a few approaches for reducing the model order for linear systems, see chapter 2. We then demonstrate how a model of a (linear) squeeze-film damping system can be simplified. While both the full model of the squeeze-film damping and the method used for reduction can be said to be simple, the example clearly demonstrates capabilities of model order reduction. It is also shown how the squeeze-film damping can be expressed in terms of an electrical equivalent circuit.

In the subsequent chapters (chapters 3-5), the focus is on reduction of non-linear systems, where we present the concept of invariant manifolds. While the concept is general, we utilize it for reducing models. An obvious advantage of using invariant manifold theory is that it offers a conceptually clear understanding of effects and behaviour of nonlinear system.

A major difficulty in using the invariant manifold method is to identify the shape of the manifold. For this, we utilize an asymptotic approach developed by Pesheck [1]. The accuracy of the asymptotic approach is investigated. For our examples, retaining only the most energetic mode,, we find that the nonlinear behaviour of this mode is present, but is relatively small compared to the linear behaviour at small amplitudes. The calculated nonlinear behaviour of the slave modes, however, soon become relatively (important and) complex, and the polynomial approximations of these modes diverge earlier from the exact solution, than does the approximation of the retained mode. Thus the reduced model approximates the retained mode better than the slave modes. This is because the slave modes have a more complex behaviour than the retained mode.

The treatment of external forcing for reduced models created via the invariant manifold approach is discussed. We present a geometrical interpreta-

tion, and show how this leads to a procedure where external forcing can be dealt with in a manner consistent with the invariance property of the manifold. The interpretation also indicates how this can be utilized to minimize errors by creating a manifold of larger dimension.

We have also extended the asymptotic approach in a manner that makes it possible to create design-parameter sensitive models. The asymptotic approach, both with regards to modal amplitude and to design-parameters, limits the range of validity of the design-parameter sensitive model. Nevertheless, it gives the designer the possibility to reason about both linear and nonlinear behaviour of the system, and is therefore a valuable tool. We have successfully investigated an industrialized dual-axis accelerometer by means of the method and demonstrate some of the capabilities of the method.

In the last chapter dealing with reduced order modelling (chapter 5), we discuss how manifolds for nonlinear dissipative systems can be found. By performing a set of simulations backwards-in-time we find trajectories on the manifold. These are in turn used to find the manifold, by interpolating between the known states. In our simulations, the trajectories prove to identify the manifold in a correct manner. A drawback, however, is that numerical errors escalate with amplitude and time. This clearly limits the use, but it is likely that the numerical procedure can be significantly improved to reduce these errors. One major advantage of the method is that it is very easy to implement. The method is demonstrated utilizing a model of the aforementioned dual-axis accelerometer, where squeeze-film damping is included.

In chapter 6, we focus on lumped modelling of a microresonator. We also discuss other topics, and especially electrical equivalents of mechanical systems. In particular, we demonstrate the two analogies between the mechanical and electrical domains. It is shown how the velocity-voltage ($f \rightarrow V$) analogy, linking velocity to voltage, is the natural choice over the force-voltage ($e \rightarrow V$) analogy. This does, however, have the implication that the electrostatic transducer element, expressed as an electrical equivalent, involves a gyrator element.

A microresonator is modelled using lumped modelling techniques, disregarding all nonlinear effects except in the electrostatic transducer. We create electrical equivalent circuits of the system by employing the $f \rightarrow V$ analogy. This is done for various degrees of partitioning of the microresonator. In all we create 3 lumped models with different numbers of degrees of freedom. The results are as expected with regard to accuracy, it improves with increased degrees of freedom. At the same time we note that the more accurate models reveal effects that are of potential importance, and which in turn can be used to improve the models of least accuracy.

In chapter 7, we analyse an electromagnetic system, intended for levitating objects. The analysis is done using a lumped model, where the elements are

created on the basis of analytical solutions. By using the compact model, we demonstrate the scaling effects of the system, clearly showing that this system takes advantage of the miniaturization. Furthermore, the analysis shows that the system is intrinsically stable. However, an effect, which causes the stable state of the floating disc to be slightly tilted is also unveiled. This is the first analysis done assessing the stability criterions of such a system. The insight arising from the analysis gives strong indications on how such a system can be utilized and how it can be improved.

8.1   Lumped modelling versus reduced order modelling

Lumped modelling and reduced order modelling puts different requirements on the designer's background knowledge and experience. Creating a reduced-order model generally requires the designer to build an accurate model in a numerical tool, and thereafter choose an appropriate reduction method. The choice of reduction method is of major importance, since this directly influences the properties of the reduced model. While we have focused on the invariant manifold method for creating reduced models, other reduction methods have also been briefly presented. This gives us an indication of the variety of the methods and also of the differing properties of the methods. Among the important parameters for choosing the best suitable reduction method is need of transparency and accuracy of the reduced model. Nonlinearity is clearly also important in many systems. As of today, however, a severe restriction to the designer's possibilities is that many reduction methods are still immature, and have to little extend been implemented in commercial software.

In model order reduction, the designer is focused on reduction methodology and its capabilities to capture either known or unknown effects from a fairly accurate large model. Lumped modelling on the other hand puts the designer in a totally different situation. He or she must identify all important effects of the system based on physical intuition. Based on that, the model is built in a manner that includes all the identified important effects, leaving unimportant effects unmodelled. For many systems, it is a straightforward task to identify the most important effects, thus making it possible to create a fairly good lumped model. However, other systems may be more complex, challenging the designer's abilities. Hence, the quality of the lumped model becomes highly dependent upon the designer's insight and experience. However, one can often build physical intuition from simulations utilizing more complex models. We also note that a designer failing to recognize a complex effect will not include such an effect in the model. Of equal importance, the designer will not be aware of the error made, resulting in a possibly erroneous model. Despite the drawbacks pointed out, lumped modelling is very popular. This is mainly due to the method's simplicity. At the same time it is a very efficient way of verifying a conceptual idea, since the main effects of the

system will then presumably be known.

Both lumped modelling and reduced order modelling can be used for creating macromodels. However, if we refer to the requirements of a macro-model given in 1.1, we note that neither of the methods are completely capable of fulfilling these requirements. For lumped models, possibly the most important problem concerns inaccuracies (and possible direct errors) in the model. Methods for reduced order modelling are still in rapid development. This is especially true for nonlinear methods where more knowledge must be obtained. Generally, model order reduction methods also do not explicitly include dependencies on design-parameters. Furthermore, they require extensive computational resources in terms of software.

Further improvements in methods for reducing nonlinear models are necessary to make them a valuable tool. When this is fulfilled, reduction methods will become an important complementary tool to lumped modelling for generating macromodels. Lumped modelling will continue to be a very important tool in macromodelling due to its simplicity and fundamental difference from model-order reduction.

8.2   Future work

It is always an advantage for designer to improve their knowledge and understanding of lumped modelling. However, designers can also benefit by expanding the knowledge and understanding of the basic physical effects and domains that are encountered in MEMS.

For model-order reduction the focus is still to develop methods and make them commersially available. We believe that the use of eigenvectors (instead of i.e. Krylov subspace) as basis vectors for the reduction process aids in making the reduced model more transparent. However, it is widely recognized that this results in reduced models that are inaccurate at static load. However, a reduced model based on the Krylov subspace will give correct static load, since the displacement under static load defines the first Krylov subspace vector. It would therefore be interesting to look at model-order reduction where the basis-vectors are a combination of the eigenvectors and the first Krylov subspace vector. This should improve the accuracy, hopefully without reducing the transparency of the model.

Invariant manifolds are an important topic in this thesis. A number of issues must be resolved before the use of manifolds can become widespread. Methods for identifying the manifold must be further investigated. Nonlinear Galerkin methods have already been investigated to a certain degree and appear to be promising. Finally, we have outlined a methodology to handle external forcing in a consistent manner, which should also be further investigated.

Chapter 9
References

[1] Pesheck, E. and Pierre, C. A global methodology for the modal reduction of large nonlinear systems containing quadratic and cubic nonlinearities. Proc. of DETC'97, 1997 ASME design engineering technical conferences, 1997.

[2] Peterson, K. Silicon as a mechanical material. *Proceedings of the IEEE*, 70(5):420–457, 1982.

[3] Senturia, S.D. Cad challenges for microsensors, microactuators, and microsystems. *Proceedings of the IEEE*, 86(8):1611–1626, 1998.

[4] Cook, R.D., Malkus, D.S., and Plesha, M.E. *Concepts and applications of finite element analysis*. John Wiley Sons, 3 edition, 1989.

[5] Chen, G. and Zhou, J. *Boundary element methods*. Academic Press, 1992.

[6] Gunther, A. and Traub, K. Precise equivalent circuits of mechanical filters. *IEEE Trans. on sonics and ultrasonics*, SU-27(5):236–244, Sept. 1980.

[7] Noor, A. Recent advances in reduction methods for nonlinear problems. *Computers and structures*, 13(1-3):31–44, 1981.

[8] Guyan, R.J. Reduction of stiffness and mass matrices. *AIAA Journal*, 3(2):380, 1965.

[9] Senturia, S.D., Aluru, N., and White, J. Simulating the behavior of mems devices: Computational methods and needs. *IEEE Computational Science and Engineering*, 4(1):30–43, January-March 1997.

[10] Golub, G.H. and Van Loan, C.F. *Matrix computations*. The Johns Hopkins University Press, 3 edition, 1996.

[11] Rosenberg, R.M. On nonlinear vibrations of systems with many degrees of freedom. *Advances in applied mechanics*, 9:155–242, 1966.

[12] Vakakis, A.F. Non-linear normal modes (nnms) and their applications in vibration theory: An overview. *Mechanical systems and signal processing*, 11(1):3–22, 1997.

[13] Shaw, S.W. and Pierre, C. Non-linear normal modes and invariant manifolds. *Journal of sound and vibration*, 150(1):170–173, 1991.

[14] Fenichel, N. Persistance and smoothness of invariant manifolds for flows. *Indiana university mathematical journal*, 21:193–225, 1971.

[15] Bianchi, G. and Marzocchi, A. Inertial manifold for the motion of strongly damped nonlinear elastic beams. *Nonlinear differential equations and applications*, 5(2):181–192, 1998.

[16] Burton, T.D. and Rhee, W. on the reduction of nonlinear structural dynamics models. *Journal of vibration and control*, 6(4):531–556, 2000.

[17] Georgiou, I.T. and Schwartz, I.B. Invariant manifolds, nonclassical normal modes, and proper orthogonal modes in the dynamics of the flexible spherical pendulum. *Nonlinear dynamics*, 25(1-3):3–31, 2001.

[18] Yabuno, H. and Nayfeh, A.H. Nonlinear normal modes of a parametrically excited cantilever beam. *Nonlinear dynamics*, 25(1-3):65–77, 2001.

[19] Gabbay, L.D. *Computer aided macromodeling for MEMS*. Phd-dissertation, Massachusetts Institute of Technology, 1998.

[20] Reitz, S., Bastian, J., Haase, J., and Schneider, P. System level modeling of microsystems using order reduction methods. Number 4755 in Proc. of SPIE, pages 365–373, 2002.

[21] Kappagantu, R. and Feeny, B.F. An 'optimal' modal reduction of a system with frictional excitation. *Journal of sound and vibration*, 224(5):863–877, 1999.

[22] Rewienski, M. and White, J.K. Improving trajectory piecewise-linear approach to nonlinear model order reduction for micromachined devices using an aggregated projection basis. Modeling and simulation of microsystems, MSM'02, pages 128–131, 2002.

[23] Grimme, E.J. *Krylov projection methods for model reduction*. Phd-dissertation, University of Illinois at Urbana-Champaign, 1997.

[24] Gallivan, K., Grimme, E., and Van Dooren, P. Pade approximation of large-scale dynamic systems with lanczos methods. Proc. of the 33rd Conf. on decision and control, pages 443–448, December 1994.

[25] Grimme, E.J., Sorensen, D.C., and Van Dooren, P. Model reduction of state space systems via an implicitly restarted Lanczos method. *Numerical algorithms*, 12(1–2):1–31, 1996.

[26] Feeny, B.F. and Kappagantu, R. On the physical interpretation of proper orthogonal modes in vibrations. *Journal of sound and vibration*, 211(4):607–616, 1998.

[27] Feeny, B.F. On proper orthogonal coordinates as indicators of modal activity. *Journal of sound and vibration*, 255(5):805–817, 2002.

[28] Lin, W.Z., Lee, K.H., and Lim, S.P. Proper orthogonal modes for macromodel generation for complex mems devices. Modeling and simulation of microsystems, MSM'03, pages 368–371, 2003.

[29] Kerschen, G. and Golinval, J.C. Physical interpretation of the proper orthogonal modes using the singular value decomposition. *Journal of sound and vibration*, 249(5):849–865, 2002.

[30] Kappagantu, R. and Feeny, B.F. An 'optimal' modal reduction of a system with frictional excitation. *Journal of sound and vibration*, 224(5):863–877, 1999.

[31] Korvink, J. and Rudnyi, E.B. Computer-aided engineering of electro-thermal

mst-devices: moving from device to system simulation. Proc. of EuroSIME 2003, pages 23–27, 2003.

[32] Bechtold, T., Rudnyi, E.B., and Korvink, J. Automatic order reduction of thermo-electric models for mems: Arnoldi versus guyan. Advanced semiconductor devices and microsystems, the fourth international conference on, pages 333–336, 2002.

[33] Westby, E. and Fjeldly, T.A. Dynamical equivalent-circuit modeling of mems with squeezed gas film damping. In *Proc. of the 19th Nordic semiconductor meeting*, volume T101 of *Physica scripta*, pages 192–195, 2002.

[34] Veijola, T., Kuisma, H., Lahdenperä, J., and Ryhänen, T. Equivalent-circuit model of the squeezed gas film in a silicon accelerometer. *Sensors and actuators*, A48:239–248, 1995.

[35] Griffin, W.S., Richardson, H.H., and Yamanami, S. A study of fluid squeeze-film damping. *Journal of basic engineering*, pages 451–456, June 1966.

[36] Senturia, S.D. *Microsystem design*. Kluwer Academic Publisher, 2001.

[37] Blech, J.J. On isothermal squeeze films. *Journal of Lubrication Technology*, 105:615–620, 1983.

[38] Schrag, G., Voigt, P., and Wachutka, G. Squeeze film damping in arbitrary shaped microdevices modelled by an accurate mixed level scheme. Modeling and simulation of microsystems, MSM'01, pages 92–95, 2001.

[39] Turowski, M., Chen, Z., and Przekwas, A. Squeeze film behaviour in mems for large amplitude motion -3d simulations and nonlinear circuit/behavioral models. Int. Workshop on behavioral modeling and simulation (BMAS'98), October 1998.

[40] Wong, A.-C., Clark, J.R., and Nguyen, C.T.-C. Anneal-activated, tunable, 68 mhz micromechanical filters. Transducer's 99, 1999 International conference on solid-state sensors and actuators, pages 1390–1393, June 7-10 1999.

[41] Maekoba, H., Helin, P., Reyne, G., Bourouina, T., and Fujita, H. Modeling and optimization of bi-stable optical switch. Modeling and simulation of microsystems, MSM'00, pages 166–169, 2000.

[42] Rewienski, M. and White, J.K. A trajectory piecewise-linear approach to model order reduction and fast simulation of nonlinear circuits and micromachined devices. *IEEE trans. on computer-aided design of integrated circuits and systems*, 22(2):155–170, feb. 2003.

[43] Ananthasuresh, G.K., Gupta, R.K., and Senturia, S.D. An approach to macromodeling of mems for nonlinear dynamic simulations. DSC-Vol. 59, microelectromechanical systems (MEMS) ASME, 1996.

[44] Hung, E.S., Yang, Y.-J., and Senturia, S.D. Low-order models for fast dynamical simulation of mems microstructures. Transducer's 97, 1997

International conference on solid-state sensors and actuators, 1997.

[45] Gabbay, L.D. *Computer aided macromodeling for MEMS*. PhD thesis, Massachusetts Institute of Technology, June 1998.

[46] Vakakis, A.F. *Normal modes and localization in nonlinear systems*. John Wiley and Sons, 1996.

[47] Chen, C.-P. and Wong, D.F. Error bounded pade approximation via bilinear conformal transformation. Proc. of the 36th Design automation conference, pages 7–12, 21-25 June 1999.

[48] Shaw, S.W. and Pierre, C. Normal modes for non-linear vibratory systems. *Journal of sound and vibration*, 164(1):85–124, 1993.

[49] Nayfeh, A.H. On nonlinear normal modes of systems with internal resonance. *Journal of vibration and acoustics*, 118:340–345, 1996.

[50] Pesheck, E., Pierre, C., and Shaw, S.W. A new galerkin-based approach for accurate non-linear normal modes through invariant manifolds. *Journal of sound and vibration*, 249(5):971–993, 2002.

[51] Marion, M. and Temam, R. Nonlinear galerkin methods. *SIAM Journal on numerical analysis*, 26(5):1139–1157, October 1989.

[52] Slater, J.C. A numerical method for determining nonlinear normal modes. *Nonlinear dynamics*, 10:19–30, 1996.

[53] Boivin, N. *Non-linear modal analysis of structural systems using invariant manifolds*. PhD thesis, University of Michigan, 1995.

[54] Ribeiro, P. and Petyt, M. Non-linear vibration of beams with internal resoance by the hierarchical finite-element method. *Journal of sound and vibration*, 224(4):591–624, 1999.

[55] Szemplinska-Stupnicka, W. *The behaviour of non-linear vibrating systems*. Kluwer Academic Publishers, 1990.

[56] Nayfeh, A.H. and Mook, D.T. *Nonlinear oscillations*. John Wiley and Sons, 1995.

[57] Westby, E. and Fjeldly, T.A. Nonlinear analytical reduced-order modeling of mems. Modeling and simulation of microsystems, MSM'02, pages 150–153, 2002.

[58] Nelson, R.B. Simplified calculation of eigenveector derivatives. *AIAA Journal*, 14(9):1201–1205, 1976.

[59] Sutter, T.R., Camarda, C.J., Walsh, J.L., and Adelmans, H.M. Comparison of several methods for calculating vibration mode shape derivatives. *AIAA Journal*, 26(12):1506–1511, 1988.

[60] Friswell, M.I. The derivatives of repeated eigenvalues and their associated eigenvectors. *Journal of vibration and acoustics*, 118:390–397, July 1996.

[61] Kenny, S.P. and Hou, G.J.W. Approximate analysis for repeated eigenvalue problems with applications to controls-structures integrated design. NASA

Technical Paper 3439, June 1994.

[62] Hilborn, R.C. *Chaos and nonlinear dynamics*. Oxford University Press, 1994.

[63] Foias, C., Sell, G.R., and Temam, R. Inertial manifolds for nonlinear evolutionary equations. *Journal of differential equations*, 73:309–353, 1988.

[64] Mikhlin, Y.V. and Morgunov, B.I. Normal vibrations in near-conservative self-excited and viscoelastic nonlinear systems. *Nonlinear dynamics*, 25:33–48, 2001.

[65] Temam, R. Inertial manifolds. *The mathematical intelligencer*, 12(4):68–74, 1990.

[66] Westby, E. Nonlinear reduced modeling of a damped dual-axis accelerometer. Eurosime '03, pages 161–164, 2003.

[67] Johnson, R.A. *Mechanical filters in electronics*. John Wiley and Sons, 1983.

[68] Sheahan, D.F. and Johnson, R.A. Crystal and mechanical filters. *IEEE Trans. on circuits and systems*, 22(2):69–88, February 1975.

[69] Clark, J.R., Bannon, F.D., Wong, A.-C., and Nguyen C. T.-C. Parallel-resonator hf micromechanical bandpass filters. Transducer's 97, 1997 International conference on solid-state sensors and actuators, pages 1161–1164, 1997.

[70] Rao, S.S. *Mechanical vibrations*. Addison-Wesley Publishing Company, 3 edition, 1995.

[71] Reddy, J.N. On locking-free shear deformable beam finite elements. *comput. methods appl. mech. engrg.*, 149:113–132, 1997.

[72] Mukherjee, S., Reddy, J.N., and Krishnamoorthy, C.S. Convergence properties and derivative extraction of the superconvergent timoshenko beam finite element. *comput. methods appl. mech. engrg.*, 190:3475–3500, 2001.

[73] Rao, S.S. and Gupta, R.S. Finite element vibration analysis of rotating timoshenko beams. *Journal of sound and vibration*, 242(1):103–124, 2001.

[74] Banerjee, J.R. and Sobey, A.J. Energy expressions for rotating tapered timoshenko beams. *Journal of sound and vibration*, 254(4):818–822, 2002.

[75] Jezierski, E. On electrical analogoues of mechatronic systems. Second workshop on robot motion and control, pages 181–184, October 2001.

[76] Bielefeld, J., Pelz., G., and Zimmer, G. Electrical network formulations of mechanical finite-element models. MICROSIM II, pages 239–247, 1997.

[77] Tilmans, H.A.C. Equivalent circuit representation of electromechanical transducers: I. lumped-parameter systems. *Journal of micromech. microeng.*, 6:157–176, 1996.

[78] Tilmans, H.A.C. Equivalent circuit representation of electromechanical transducers: I. distributed-parameter systems. *Journal of micromech. microeng.*, 7:285–309, 1997.

[79] Beatovic, D., Levin, P.L., Sadovic, S., and Hutnak, R. A galerkin formulation of the boundary element method for two-dimensional and axi-symmetric problems in electrostatics. *IEEE Trans. on electrical insulation*, 27(1):135–143, February 1992.

[80] Hedenstierna, H., Habibi, S., Nilsen, S.M., Kvisteroy, T., and Jensen, G.U. Bulk micromachined angular rate sensor based on the 'butterfly'-gyro structure. The 14th IEEE International Conference on MEMS, MEMS2001, pages 178–181, 2001.

[81] Corman, T., Enoksson, P., Noren, K., and Stemme, G. Novel burst technology for closed loop detection and excitation of resonant silicon sensors. Transducer's 99, 1999 International conference on solid-state sensors and actuators, pages 1402–1405, June 7-10 1999.

[82] Wang, K., Bannon, F.D., Clark, J.R., and Nguyen, C.T.-C. Q-enhamcement of microelectromechanical filters via low-velocity spring coupling. IEEE Int. ultrasonics symp., pages 323–327, Oct 5-8 1997.

[83] Wang, K., Wong, A.-C., and Nguyen, C.T.-C. Vhf free-free beam high-q micromechanical resonators. *Journal of microelectromechanical systems*, 9(3):347–360, september 2000.

[84] Ottosen, N and Petersson, H. *Introduction to the finite element method*. Prentice Hall, 1992.

[85] Westby, E.R. Identifcation of material parameters and the inverse method. Master's thesis, Norwegian University of Science and Technology, 1998.

[86] Westby, E., Sangster, A., and McErlean, E. Stability of a cavity based electromagnetic suspension system for micro-scale actuators. *Journal of electromagnetic waves and applications*, 17(9):1331–1347, 2003.

[87] de Wolf, D.A. *Essentials of electromagnetics for engineering*. Cambridge University Press, 2001.

[88] Griffiths, D.J. *Introduction to electrodynamics*. Prentice Hall, third edition, 1999.

[89] Kumar, S., Cho, D., and Carr, W.W. Experimental study of electric suspension for micro-bearings. *Journal of microelectromechanical systems*, 1(1):23–30, 1991.

[90] Fukatsu, K., Murakoshi, T., and Esashi, M. Electrostatically levitated micromotor for inertia measurement system. Tech. digest of the transducers'99 Conf., pages 1558–1561, 1999.

[91] Toda, R., Takeda, N, and et. al. Electrostatically levitated spherical 3-axis accelerometer. 15th Internat. conf. on electromech. Syst., pages 710–713, 2001.

[92] Moser, R. and Hannes, B. Precise positioning using electrostatic glass motor with diamagnetically suspended rotor. *IEEE Trans. on applied*

superconductivity, 12(1):937–939, 2002.

[93] Kumar, S., Cho, D., and Carr, W.W. A proposal for electrically levitating micromotors. *Sensors and actuators*, 24:141–149, 1990.

[94] Sangster, A. and McErlean, E. Electromagnetic levitation of micro-scale actuators using microwave cavity resonators. *IEE Proc. (MAP)*, 147(5):359–363, 2000.

[95] Sangster, A., McErlean, E., and et. al. Coupled re-entrant cavity system for electromagnetic levitation. *IEEE Journal of MEMS*, 15(6):815–831, 2001.

[96] Sangster, A. and McErlean, E. Magnetic suspension for microactuators using microwave cavity resonators. *IEE Proc. (MAP)*, 149(1):45–49, 2002.

[97] Sulfridge, M., Saif, T., Miller, N., and O'Hara, K. Optical actuation of a bistable mems. *Journal of MEMS*, 11(5):574–583, 2002.